Impacts of Light-Absorbing Impurities in Snow and Ice on Hydrology

Felix Nikolaus Matt

Dissertation submitted for the degree of Philosophiae Doctor (PhD)

Department of Geosciences
Faculty of Mathematics and Natural Sciences
University of Oslo

Oslo, Norway
June 2019

Series of dissertations submitted to the
Faculty of Mathematics and Natural Sciences, University of Oslo
No. 2197

ISSN 1501-7710

Cover: Hanne Baadsgaard Utigard.
Print production: Reprosentralen, University of Oslo.

Abstract

About one eighth of the Earth's surface is permanently covered by snow and ice, and about one third is impacted by seasonal snow cover. Snow melt is an important contributor to fresh water supply in many of these regions, making a profound understanding of snow accumulation and melt processes paramount for water resource management, flood prediction, and hydropower production. A great role plays hereby the amount of solar radiation absorbed by the snow due to the direct impact on the energy budget. Clean snow reflects most of the sunlight, creating a white appearance. In fact, snow is known to be the most reflecting natural surface on Earth. However, the albedo of snow, a measure of the ability of a surface to reflect sunlight, undergoes large variations due to a number of processes that can lead to a reduction of the snow albedo. Recently, implications of particles mixing within the snow that have the ability to strongly absorb in the visible range of the solar spectrum have caught the attention of the research community. These particles originate from fossil fuel combustion, forest fires, volcanic activities, atmospheric transport of mineral dust, and biological activity, and are released by both natural and anthropogenic sources. Lowering the snow albedo through their presence in snow, it has been found that these particles cause a significant radiative forcing on global and regional scales. While the effect has mostly been studied in the context of climate impacts, further fields of research such as regional hydrologic impacts and implications for glacier mass balance are just emerging. In particular the response of river flow of seasonally snow cowered basins has received little attention despite indications of significant implications from light absorbing particles during snow melt in various regions.

This thesis focuses on the hydrologic response to light absorbing impurities in snow at the catchment scale. The development of a snow algorithm that allows the consideration of light absorbing impurity impacts on snow processes is presented and applied within a rainfall-runoff hydrological model. The significance of these impacts to the hydrologic response is shown for study regions located in Norway and the Indian Himalayas. By announcing the first of its kind rainfall-runoff model allowing to dynamically account for light-absorbing snow impurities, this thesis contributes to the understanding of the magnitude of impacts in the study regions, as well as raises attention to the uncertainties connected with model representations of such processes.

Last but not least, the hydrologic model framework used in this thesis has been developed in parallel to this thesis, from a joint effort by Statkraft AS and the University of Oslo. The development of the framework aims for a model tool suitable for catchment scale analysis in the fields of hydropower production, flood prediction, and water resource management, with a strong focus on efficient operational application.

Acknowledgements

Many people have supported and encouraged me throughout my PhD. First of all, I would like to thank my supervisor John Burkhart, without whom this work would not have been possible. John came up with essential ideas, provided extra funding for traveling, and always had his door open for discussions. Furthermore, John has a very detailed understanding of IT matters, from which I greatly benefited. The knowledge gained from discussions spun around these are fundamentally defining my interests and work today. Towards the end of my PhD, John also came up with additional funding, which made it possible to keep on focusing on the thesis. Thank you very much, John! Besides John as main supervisor, Lena Merete Tallaksen co-supervised this thesis and also always had her door open for a quick and fruitful chat. Thank you Lena for taking this role!

For IT support I would like to thank Hans Peter Verne. A big thanks also goes to Anne Claire Fouilloux for assisting me with setting up models on UiO's high performance computing clusters. Sigbjørn Helset from Statkraft spent many night hours after work and during weekends debugging the hydrologic model used in this thesis, looking at badly written code and replacing it with something that actually works. Thank's a lot, Sigbjørn!

Great thanks also goes to my office mate Paul for support and discussions whenever needed, and many adventures outside the walls of the geology building, most of which on skis.

Likewise, I would like to thank Pim, Thomas, and Bas for a great time at work and even better times off-work. Thanks for accompanying me in skiing, climbing, biking, playing and watching football, and drinking a beer or more from time to time. In this respect I also owe a big thanks to the members of geo-football, of whom a big share has already been mentioned above. In addition: Leo, Adrien, Kjetil, Chris N., and Kris. Thanks also to Chris Z. for many bar visits and the box of beer I'll get after the defense. And to Timo, Jonas, and Manuel anyway and always.

Finally, I would like to thank my parents, on whose support I always can count, regardless in which matter. Danke Mama und Papa! My biggest gratitude, however, goes to you, Ane ♡. Working on this thesis wasn't a stroll in the park and your patience and support throughout the

years, particularly in the recent past, were the most important ingredient to finally getting the beast submitted.

Contents

List of symbols and abbreviations

A_s	snow specific surface area [m^2 kg^{-1}].
A_s	specific surface area, see also SSA [m^2 kg^{-1}].
CFR	refreezing parameter [-].
CWH	liquid water fraction threshold [-].
D_i	atmospheric deposition mass flux of LAISI species i [kg s^{-1} m^{-2}].
E_a	actual evapotranspiration [mm].
E_p	potential evapotranspiration [mm].
H_l	latent heat flux [W m^{-2}].
H_r	heat flux from rain [W m^{-2}].
H_s	sensible heat flux [W m^{-2}].
H_{vap}	latent heat of vaporization [J kg^{-1}].
K	net shortwave radiation [W m^{-2}].
L	net longwave radiation [W m^{-2}].
M_g	glacier melt [mm].
M_s	snow melt [mm].
M_{rf}	amount of refreezing liquid water [mm].
P	precipitation [mm].
Q	discharge [$m^3 s^{-1}$].
Q_a	absorption efficiency [-].
Q_s	scattering efficiency [-].
R	net radiation [W m^{-2}].
S	liquid water storage [mm].
T	air temperature [°C].
TF_g	glacier melt factor [mm d^{-1} K^{-1}].
TF_s	snow melt factor [mm d^{-1} K^{-1}].
TT_g	threshold temperature for glacier melt [°C].
TT_s	threshold temperature for snow melt [°C].

T_s	snow temperature [°C].
ΔE	net energy flux at snow surface [W m^{-2}].
Δt	model time step [s].
Θ	mass fraction of liquid water content in snow [-].
α	broadband albedo [-].
α_g	albedo of underlying ground [-].
α_λ	spectral albedo [-].
γ	psychrometric constant [kPa K^{-1}].
λ	wavelength of electromagnetic wave [μm].
μ_0	cosine of solar zenith angle [-].
ρ_i	density of ice, 917 kg m^{-3}.
θ_0	solar zenith angle [°].
a	Priestley-Taylor constant [-].
c_1	catchment specific discharge recession parameter [-].
c_2	catchment specific discharge recession parameter [-].
c_3	catchment specific discharge recession parameter [-].
c_p	heat capacity of water [J kg^{-1} K^{-1}].
$c_{b,i}$	mixing ratio of LAISI species i in model bottom layer [ng g^{-1}].
$c_{s,i}$	mixing ratio of LAISI species i in model surface layer [ng g^{-1}].
g	asymmetry factor [-].
h	ratio of diffuse to total (diffuse+direct) incident flux [-].
k_i	scavenging ratio of LAISI species i [-].
$m(\lambda)$	complex refractive index of ice [-].
$m_{b,i}$	mass of LAISI species i in model bottom layer [kg m^{-2}].
$m_{im}(\lambda)$	imaginary part of the complex refractive index of ice [-].
$m_{re}(\lambda)$	real part of the complex refractive index of ice [-].
$m_{s,i}$	mass of LAISI species i in model surface layer [kg m^{-2}].
q_b	melt water mass flux out of model bottom layer [kg s^{-1} m^{-2}].
q_s	melt water mass flux from the model surface to the bottom layer [kg s^{-1} m^{-2}].
r	optical grain radius, see also OGR [μm].
s	snow water equivalent, see also SWE [mm].

$s_v(T)$	slope of the relationship between the saturation vapour pressure and air temperature [kPa K^{-1}].
t	time [s].
AeroCom	Aerosol Comparisons between Observations and Models project.
BC	Black Carbon.
BOBYQA	Bound Optimization BY Quadratic Approximation algorithm.
CV	coefficient of variation.
ECLIPSE	Evaluating the Climate and Air Quality Impacts of Short-Lived Pollutants project.
ECMWF	European Center for Medium Range Weather Forecasting.
FLEXPART	Flexible Particle Dispersion Model.
GAINS	Greenhouse gas - Air pollution Interactions and Synergies.
GFED	Global Fire Emissions Database.
HKKH	Hindu Kush, Karakoram, and Himalayan.
LAISI	light-absorbing impurities in snow and ice.
LAP	light-absorbing particles.
MAC	mass absorption cross section [m^2 kg^{-1}].
MET	The Norwegian Meteorological Institute.
MODDRFS	MODIS Dust Radiative Forcing in Snow.
MODIS	Moderate-resolution Imaging Spectroradiometer.
NIR	near-infrared.

NSE	Nash-Sutcliffe model efficiency [-].
NVE	The Norwegian Water Resources and Energy Directorate.
OC	Organic Carbon.
OGR	optical grain radius, see also r [μm].
PDF	probability density function.
SBDART	Santa Barbara DISORT Atmospheric Radiative Transfer model.
SCA	snow covered area [m^2].
SCE-UA	Shuffled Complex Evolution - University of Arizona algorithm.
SDC	snow depletion curve.
Shyft	Statkraft's Hydrologic Forecasting Toolbox.
SNICAR	Snow, Ice, and Aerosol Radiative model.
SSA	specific surface area, see also A_s [m^2 kg^{-1}].
SWE	snow water equivalent, see also L [mm].
SWIR	shortwave-infrared.
TP	Tibetan Plateau.
TPH	Tibetan Plateau and Himalaya.
UV	ultraviolet.
VIS	visible spectrum.
WATCH	Water and Global Change project.
WRF	Weather Research and Forecasting Model.
WRF-Chem	Weather Research and Forecasting Model coupled with chemistry.

Part I

Overview

1 Introduction

1.1 Motivation

In many regions of the world, snow melt contributes to a major portion of the water budged (e.g., Junghans et al., 2011; Jeelani et al., 2012; Engelhardt et al., 2014), and about one sixth of the world's population is dependent on fresh water supply from snow or glacier melt (Hock et al., 2006). In particular in a warming climate (IPCC, 2013), subsequent accelerated melting in many mountain systems (Pepin et al., 2015), along with increasing fresh water demands due to rapid population growth (Cosgrove and Loucks, 2015), detailed understanding of the hydrologic system is essential. Reliable prediction of the timing and quantity of snow melt and stream flow are paramount in order to perform water resource management that assures water supply to millions of people.

Hydrological models are used by researchers, water resource managers, and policy makers to understand, predict, and manage water. Given the important role of snow cover in many hydrological systems, a good model representation of snow is therefore of considerable importance. In order to capture snowpack dynamics with the help of numerical models, each aspect of the energy budged needs to be treated with sufficient care, taking into account the predominant processes. A specific property of snow is to reflect a large fraction of sunlight and thus limit the portion of energy available for snow melt provided by the sun.

For snow, the ability to reflect sunlight plays a key role in the energy budget of the snowpack. However, the variable determining the fraction of reflected solar radiation, the so called snow albedo, remains a large source of uncertainties in the prediction of snowpack evolution and melt (e.g., Malik et al., 2014; Jacobi et al., 2015; Thackeray and Fletcher, 2016). As snow ages, the snow albedo undergoes large temporal fluctuations. The mean size of snow grains increases over time, as the snow microstructure changes due to metamorphoses processes caused by sintering (Rosenthal et al., 2007), sublimation (Flanner and Zender, 2006) and freeze-thaw processes (Kapil et al., 2010). As a result of the altered scattering properties of the snow grains, snow albedo generally decreases over time (e.g., Wiscombe and Warren, 1980), leading to higher absorption of solar radiation and increased snow melt.

But snow metamorphoses are not the only processes causing a decreased ability to reflect sunlight. The role of small particles mixed with the snow and their property to efficiently absorb sunlight in the visible spectrum, where snow albedo of clean snow is highest, caught the attention of scientists already in the 1970s and 1980s (e.g Higuchi and Nagoshi, 1977; Warren and Wiscombe, 1980). More recently, significant radiative forcing from absorbing impurities in snow and ice on a global scale was predicted in several studies (Hansen and Nazarenko, 2004; Hansen et al., 2005; Flanner et al., 2007), bringing the topic back into the focus of research. Nowadays it is known that the resulting modification of the snow's energy budget due to the presence of these impurities can lead to shortening of snow cover duration (Painter et al., 2007; Ménégoz et al., 2014), acceleration of glacier melt (Kaspari et al., 2015; Zhang et al., 2017), and altering of the hydrologic cycle (Qian et al., 2009; Painter et al., 2010; Qian et al., 2011; Oaida et al., 2015; Painter et al., 2017).

Many aspects of the role of these particles concerning hydrological processes are not yet understood and uncertainties are high (Qian et al., 2014b). On the other hand, understanding shifts in the timing and amount of runoff from snowmelt due to light-absorbing aerosols could help improve hydrologic predictions and reduce both uncertainty in predicting runoff and stressors in local water supplies (Bryant et al., 2013). However, to date, no rainfall-runoff model aiming for application in water resource management, hydropower production environments, and flood forecasting is able to account for the dynamic albedo response to light-absorbing impurities in snow.

The scope of this thesis is the integration of light-absorbing particles originating from atmospheric aerosol deposition in a hydrological framework operating at the catchment scale. Aiming for improving hydrological modelling, the model is applied and evaluated in different regions. The herein addressed scientific gaps between current state of knowledge and the introduced objectives are further specified and discussed in Chapter 2.

1.2 Research Aims

The aim of this thesis is to develop, test, and apply a hydrologic catchment model that allows to link atmospheric aerosol deposition to hydrological predictions at the catchment scale.

In order to address this, three main tasks are addressed:

- **Task 1:** *Develop a snow algorithm able to dynamically account for light-absorbing aerosols.*

Light-absorbing particles originating from atmospheric aerosol deposition will be integrated in an energy balance based snowpack algorithm. The snowpack algorithm will then be implemented in a hydrological model operating at the catchment scale.

- **Task 2:** *Investigate the sensitivity and uncertainty of processes related to light-absorbing impurities.*

  Sensitivities of parameters determining the impact of light-absorbing impurities on snowpack evolution will be identified through simulations at the point scale. Uncertainties in the hydrologic response will be determined through simulations at the catchment scale.

- **Task 3:** *Integrate remotely sensed snowpack information in order to improve model predictions of light-absorbing impurity impacts on the hydrologic response.*

  Methods to integrate satellite retrievals of light-absorbing impurities in hydrologic simulations will be developed, applied, and evaluated aiming to improve the impact estimate of light-absorbing impurities on discharge generation at the catchment scale.

1.3 Outline

This thesis is composed of two parts. **Part I** provides an overview of the presented research and yet unpublished work. A general background on the state of knowledge of the role of light-absorbing impurities on hydrologic systems is given in Chapter 2. The gap of knowledge addressed in this thesis is pointed out and put into context of the recent body of research in the field. Chapter 3 provides a general overview of the methodologies applied in the analysis, with particular focus on modelling approaches. Geospatial and meteorological datasets, and the climatic and geographic characteristics of study regions used in the research of this thesis are described in Chapter 4. The backbone of this thesis are three publications, shortly summarized in Chapter 5 together with unpublished additional material related to each of the publications. A general discussion of the results put into context of the state of science on the topic is provided in Chapter 6. Finally, conclusions are summarized in Chapter 7 alongside with an outlook.

Part II consists of the three scientific journal articles forming the basis of this thesis. Paper II and III are peer-reviewed and open-access published in internationally recognized scientific journals. The manuscript of Paper I is soon to be submitted to the Hydrology and Earth System Sciences journal of Copernicus Publications.

2 Scientific Background

2.1 Snow Albedo

Snow melt plays a key role in the hydrology of catchments of various high mountain areas such as the Himalayas (Jeelani et al., 2012), the Alps (Junghans et al., 2011), the western United States (Li et al., 2017a), and the Norwegian mountains (Engelhardt et al., 2014), and is an equally important contributor to stream flow generation as rain in these areas. Furthermore, timing and magnitude of the snow melt are major predictors of floods (Berghuijs et al., 2016) and land slides (Kawagoe et al., 2009), and important factors in water resource management and operational hydropower forecasting. For these reasons, detailed understanding of the key processes determining snow melt is paramount.

However, there are large uncertainties in many variables specifying the temporal evolution of the snowpack, and the portion of incoming shortwave radiation that is absorbed by snow is one of the most important due to the direct effect on the energy input to the snowpack from solar radiation (e.g., Anderson, 1976) and subsequent implications for snow temperature, sublimation, and melt.

In earth sciences, the dimensionless parameter *albedo* is fundamental to describe the ability of a surface to reflect incoming electromagnetic radiation. By definition, the spectral albedo α_λ is defined as the ratio of the surface-reflected upwelling to the incident ($F_\lambda \downarrow$) flux of monochromatic radiation at wavelength λ,

$$\alpha_\lambda = \frac{F_\lambda \uparrow}{F_\lambda \downarrow}, \tag{2.1}$$

measured over the upward directed semi-hemispherical space. The radiative fluxes F_λ, or irradiances, describe the power per unit area and unit wavelength interval that is incident ($\downarrow$) on or reflected ($\uparrow$) by the surface.

Likewise, the albedo within a spectral band specified by λ_1 and λ_2, called broadband albedo α, is defined as the ratio of the total surface-reflected upwelling ($F \uparrow$) to the total incident ($F \downarrow$) flux of radiation,

$$\alpha = \frac{F\uparrow}{F\downarrow} \tag{2.2}$$

$$= \frac{\int_{\lambda_1}^{\lambda_2} F_\lambda \uparrow d\lambda}{\int_{\lambda_1}^{\lambda_2} F_\lambda \downarrow d\lambda}. \tag{2.3}$$

Even though broadband albedos can be determined for any spectral band, in earth sciences, the term broadband albedo often refers to the shortwave albedo. Most commonly, shortwave albedos are calculated using the 0.25-5 μm or the 0.3-3 μm wavelength band. In practice, albedo calculations using the two ranges produce similar results because solar irradiance at wavelengths beyond 0.3-3 μm approach zero at the earth's surface (see the spectral irradiance at the earth's surface shown in Figure 2.1). In this thesis, however, broadband/shortwave albedo is referred to as the 0.3-5 μm band if not specified otherwise, because the radiative transfer model introduced in Section 3.3.3, which is used to determine snow albedos throughout this thesis, operates on this wavelength range. It also should be noted that the albedo is not an intrinsic surface property. Instead, the albedo depends on both the radiative properties of the surface and the spectral and angular distributions of the incident radiation. The latter is governed by atmospheric composition and the direction of the beam of light.

Snow is known to be the most reflective natural surface on Earth (Coulson et al., 1965) and plays a crucial role in the energy balance of the current Earth's climate system due to the ice-albedo feedback (e.g., Kashiwase et al., 2017). Fresh snow typically reflects approximately 90% of incoming solar radiation (albedo of 0.9). Over time, snow undergoes metamorphosis as a result of sintering (Rosenthal et al., 2007), sublimation (Flanner and Zender, 2006) and freeze-thaw events (Kapil et al., 2010). Due to these processes, the micro structure of snow changes, along with the scattering properties of the snow grains, resulting in a potentially significant drop in albedo. The subsequent increased absorption of solar radiation has implications for timing and quantity of snow melt.

To the human observer, fresh snow appears as a white surface. The impression of snow as a white surface corresponds to generally high spectral albedos in the visible spectrum (VIS; 0.3-0.7 μm), where solar radiation peaks in intensity (Figure 2.1). What remains hidden to the human observer is that at wavelengths outside the upper bound of the visible spectrum, spectral snow albedos drop rapidly in the near-infrared (NIR, 0.7-1.4 μm) and stay comparably low at longer wavelengths (snow is nearly "black" in the infrared spectrum).

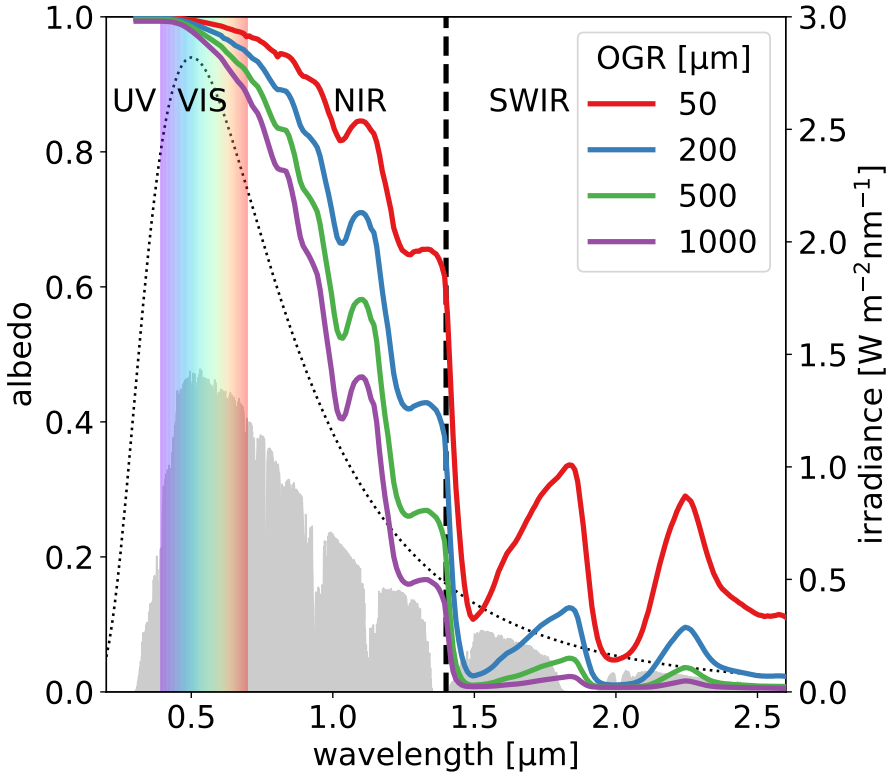

Figure 2.1: Spectral albedos of snow with different optical grain radii (OGR) simulated with the Snow, Ice, and Aerosol Radiation (SNICAR) model (Flanner et al., 2007, 2009). The dotted black curve shows the black body irradiance of the sun received by the earth. The grey area shows the direct normal spectral irradiance at the earth's surface, based on the American Society for Testing and Materials Terrestrial Reference Spectra (modelled using the Simple Model for Atmospheric Transmission of Sunshine, vesion 2.9.2; Gueymard (2001); Gueymard et al. (2002)). UV is the ultraviolet, VIS the visible, NIR the near infrared, and SWIR the shortwave infrared range of the electromagnetic spectrum.

2.1.1 Light-absorbing impurities in snow and ice

Snow metamorphism leads to a drop in spectral albedo that mainly occurs in the NIR spectrum (see solid lines in Figure 2.1). However, observations of spectral snow albedo in some aged snowpacks further revealed low spectral albedo in the visible spectrum observed that cannot be caused sole by snow metamorphism (Wiscombe and Warren, 1980; Aoki et al., 2000, e.g.,).

Instead, Wiscombe and Warren (1980) and Warren and Wiscombe (1980) hypothesized that trace amounts of absorptive impurities occurring in natural snow can lead to significant implications for snow albedo. To date, many studies support this hypothesis (Doherty et al., 2010; Forsström et al., 2013; IPCC, 2013; Wang et al., 2013; Qian et al., 2014b). Particles that have

the ability to absorb electromagnetic waves in the short wavelength range caught the attention of the research community due to their influence on water and energy budgets of both the atmosphere and the earth surface (e.g., Twomey et al., 1984; Albrecht, 1989; Hansen et al., 1997; Ramanathan et al., 2001; Lau and Kim, 2006; Flanner et al., 2007; Qian et al., 2009, 2011; Bond et al., 2013). These particles originate from fossil fuel combustion and forest fires in the form of Black Carbon (BC) and Organic Carbon (OC) (Bond et al., 2013; AMAP, 2015), mineral dust (Painter et al., 2012b), volcanic ash (Rhodes et al., 1987), organic compounds in soils (Wang et al., 2013), and biological activity (Lutz et al., 2016). Some of these have remote sources and undergo long distance atmospheric transport, interacting with their surroundings (Figure 2.2): The airborne particles warm the troposphere by absorbing solar radiation, which raises the internal energy of the particles and causes them to increase in temperature. The subsequent increased emission of predominantly infrared radiation (following Planck's law (Planck and Masius, 1914)) is then absorbed by surrounding air molecules, causing an increase in air temperature. In turn, the absorption lowers the amount of shortwave radiation penetrating through the atmosphere, and thus has a cooling effect at the earth's surface. The impact on solar heating in the atmosphere and at the surface can alter atmospheric stability and thus has the potential to impact atmospheric circulation (Kim et al., 2015). In addition to the radiative effect, the particles can act as cloud condensation nuclei and thus influence the formation of clouds and impact precipitation (Dusek et al., 2006; Zhang et al., 2008; Maskey et al., 2017).

If these aerosols are deposited alongside snowfall, they lower the spectral albedo of the snow in the shortwave spectrum (dashed purple line in Figure 2.3), and act in a similar way as their airborne counterparts by emitting infrared radiation (Figure 2.2). Due to the efficient absorption properties of snow grains in the thermal infrared, this leads to heating of the snow. This in turn has implications for the evolution of the snow micro-structure (Flanner et al., 2007) and snow melt.

In this thesis, particles (airborne or deposited) that have the ability to absorb in the shortwave spectrum are referred to as LAP (light-absorbing particles), whereas LAISI (light-absorbing impurities in snow and ice) is only used to refer to LAP mixed with snow.

2.1.2 Modelling snow albedo

Having a high temporal variability, the albedo of snow is a major controlling factor in the surface energy balance of snow covered areas. A good representation of snow albedo is therefore paramount in numerical models (in this thesis simply referred to as "models") that aim to simulate the spatial and temporal evolution of snow.

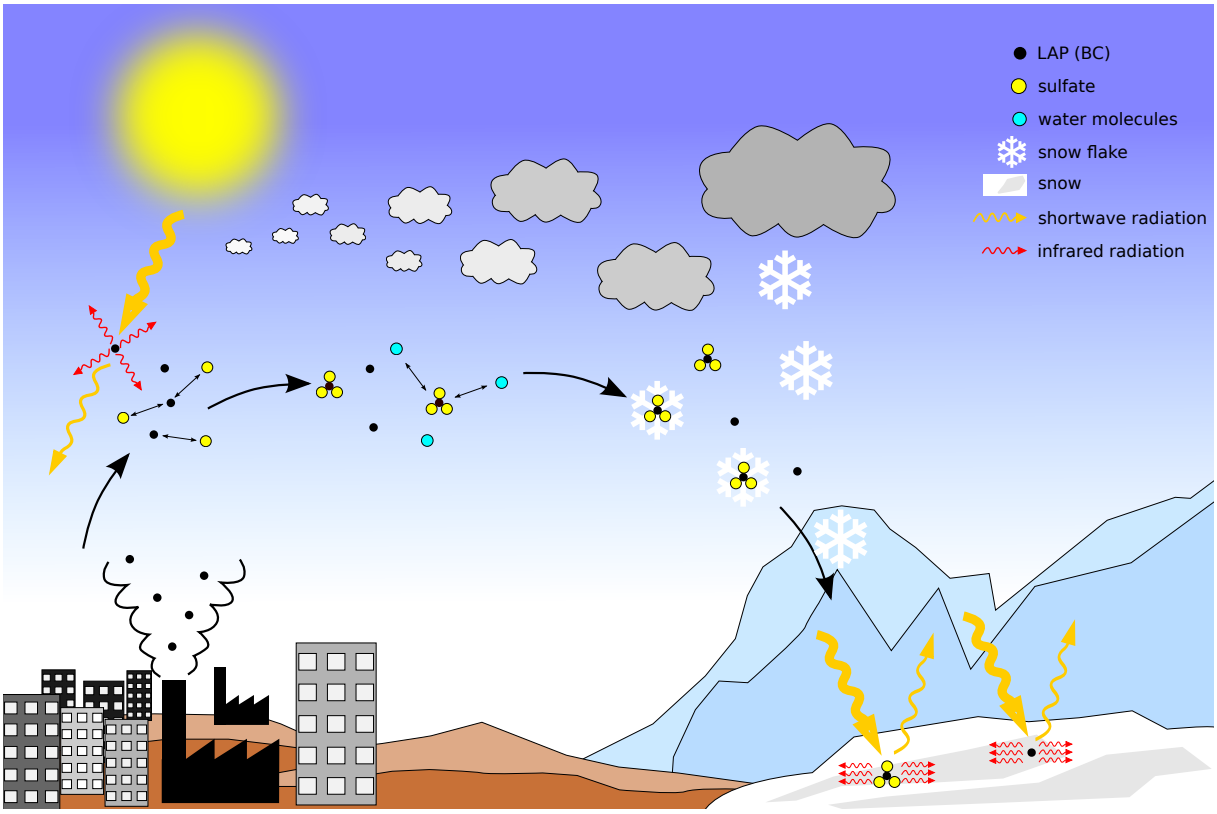

Figure 2.2: Schematic drawing of Black Carbon (and other light-absorbing particles) pathways and processes in the atmosphere and snow.

In various models, a range of approaches is used to capture the variability of snow albedo. The direct integration of observations is one possibility, however, observations of albedo are often only fragmentary available both in space and time, require expensive instrumentation and maintenance, and are therefore often not suitable for use in model applications. Even though satellite observations of snow albedo are common and offer large spatial coverage, retrievals are limited to clear sky areas and associated with large uncertainties, particularly over complex terrain. For this reason, the direct integration of observation in models is challenging and often impractical. Instead, models resolving the surface energy balance are usually coupled to a snow albedo model. Very common is the integration of empirical parametrizations based on observations. These parametrizations are usually mathematically simple and computationally fast, and do not require sophisticated knowledge about the physical state of the snowpack and the atmosphere. However, due to their simplicity these parametrizations often ignore certain variables impacting the albedo, such as incident irradiation characteristics and the presence of LAISI. Furthermore, the drop in albedo over time, though usually represented as a temporal

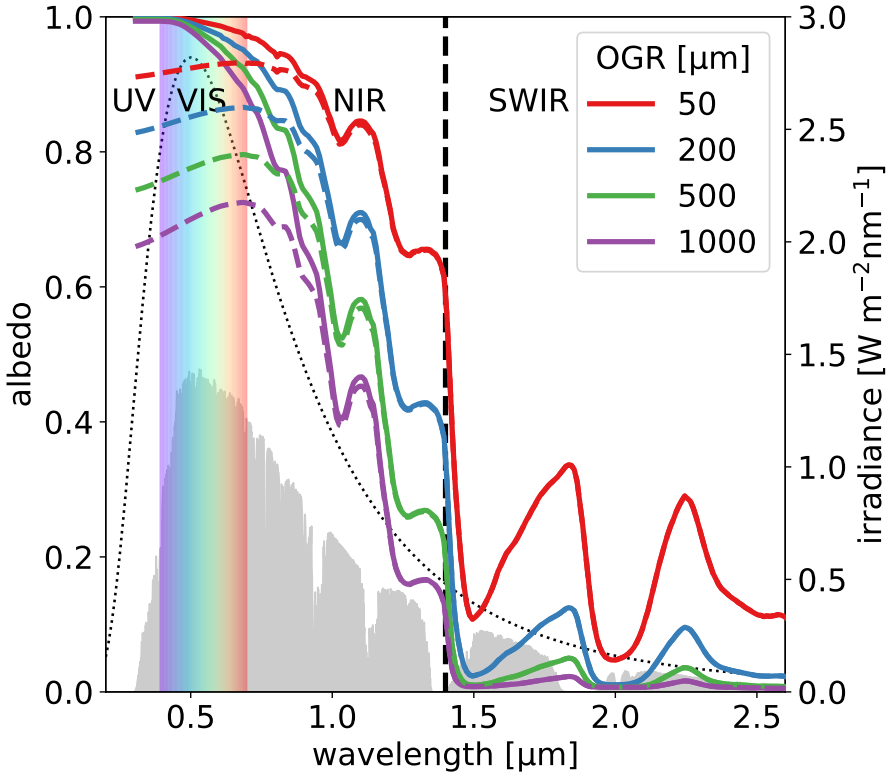

Figure 2.3: Spectral albedos of snow with different optical grain radii (OGR) and Black Carbon (BC) content simulated with the Snow, Ice, and Aerosol Radiation (SNICAR) model. Solid lines show spectral albedos of clean snow and dotted lines show spectral albedos of snow with 500 ng g^{-1} BC. Black body irradiance (black dotted line) and spectral irradiance at the earth's surface (grey area) are described in Figure 2.1.

decay function, is decoupled from the snow metamorphism causing it. Only few attempts exist to determine broad band albedo in a physically consistent approach (Marshall, 1989; Brun et al., 1992; Gardner and Sharp, 2010), wherefore broad band albedo is usually determined from empirical parametrizations (e.g., Brock et al., 2000; Pedersen and Winther, 2005).

For simulating the spectral albedo of snow, a range of physically based models have been developed (Wiscombe and Warren, 1980; Flanner et al., 2007, 2009) giving reliable results when comparing with measurements (e.g., Hadley and Kirchstetter, 2012). However, they are computationally more expensive and demanding in their input data requirements. For this reason, the implementation of such approaches in spatially distributed numerical models with already high computational needs was impractical until recently. As computational potential increased continuously over the last decades (Moore, 2006; Keyes, 2006), these approaches have been implemented in multilayer point models (Tuzet et al., 2017), regional climate models (Oaida et al.,

2015), and global climate models (Flanner et al., 2007) in order to better represent process based mechanisms and snow sensitivity to boundary forcing variables.

2.1.3 Modelling the spectral albedo of snow

In this Section, the widespread and well established approach to describe snow grains as spheres is introduced. Snow albedo is then a function of the scattering properties of these spheres, potential absorbers mixed within the snow, and the spectral and angular distribution of incoming electromagnetic radiation.

To determine the spectral scattering properties of the snow continuum (multiple scattering), one needs to know the single scattering properties of each component (i.e. snow grains, impurities). These properties are defined by three dimensionless parameters: the absorption efficiency Q_a, the scattering efficiency Q_s, and the asymmetry factor g, describing the mean cosine of the scattering angle.

For retrieving these quantities, the most widely used approach describes snow grains as spheres (Wiscombe and Warren, 1980; Flanner et al., 2007, 2009), even though shapes of naturally occurring snow grains usually strongly deviate from spherical shapes (Lachapelle, 1969). It has been shown that assuming a collection of spheres with the same specific surface area (SSA) A_s (surface area per unit of mass) as the snow grains, is a well suited approximation (Wiscombe and Warren, 1980; Hadley and Kirchstetter, 2012). The area weighted radius of the spheres r relates to A_s as

$$r = \frac{3}{\rho_i \cdot A_s}, \tag{2.4}$$

with $\rho_i \approx 917$ kg m^{-3} the density of ice. In the literature, r is normally referred to as *effective grain radius* or *optical grain radius* (OGR). Approximating snow grains as spheres then allows the use of a known set of equations describing the scattering of light by small particles, where the scattering particle is of comparable size to the wavelength λ of the scattered electromagnetic wave. This set of equations is widely known as *Mie theory* (e.g., van de Hulst, 1957; Wiscombe, 1980). These equations require as input the complex refractive index of ice

$$m(\lambda) = m_{re}(\lambda) + m_{im}(\lambda) \tag{2.5}$$

and the dimensionless parameter $2\pi r_s/\lambda$. The complex refractive index accounts for refraction (real part $m_{re}(\lambda)$) and attenuation due to absorption (imaginary part $m_{im}(\lambda)$) of light passing through ice. Examples of measured $m(\lambda)$ are given in Figure 2.4.

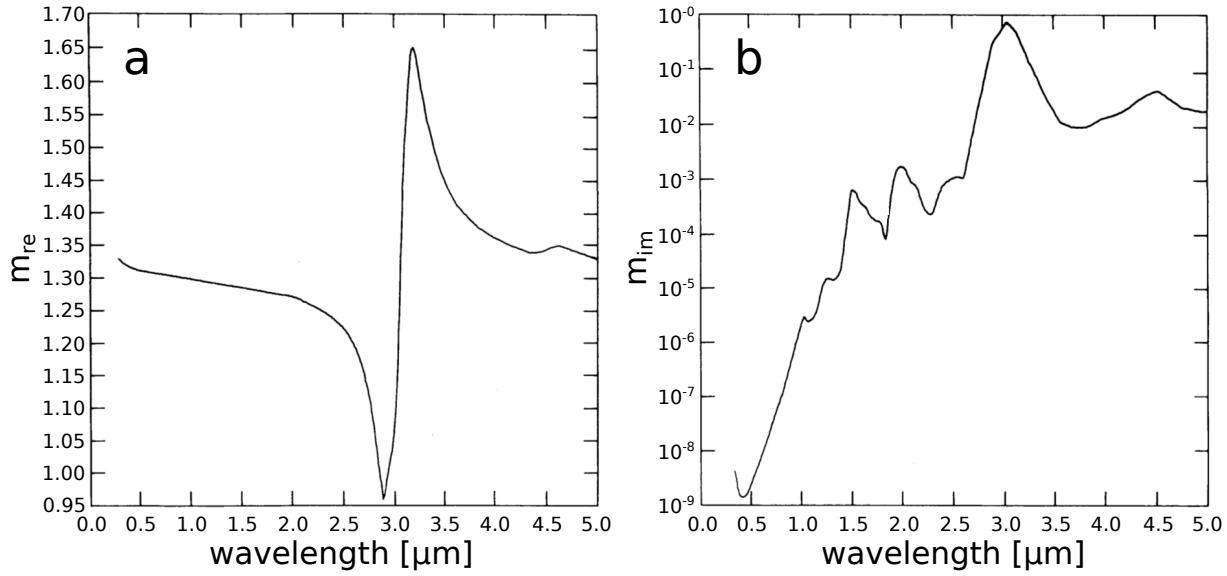

Figure 2.4: Real and imaginary part of the refractive index of ice at -7°C. Modified from Wiscombe and Warren (1980).

Using the determined single scattering properties of ice grains, it is then possible to determine the spectral albedo of a snowpack from multiple scattering using a radiative transfer model. Widely accepted is the Delta-Eddington approximation (Joseph et al., 1976) due to its ability to handle anisotropic scattering (snow grains strongly forward-scatter) (Wiscombe and Warren, 1980; Dang et al., 2016).

Based on the approach described above, Wiscombe and Warren (1980) and Warren and Wiscombe (1980) developed a robust and elegant model for snow albedo that remains today as a standard. Critical to their approach was the ability to account for the strongly forward-scattering snow grains, the large variability in ice absorption with wavelength, and both diffuse to direct beam radiation at the surface. Furthermore, and of particular importance to the success of the approach, the model relies on observable instead of tunable parameters:

λ the wavelength of radiation

$m(\lambda) = m_{re}(\lambda) + m_{im}(\lambda)$ the complex refractive index of ice

r the mean snow grain radius (also called optical grain radius, OGR)

μ_0 the cosine of the solar zenith angle θ_0

h the ratio of diffuse to total (diffuse + direct) incident flux

s the snow water equivalent (SWE) of the snowpack

α_g the albedo of the underlying ground

Based on this work, Flanner et al. (2007, 2009) developed the Snow, Ice, and Aerosol Radiative (SNICAR) model, a multilayer radiative transfer model for snow that allows to simulate snow albedo for arbitrary snow conditions and number of LAISI at any concentration.

2.2 Snow-albedo feedbacks

The interplay of mechanisms by which LAP impact the troposphere is complex and to date uncertainties on impact estimates are high (Flanner et al., 2009; IPCC, 2013).

At the surface, the darkening effect of LAISI has a warming effect on the snow, which impacts snow microphysics. Many studies hypothesize that a small initial snow albedo reduction may have a large net forcing due to a number of feedbacks, all of which resulting in an amplification of the radiative forcing (e.g., Flanner et al., 2007; Qian et al., 2009; Bond et al., 2013):

1. The LAISI induced surface darkening has the potential to accelerate snow ageing, leading to a faster increase in OGR. The albedo of snow is generally lower for snow with larger OGR (see Figure 2.1). Furthermore, LAISI absorb more efficiently in snow with larger OGR (see Figure 2.3). For this reason, the mechanism further lowers snow albedo and increases snow melt (Flanner and Zender, 2006; Flanner et al., 2007; Hadley and Kirchstetter, 2012).

2. During melt, LAISI may retain in the snow and accumulate at the snow surface, which further darkens the snow surface and accelerates snow melt (Conway et al., 1996; Xu et al., 2012; Doherty et al., 2013). This effect is referred to as *melt amplification* (Doherty et al., 2013). The magnitude of the positive feedback through the LAISI enrichment depends on the scavenging efficiency, describing how effective LAISI are entrained with melt water (Flanner et al., 2007; Qian et al., 2014a).

3. Due to accelerated melt, the darker underlying surface is exposed earlier leading to the well-known *snow albedo feedback* (Hansen and Nazarenko, 2004; Serreze and Francis, 2006; Flanner et al., 2007; Hadley and Kirchstetter, 2012).

Accounting for the above listed feedbacks, modelling studies suggest that LAISI induced snow darkening is more efficient in accelerating snow melt than any other anthropogenic agent (Hansen et al., 2005; Flanner et al., 2007; Qian et al., 2011).

2.3 Climatic and hydrologic response to light-absorbing impurities in snow and ice

Even though the impact of LAISI on snow albedo is known since the 1970s (e.g., Higuchi and Nagoshi, 1977; Warren and Wiscombe, 1980; Grenfell et al., 1981; Clarke and Noone, 1985), it took until the 2000s for the topic to gain traction, when several studies showcased the importance of LAISI on different scales (e.g., Hansen and Nazarenko, 2004; Jacobson, 2004; Flanner et al., 2007; Painter et al., 2007).

Model studies investigating the climatic impacts on a global scale state that BC in snow causes a surface warming on the northern hemisphere, with a climate efficacy of BC-in-snow that is by a factor of 2-4 larger than that of CO_2 (Hansen and Nazarenko, 2004; Jacobson, 2004; Hansen et al., 2005; Flanner et al., 2009; Koch et al., 2009; Shindell and Faluvegi, 2009). The large efficacy implies that the climatic impacts are likely to be larger than instantaneous forcing estimates suggest (Qian et al., 2014b).

On a regional scale, most modelling studies investigating climatic and hydrologic impacts of LAISI focus on mountainous regions such as the Tibetan Plateau (TP), the Colorado mountain range (e.g., Painter et al., 2012b; Skiles et al., 2012), the Alps (e.g., Di Mauro et al., 2015; Gabbi et al., 2015), and the Andes (e.g.,see Molina et al., 2015, for a review of studies). The Tibetan Plateau and Himalaya (TPH) has been pointed out to be a region of specific importance due to a number of reasons. Due to its vicinity to some of the largest sources of BC emissions of the world (Bond and Bergstrom, 2006; Bond et al., 2013) such as the Indo-Gangetic Plain (Ramanathan et al., 2007), especially the southern side of the TPH is exposed to high deposition of LAP. In response to the increased anthropogenic LAP emissions from these sources, BC and OC levels extracted from Himalayan ice cores indicate a significant increase in deposition on the TP since 1990 (Ming et al., 2008; Kaspari et al., 2011) and model studies suggest that the TP receives the highest radiative forcing from LAISI globally (Flanner et al., 2007; Qian et al., 2011). Furthermore, westerly winds advect large amounts of mineral dust from Southwest Asia and the Thar Desert into the Indo-Ganges planes, with occasional outbreaks over the southern side of the Himalayas (Hegde et al., 2007; Prasad and Singh, 2007; Gautam et al., 2011, 2013; Duchi et al., 2014). Due to the large role that the TPH plays in the monsoon circulation and the Asian hydrological cycle (Qian et al., 2011), and the large surface water resources stored in snow and ice, LAISI implications in this region captured the interest of scientists and water resource managers.

There is broad consensus on the primary role of increasing greenhouse gas concentrations as driver of accelerated melting of snow and glaciers on a global scale (Barnett et al., 2005).

However, the above-average increase in warming and retreat of glaciers in the TPH region gives rise to the hypothesis that additional mechanisms are driving these changes (Xu et al., 2009). The heating of the atmosphere by LAP and increased snow and glacier melt caused by LAISI has the potential to account for these at least partially (Ramanathan and Carmichael, 2008; Lau et al., 2010; Qian et al., 2011). Qian et al. (2011) used a global climate model to simulate the effect BC and mineral dust in snow have on the hydrological cycle of the TP. They found a significant impact on the hydrology, with runoff increasing during late winter/early spring and decreasing during late spring/early summer due to a trend towards earlier melt dates. However, detailed modelling at the catchment scale was not conducted.

With respect to hydrologic impact studies outside the TPH, most focus has been on the western United States (Painter et al., 2007, 2010; Qian et al., 2009; Oaida et al., 2015). In the Rocky Mountains, dust deposition increased fivefold in comparison to the mid nineteenth century, most likely due to human activities altering surface sediments that caused an increase in wind erosion (Neff et al., 2005). Painter et al. (2010) showed that dust, deposited to snow in the Colorado River basin, can have severe implications for the hydrological regime due to disturbances to the discharge generation from snowmelt during the spring time. They observed a shifting in the peak runoff by several weeks and leading to earlier snow-free catchments and a decrease in annual runoff. Qian et al. (2009) simulated hydrological impacts due to BC deposition in the western United States using the Weather Research and Forecasting Model (WRF) coupled with chemistry (WRF-Chem). They found a decrease in net snow accumulation and spring snowmelt due to BC-in-snow induced increase in surface air temperature. Oaida et al. (2015) implemented radiative transfer calculations to determine snow albedo in the Simplified Simple Biosphere land surface model of the WRF regional climate model. They showed that physically based snow albedo representation can be significantly improved by considering the deposition of light-absorbing aerosols on snow over the western United States.

2.4 Gap of knowledge

The governing processes to enable LAISI calculation have been implemented in a variety of models. To date, models of different scales consider the effects of LAISI, ranging from multi-layer point models (Tuzet et al., 2017), to regional (Oaida et al., 2015), and global (Flanner et al., 2007) climate models. However, only very few studies investigate the effect at the catchment scale.

Using the Variable Infiltration Capacity model, Painter et al. (2010) studied implications from dust radiative forcing in snow on runoff from the Upper Colorado River Basin. They found that

the peak runoff occurs on average three weeks earlier nowadays compared to the beginning of the 20th century due to increased dust deposition resulting from anthropogenic activities.

Despite these efforts, the direct integration of deposition mass fluxes of LAP in a catchment model is still lacking. To date, there is no rainfall-runoff model with focus on runoff forecast at the catchment scale that is able to consider atmospheric LAP deposition mass fluxes and subsequent implications from LAISI. On the other hand, there is evidence that including the radiative forcing of LAISI has the potential to improve the quality of hydrological predictions. Bryant et al. (2013) showed that during the melt period errors in the operational stream flow prediction of the National Weather Service Colorado Basin River Forecast Center are linearly related to dust radiative forcing in snow. They concluded that implementing the effect of LAISI on the snow reflectivity could improve hydrological predictions in regions prone to deposition of light-absorbing aerosols on snow, which emphasizes the need for development of a suitable model approach. Furthermore, we continuously move towards hydrological models with an increasing complex representation of the physical processes involved in the evolution of the seasonal snowpack. Heretofore there has been little focus on the factors related to LAISI, such as the impact of aerosol deposition on snow albedo, that may alter the timing and character of discharge generation at the catchment scale.

In this thesis, this deficiency is addressed by introducing a rainfall-runoff model with a newly developed snow algorithm that allows for a new class of model input variables: the deposition mass flux of different species of light-absorbing aerosols. The model integrates snowpack dynamics forced by LAISI and allows for analysis at the catchment scale. The algorithm uses a radiative transfer model for snow to account dynamically for the impact of LAISI on the snow albedo and the subsequent impacts on the snow melt and discharge generation. Aside from enabling the user to optionally apply deposition mass fluxes as model input, the algorithm depends on standard atmospheric input variables, such as precipitation, temperature, shortwave radiation, wind speed, and relative humidity.

3 Methodologies

3.1 Hydrologic modelling with Shyft

All hydrological analysis presented in this thesis are conducted with Statkraft's Hydrologic Forecasting Toolbox (Shyft). Shyft is a modern and open source (`https://gitlab.com/shyft-os`) modelling platform that provides distributed hydrological analysis in research and water management applications targeting the fields of hydropower production, flood forecasting, water resource management, and impact assessment. The model framework is developed by Statkraft AS in collaboration with the University of Oslo. In the current state, the platform supports several hydrological models with focus on snow covered regions and is introduced in Paper I of this thesis.

The concept of Shyft follows the idea that a hydrological model can be expressed as a sequence of algorithms that aim to represent a conceptual component of the hydrological system. Examples of such components are evapotranspiration, snow accumulation/melt processes, and soil water response. These algorithms (or methods) can then be combined to a sequence, the so called method-stack or model. Shyft provides a standard set of methods and models, but also aims to provide the user with the flexibility to implement their own contributions or to re-arrange provided methods into new models.

The sequence of methods is then run on a cell by cell basis, where the cell loosely represents an area of similar time-invariant geographical data (e.g. topographic properties or land type) with (to date) no specific restriction to cell geometry or area. Cells can be grouped to catchments and regions (a collection of catchments), and model calibration can be performed on the catchment and region level, as well as the cell level. In every aspect, Shyft is optimized for highly efficient simulation of hydrological processes.

The objectives of Shyft are to:

- provide a flexible hydrologic forecasting toolbox built for operational environments
- enable highly efficient and rapid calculations of hydrologic response at the region scale

- allow for using the multiple working hypothesis (Clark et al., 2011) to obtain an optimal catchment forecast

- create a mechanism for rapid implementation of improvements identified through research activities

In particular the first two objectives require computational efficiency and a software architecture that allows test coverage of all aspects of the software. Shyft uses the latest C++ standards and makes use of the utility of C++ template concepts in order to provide a flexible software for use in both business critical applications and research. All components of the framework are exposed to the user via an Application Programming Interface supporting both C++ and Python. In order to demonstrate the functionality of Shyft we developed an interactive documentation for various aspects of the model using Jupyter Notebooks (`https://gitlab.com/shyft-os/shyft-doc`).

3.2 Shyft Method Stack

Currently, several method-stacks are supported in Shyft (Figure 3.1). In additions to the "default" method-stacks described in this Section, a modular adaptation of the popular and widely used HBV model (Bergström, 1976, 1995) is implemented in Shyft. A well documented description of the HBV model can be found in Seibert and Vis (2012). The method-stacks are described below. Due to the (to date) primary application of Shyft in seasonally snow covered regions, the focus was particularly directed towards the representation of snow accumulation/melt processes in the early stages of development. For this reason, the method stacks differ mainly in the algorithms targeting snow processes (Section 3.2.4).

3.2.1 Hydrologic response

In all method stacks except the HBV-stack, the cell response to precipitation and snow melt is determined using the approach of Kirchner (2009), who describes catchment discharge from a simple first order nonlinear differential equation. The underlying assumption of the approach is that the discharge is only a function of the liquid water in storage in the catchment, such that

$$Q = f(S) \tag{3.1}$$

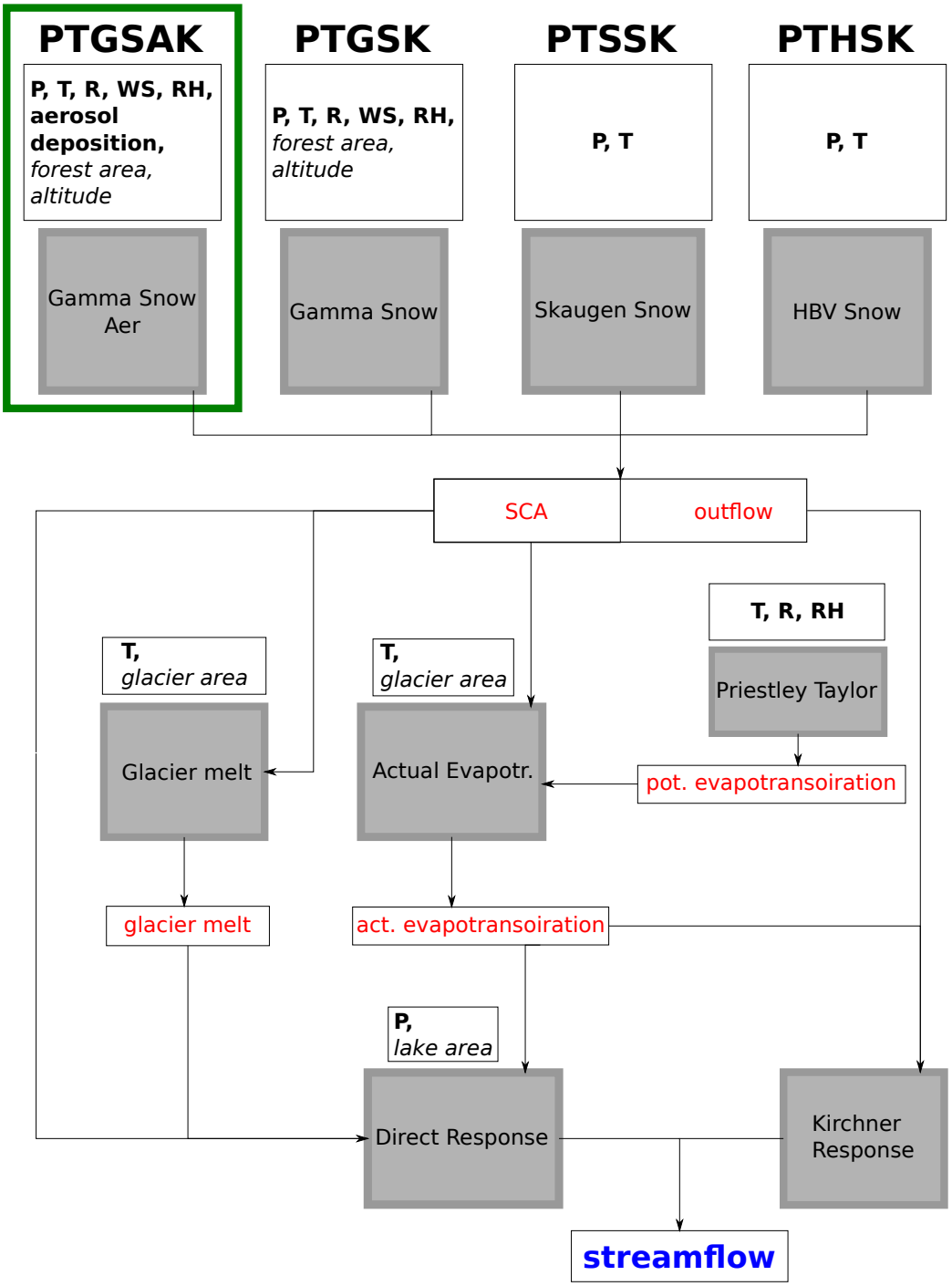

Figure 3.1: Sketch showing the structure of available method-stacks in Shyft. Methods are shown in grey boxes, input variables are listed in big font, static cell data are shown in italic, and response variables passed between methods are marked in red. The green box marks the contribution developed during the work for this thesis.

where Q is the catchment discharge, S is the liquid water storage, and the $f(S)$ the functional relationship between Q and S, which is required to be invertible. Using the conservation-of-mass equation for a catchment,

$$\frac{dS}{dt} = P - E - Q, \tag{3.2}$$

Kirchner (2009) finds the first order differential equation

$$\frac{dQ}{dt} = g(Q)(P - E - Q), \tag{3.3}$$

where $g(Q)$ (called the "sensitivity function") is the derivative with respect to S of the inverse of $f(S)$. $g(Q)$ can be estimated from the observed discharge alone for periods of the discharge time series for which the catchment precipitation (P) and evapotranspiration (E_a) can be neglected. Kirchner (2009) uses the discharge time series of two catchments governed by humid climate and mild and snow poor winters (the Plynlimon catchments in mid-Wales; for more information see Robinson et al. (2013)), and recession plots to estimate $g(Q)$. He finds

$$ln(g(Q)) \approx c_1 + c_2 ln(q) + c_3 (ln(Q))^2 \tag{3.4}$$

with c_1, c_2 and c_3 being the only catchment specific parameters. To then solve Equation (3.3) numerically using Equation (3.4), Kirchner suggests to log-transform Equation (3.3) due to a "smoother" profile of the log-transformed function:

$$\frac{d(ln(Q))}{dt} = \frac{1}{Q}\frac{dQ}{dt} = g(Q)(\frac{P - E}{Q} - 1) \tag{3.5}$$

In contrast to Kirchner's approach, we apply a slight adjustment. Firstly, we use the outflow response from the snow routine described in Sect. 3.2.4 instead of precipitation, P, to integrate Equation (3.5). This outflow can be liquid precipitation, melt water, or a combination of both. In the catchments used by Kirchner (2009) "persistent snow cover is rare". For this reason, a contribution to the liquid water storage from snow melt is not considered in Equation (3.2). Our study catchments, however, are high mountain catchments with long lasting snow cover. Thus, snow melt significantly contributes to the change in the liquid water storage, making the aforementioned adaptation necessary.

Secondly, we assume that the sensitivity function, $g(Q)$, has the same form as described in Kirchner (2009) (see Equation (3.4)) and estimate the parameters c_1, c_2 and c_3 by standard model calibration of simulated discharge against observed discharge using the Nash-Sutcliffe model efficiency (NSE) as objective function (for further details see Section 3.4.1), rather than using recession plots. Since we use a daily time step in our simulation, the identification of

periods with negligible storage contribution from precipitation (and/or from snow melt) and evapotranspiration is reduced significantly compared to using an hourly time step: Kirchner (2009) uses an hourly time step and identifies predominantly rainless night hours, which satisfy the aforementioned condition.

In contrast to the hydrologic response following Kirchner (2009), glacier melt and precipitation falling over lakes contributes directly to discharge generation without undergoing a time delay (*direct response* in Figure 3.1).

3.2.2 Glacier melt

Glacier melt is calculated using a simple degree-day model (e.g., Hock, 2003), where the amount of glacier melt M_g is calculated from a claimed linear relationship to air temperature T,

$$M_g = \begin{cases} TF_g * (T - TT_g), & \text{if } T > TT_g \\ 0, & \text{if } T \leq TT_g. \end{cases} \tag{3.6}$$

The slope of the linear relationship is described with the tunable parameter TF_g, which is typically given in units of mm h^{-1} K^{-1} or mm d^{-1} K^{-1}, depending on the model time step. TT_g is the threshold temperature beyond which glacier melt is assumed to occur.

3.2.3 Evapotranspiration

To determine the potential evapotranspiration E_p, all of the implemented method-stacks rely on the equation according to Priestley and Taylor (1972),

$$E_p = \frac{a}{H_{vap}} \cdot \frac{s(T)}{s_v(T) + \gamma} \cdot R, \tag{3.7}$$

where $a = 1.26$ is a dimensionless empirical multiplier, γ the psychrometric constant, $s_v(T)$ the slope of the relationship between the saturation vapour pressure and the air temperature T, H_{vap} the latent heat of vaporization, and R the net radiation.

The actual evapotranspiration E_a is then determined taking the available liquid water storage and the snow covered area (assuming only evapotranspiration from snow free areas) into account.

3.2.4 Snow accumulation/melt

At the time of writing this thesis, three different snow accumulation/melt algorithms are implemented, which differ in concept and complexity and are part of the open source library. A further snow algorithm was developed in the course of this thesis, and is described in detail in Section 3.3.

1. **HBV Snow**

   The least complex snow algorithm implemented originates from the HBV model (Bergström, 1976, 1995), and is conceptually similar to the glacier routine (Section 3.2.2):

   $$M_s = \begin{cases} TF_s * (T - TT_s), & \text{if } T > TT_s \\ 0, & \text{if } T \leq TT_s. \end{cases} \tag{3.8}$$

   M_s is the snow melt, TF_s the snow melt factor (typically given in units of mm h^{-1} K^{-1} or mm d^{-1} K^{-1}, depending on the model time step), and TT_s is the threshold temperature beyond which snow melt is assumed to occur and below which precipitations falls as snow. Liquid water from rain and melt is retained in the snowpack up to a certain mass fraction of SWE of the snowpack, defined by the parameter CWH. Temperatures below TT_s lead to refreezing of a certain amount M_{rf} of the liquid water content, conditioned by the refreezing parameter CFR,

   $$M_{rf} = \begin{cases} CFR \cdot TF_s \cdot (TT - T), & \text{if } T < TT_s \\ 0, & \text{if } T \geq TT_s. \end{cases} \tag{3.9}$$

   To represent sub-cell SWE distribution, snowfall is partitioned to a number of snowpack sub-sets, according to user defined redistribution factors (to multiply with snowfall). The sub-cell snowpacks then differ by the amount of SWE, and under conditions of melt, the amount of liquid water.

   Despite their simplicity, degree-day methods for determining snow (and ice) melt are widely used in cryospheric modelling due to little input data requirements, reliable forecasts of air temperature, good model performance in many regions of the world, and fast computation (e.g., Hock, 2003).

2. **Skaugen Snow**

Similar to *HBV Snow*, this method also uses a temperature index model to determine snow melt, however, an alternative approach for the representation of sub-cell snow distribution has been implemented following Skaugen and Randen (2013) and Skaugen and Weltzien (2016). In this approach, the spatial probability density function (PDF) of accumulated SWE is estimated as a correlated sum of gamma-distributed unit fields of snowfall, which are distributed in space according to a two-parameter gamma distribution (Skaugen, 2007). The resulting spatial distribution of SWE is thus temporally varying in shape and the parameters of the PDF can be described as dynamic in that they change over time as a function of snow accumulation and melt events. The choice of distribution is based on earlier studies, concluding that the gamma-distribution is appropriate to describe the spatial distribution of precipitation, SWE, and snow depth. The parameters of the distribution describing accumulation events can be estimated from observed spatial variability of precipitation at the catchment scale. This leads to a reduction of model parameters requiring calibration against observed runoff. Temporal changes in snow covered area (SCA) are derived from the spatial PDF of SWE and the intensity of melting events (Skaugen and Randen, 2013).

3. **Gamma Snow**

   This method attempts to solve the energy balance equation

$$\Delta E = K + L + H_s + H_l + H_r, \tag{3.10}$$

   where ΔE is the net energy flux at the snow surface, K is the net shortwave radiation flux, L is the net longwave radiation flux, H_s and H_l are the sensible and latent heat fluxes, and H_r is the heat contribution from rain (see Figure 3.2). The net shortwave radiation is

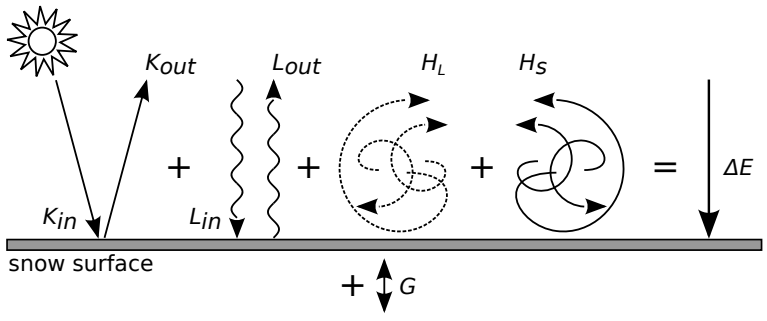

Figure 3.2: Schematic drawing of the snow surface energy balance components. Symbols are explained in the text. Motivated from Figure 1.7 in Leclercq (2012).

composed of the global radiation, K_{in}, and the reflected short wave radiation, K_{out}, which relate to each other via the snow albedo α:

$$K = K_{in} - K_{out} = K_{in}(1 - \alpha) \tag{3.11}$$

Temporal decrease in snow albedo is fast for temperatures above 0°C, following an exponential decay function, and slow for temperatures below 0°C, following a linear relationship. After snowfall larger than a pre-defined amount, the albedo is reset to the albedo of fresh snow. Incoming and outgoing longwave radiations are calculated according to the Stephan-Boltzmann law. The required snow surface temperature is approximated using a linear relationship to the air temperature (Raleigh et al., 2013).

Following Anderson (1976), a bulk-transfer approach is employed to approximate the turbulent fluxes of sensible and latent heat as functions of wind speed, temperature, and humidity, where the impact of the wind speed is represented in a linear, two-parametric wind-function.

To determine heat contribution from rain H_r, it is assumed that rain falling on top of snow is cooled from atmospheric temperature to 0°C, releasing the sensible heat

$$H_r = \begin{cases} \frac{c_p \cdot T \cdot P}{\Delta t}, \text{if } T > 0°\text{C} \\ 0, \text{if } T \leq 0°\text{C} \end{cases} \tag{3.12}$$

where c_p is the heat capacity of water, and Δt the model time step.

If Equation (3.10) results in an energy surplus, it is assumed that the surplus is consumed by snow melt, less the change in the cold content of the top 30 mm of SWE of the snowpack.

Once snowmelt is determined from Equation (3.10), the snow state is described using a snow depletion curve (SDC) approach (e.g., Liston, 1999, 2004; Kolberg et al., 2006), which relates the SCA of a model cell to the snow mass balance. This approach has been used in many studies to determine the snow state in hydrological models (e.g., Kolberg and Gottschalk, 2006, 2010; Hegdahl et al., 2016).

As mentioned above, the main focus of this thesis lies on the representation of snow in a catchment and the impact of LAISI on the snow albedo, snow melt, and the subsequent effects on the catchment discharge. To account for the effect of LAISI, we developed a new energy balance based snow accumulation and melt routine, described in the following section.

3.3 A new snowpack model accounting for LAISI

We developed a snowpack routine that allows to take the impact of LAISI on albedo into account. The energy balance part of the algorithm builds up on the *Gamma Snow* routine introduced in Section 3.2.4. However, significant changes have been introduced to the calculation of the snow albedo and the representation of the sub-grid snow distribution, which are presented herein.

To represent the evolution of LAISI mixing ratios near the snow surface, we introduce two snow layers in our model. The surface layer has a time invariant maximum thickness (further called maximum surface layer thickness). The mixing ratio of each LAISI species in this layer is calculated from a uniform mixing of the layer's snow with either falling snow with a certain mixing ratio of aerosol (wet deposition), or aerosol from atmospheric dry deposition. Following Krinner et al. (2006), we apply a maximum surface layer thickness of 8 mm SWE. Krinner et al. (2006) suggests this value based on observations of 1 cm thick dirty layers in alpine firn cores used to identify summer horizons. The second layer (bottom layer) represents the snow exceeding the maximum thickness of the surface layer and has no upper limit.

3.3.1 Melt amplification

The introduction of two layers allows to account for melt amplification. LAISI mass fluxes between the two layers are accounted for during snow accumulation and melt. Generalizing Jacobson (2004)'s representation of LAISI mass loss due to meltwater scavenging for multiple snow layers, we characterize the magnitude of melt scavenging using the scavenging ratio k_i and calculate the temporal change of LAISI mass $m_{s,i}$ of LAISI species i in the surface layer as

$$\frac{dm_{s,i}}{dt} = -k_i q_s c_{s,i} + D_i \tag{3.13}$$

and the change of LAISI mass $m_{b,i}$ in the bottom layer as

$$\frac{dm_{b,i}}{dt} = k_i \cdot (q_s c_{s,i} - q_b c_{b,i}). \tag{3.14}$$

Herein, q_s and q_b are the mass fluxes of melt water from the surface to the bottom layer and out of the bottom layer, respectively, and $c_{s,i}$ and $c_{b,i}$ are the mass mixing ratios of LAISI in the respective layer. D_i is the atmospheric deposition mass flux. A value for k_i of <1 is equal to a scavenging efficiency of less than 100% and hence allows for accumulation of LAISI in the surface layer during melt.

In our analysis, we account for hydrophilic BC, hydrophobic BC, and dust. Following Flanner et al. (2007), we treat aged, hydrophilic BC as sulphate coated to account for the net increase in the mass absorption cross section (MAC) by 1.5 at λ=550 nm compared to hydrophobic BC. The net increase results from the ageing of BC (reducing effect on MAC) and particle coating from condensation of weakly absorbing compounds (enhancing effect on MAC) (Bond et al., 2006). As a consequence, hydrophilic BC absorbs stronger than hydrophobic BC under the same conditions. On the other hand, hydrophilic BC undergoes a more efficient melt scavenging. Scavenging ratios of LAISI species addressed in this thesis are shown in table 3.1.

LAISI species	Scavenging ratio	Reference
hydrophilic BC	0.2	Flanner et al. (2007)
hydrophobic BC	0.03	Flanner et al. (2007)
dust	0.01	Oaida et al. (2015)

Table 3.1: Scavenging ratios of LAISI species addressed in this thesis.

3.3.2 Optical grain radius (OGR) of snow

Both the albedo of clean snow and the effect of LAISI on the snow albedo strongly depend on the snow optical grain radius r (Warren and Wiscombe, 1980), which alters as snow ages. r can be related to the snow specific surface area A_s via

$$r = \frac{3}{\rho_i \cdot A_s}, \tag{3.15}$$

with ρ_i the density of ice. A_s represents the ratio of surface area per unit mass of the snow grain (Roy et al., 2013).

In our model, we compute the evolution of A_s in dry snow following Taillandier et al. (2007) as

$$A_s(t) = [0.629 \cdot A_{s,0} - 15.0 \cdot (T_s - 11.2)] - [0.076 \cdot A_{s,0} - 1.76 \cdot (T_s - 2.96)] \ln\left\{t + \exp\left(\frac{-0.371 \cdot A_{s,0} - 15.0 \cdot (T_s - 11.2)}{0.076 \cdot A_{s,0} - 1.76 \cdot (T_s - 2.96)}\right)\right\}, \tag{3.16}$$

where t is the age of the snow layer in hours, $A_{s,0}$ is A_s at t=0, and T_s is the snow temperature. The evolution of A_s in wet snow is calculated according to Eq. (3.15) and Brun (1989) as

$$\frac{dr}{dt} = \frac{C_1 + C_2 \cdot \Theta^3}{r^2 \cdot 4\pi}, \tag{3.17}$$

where C_1=1.1· 10^{-3} mm^3 d^{-1} and C_2 = 3.7·10^{-5} mm^3 d^{-1} are empirical coefficients. Θ is the liquid water content of snow in mass percentage. $A_{s,0}$ is set to 73.0 m^2 kg^{-1} (Domine et al., 2007) and we set the minimum snowfall required to reset A_s to 5 mm SWE.

3.3.3 Modelling snow albedo using SNICAR

To solve for the effect of light absorption from LAISI on the snow albedo, we have integrated a 2-layer adaption of the Snow, Ice, and Aerosol Radiative model (SNICAR;Flanner et al., 2007, 2009) into the energy and mass budget calculations. By providing the solar zenith angle of the sun, the OGR, mixing ratios of LAISI in the snow layers, and SWE of each layer, SNICAR calculates reliably the snow albedo for a number of spectral bands (see Figure 3.3). To achieve this, SNICAR utilizes the theory from Wiscombe and Warren (1980) and the two-stream, multilayer radiative approximation of Toon et al. (1989). SNICAR is available with 470 bands at a spectral resolution of 0.01 μm covering the spectrum from 0.3 to 5.0 μm, and as a computationally optimized version using five spectral bands (0.3-0.7, 0.7-1.0, 1.0-1.2, 1.2-1.5, and 1.5-5.0 μm) (Flanner et al., 2007). In this thesis, both versions are used. The fine 470-band version is used in stand-alone simulations of Paper III. The computationally faster 5-band version is implemented in the snow algorithm introduced herein in order to maintain computational efficiency during hydrologic simulations. Flanner et al. (2007) compared results from the 5-band scheme to the default 470-band scheme in SNICAR and concluded that relative errors are less than 0.5%. Broadband albedos (see Figure 3.4) are calculated with incident fluxes that are simulated offline assuming mid-latitude winter clear- and cloudy-sky conditions.

3.3.4 Sub-grid snow distribution

In order to allow for explicit treatment of snow layers while representing sub-grid snow variability, we follow Aas et al. (2017), and assume that the sub-grid spatial distribution of each single event of solid precipitation follows a certain PDF. From this distribution we calculate multiplication factors, which then are used to assign the snowfall of a model grid cell to a number of sub-grid computational elements, the so called tiles (Aas et al., 2017). The snow algorithm described herein is executed for each of the tiles separately, providing a mechanism to account for snow spatial distribution while preserving conservation of mass. Therefore, variables related to the snow state, such as SWE, liquid water content, LAISI mixing ratios, and snow albedo differ among the tiles. To calculate the multiplication factors, we assume that the sub-grid redistributed snow follows a gamma distribution (see e.g., Kolberg and Gottschalk, 2010; Gisnås et al., 2016), determined by the coefficient of variation (CV) of SWE at snow maximum. Ex-

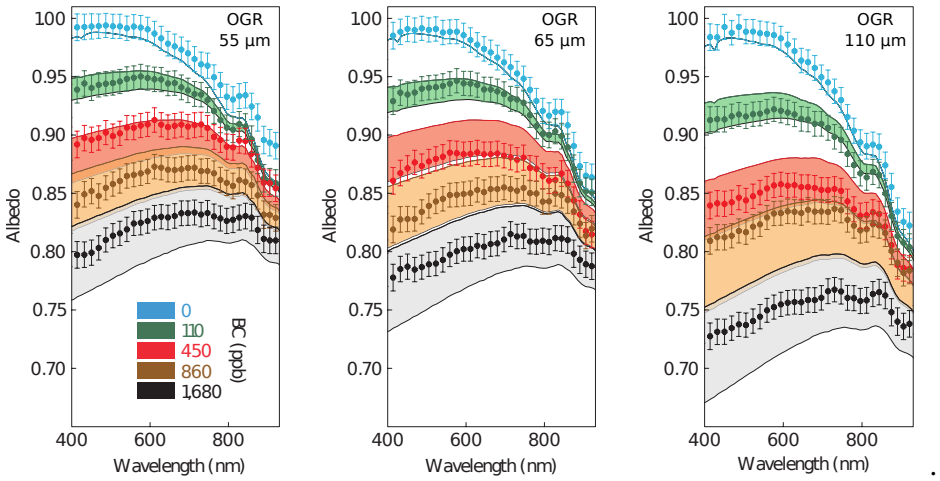

Figure 3.3: Spectral albedos of snow of different OGR mixing ratios of BC as obsereved in laboratory experiments (dots) and simulated with SNICAR (shaded bands). Error bars show the standard deviations of the measurements. Shaded bands refer to simulations assuming BC mass absorption cross-sections of 7.5 and 15 m^2 g^{-1}, respectively, at wavelength λ=550 nm. Modified from Hadley and Kirchstetter (2012).

amples of multiplication factors for forested grid cells and forest free grid cells for different CV values are shown in Fig. 3.5.

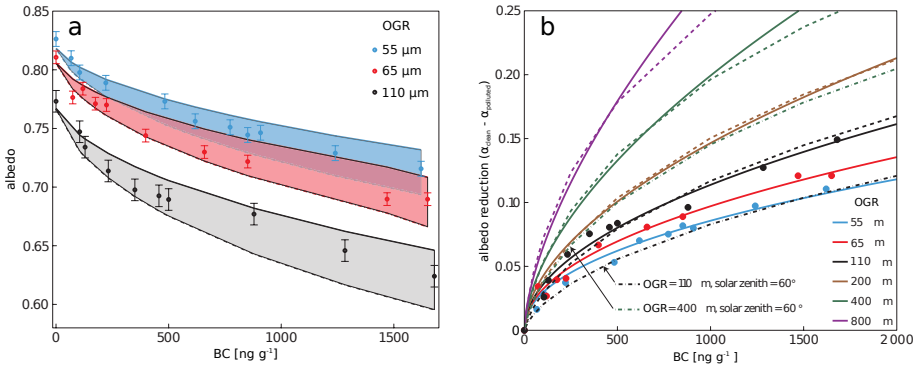

Figure 3.4: (a) Broadband albedo of snow resulting from spectral weighting over the 3-2.5 μm solar spectrum derived from experiments (dots; error bars show ±1 standard deviation) and modelled using SNICAR (shaded bands). Shaded bands refer to simulations assuming BC mass absorption cross-sections of 7.5 and 15 m^2 g^{-1}, respectively, at wavelength λ=550 nm. (b) Snow albedo reduction due to BC in snow. Circles show experimental data, solid lines are from an empirical relationship derived from the experimental data, and dashed lines are SNICAR predictions for a BC MAC of 11 m^2 g^{-1} at λ=550 nm and solar zenith angles of 0° unless otherwise specified. Both figures are modified from Hadley and Kirchstetter (2012).

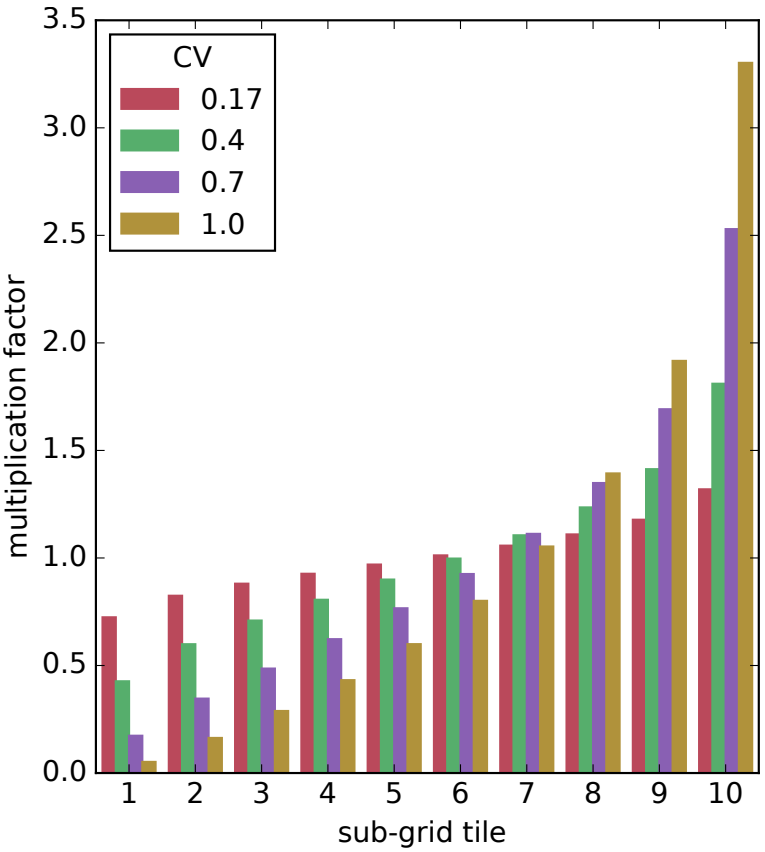

Figure 3.5: Examples of multiplication factors for different coefficients of variation (CV) computed from a gamma distribution.

3.4 Calibration and evaluation

Due to the conceptual nature of many aspects of the model used herein, the model has a number of model parameters that can assume a range of values for which the model simulates hydrologic variables within reason. The range of suitable values makes the model flexible and allows the adaption of the model to different climatic and hydrologic conditions. In order to assert quality predictions for a particular watershed, these parameters need to be estimated through model calibration. During calibration, varying sets of parameters are applied to the model and model predictions are evaluated based on a performance measure allowing to quantify the predictive power of the model.

3.4.1 Performance measures

A large number of objective functions to assess the predictive power of environmental models exist. A comprehensive review of the most important and widely used ones is given in Bennett et al. (2013). In this thesis, the following measures are used:

- **Nash-Sutcliffe Model Efficiency**
  The Nash-Sutcliffe model efficiency (NSE) (Nash and Sutcliffe, 1970)

$$E_{NS} = 1 - \frac{\frac{1}{n}\sum_{i=1}^{n}(y_i - \hat{y}_i)^2}{\frac{1}{n}\sum_{i=1}^{n}(y_i - \overline{y})^2}, \tag{3.18}$$

  allows to asses the predictive power of a model and is widely used in hydrologic modelling to investigate the ability of a model to predict discharge. In Equation 3.18, y_i is the predicted value, $\hat{y}_i$ is the corresponding observation, $\overline{y}$ is the mean of the observed data, and n is the sample size. The method compares the performance of the model to a model that always uses the mean of observations as prediction. A value of 1 indicates perfect agreement with observations, while a value of zero states that the prediction performance is equal to using the mean of observations as prediction.

- **Root-Mean-Square Error**
  The Root-Mean-Square Error (RMSE)

$$E_{RMS} = \sqrt{\frac{1}{n}\sum_{i=1}^{n}(y_i - \hat{y}_i)^2}, \tag{3.19}$$

  is a general purpose error metric for numerical predictions (e.g., Bennett et al., 2013).

- **Mean Absolute Volume Error**

$$E_{MAE} = \frac{1}{n} \sum_{i=1}^{n} |y_i - \hat{y}_i| \tag{3.20}$$

The measure is similar to the Root-Mean-Squared Error, however, the use of absolute values reduces the bias towards large events (e.g., Bennett et al., 2013).

3.4.2 Automatic calibration

Finding the best set of parameters for a model applied to a particular region is a wide field of research on its own (Madsen et al., 2002). Manual calibration relying on trial-and-error parameter adjustment is extremely time consuming and therefore impractical or even unrealistic, depending on the number of model parameters and the degree of parameter interaction. Much more effective and less time consuming are automated calibration algorithms designed for finding the global minimum on the response surface of an objective function. Most common are population-evolution-based algorithms (Madsen et al., 2002) such as genetic algorithms (Wang, 1991), shuffle complex evolution approaches (Duan et al., 1992), and simulated annealing (Sumner et al., 1997).

In this thesis, two calibration algorithms are used. Firstly, the robust general purpose evolutionary global optimization algorithm SCE-UA (Shuffled Complex Evolution - University of Arizona; Duan et al., 1992, 1994), which is widely used in conceptual model calibration (e.g., Cooper et al., 1997; Madsen, 2000; Jayawardena et al., 2006; Newman et al., 2015). Secondly, the direct search algorithm BOBYQA (Bound Optimization BY Quadratic Approximation Powell, 2009) is used, which is computationally less demanding than evolutionary methods, but nevertheless has been found to produce reliable optimization results.

4 Study Sites and Data

In this thesis, two main study sites are used, namely the Atnsjøen Catchment in Norway and the Upper Beas Catchment in the Indian Himalayas. Since the data used at each site differ immensely in how it is compiled, it is listed separately for each site. In Section 4.1 the Norwegian study site is introduced alongside data used in Paper II and in Section 4.2 the Himalayan study site is introduced together with the data used in Paper III.

4.1 Atnsjøen Catchment, Norway

The unregulated upper Atna river is located in the Rondane mountains in southern Norway (Figure 4.1a and b) and is a tributary of the Glomma river - the largest and longest river in Norway. The mountainous region lies between the two major valleys of Gudbrandsdalen and Østerdalen. The Atnsjøen watershed covers an area of 463 km^2 and ranges in elevation from 700 m above sea level (masl) at the outlet of lake Atnsjøen to over 2000 masl in the western part of the watershed (Figure 4.1c). Approximately 90% of the watershed are above the tree line (Sandlund and Aagaard, 2004).

4.1.1 Climate and hydro-meteorological observations

The catchment is located in the eastern part of southern Norway, which is characterized by continental climatic conditions (Figure 4.2). The average annual precipitation in the eastern part of southern Norway (approximately 650 mm in the study region) is much lower than in the coastal and maritime regions to the West. The amount of water stored in the seasonal snow accounts for about 50% of the annual precipitation sum (Wold, 1992), leading to the accumulation of a substantial snow pack between autumn and spring despite relatively low precipitation rates, and a strong impact of snow melt on the spring flood. Floods frequently occur in late April, May, and early June, commonly triggered by periods of warm weather and heavy rainfalls (Nesje et al., 2000). This is very distinct from the western part of southern Norway, where marine impact dominates climatic conditions along the coastal mountain ranges

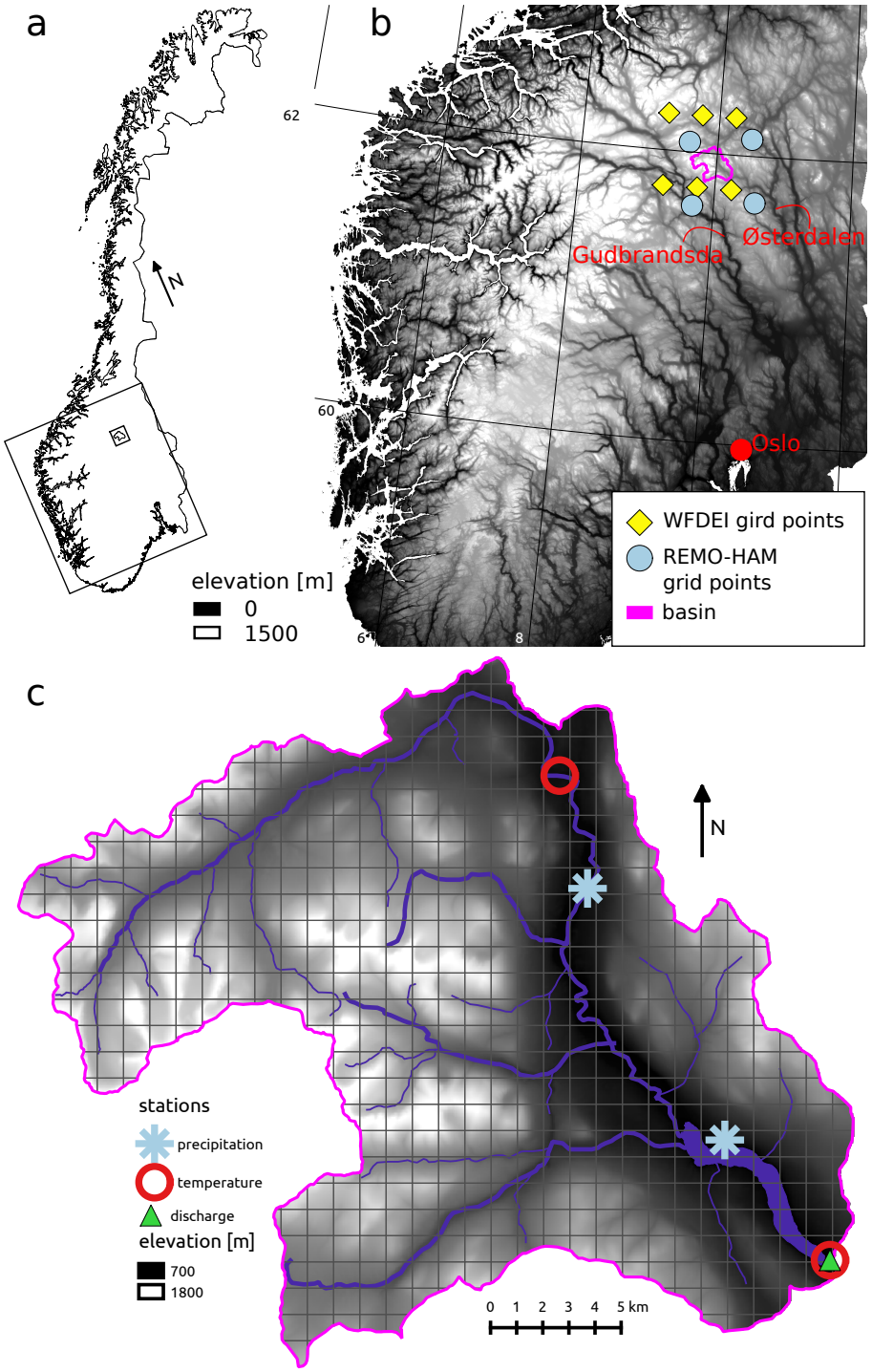

Figure 4.1: a) Map of Norway showing the image section of b) and c). b) Location of the Atnsjøen catchment in southern Norway and location of WATCH-Forcing-Data-ERA-Interim and REMO-HAM grid points close to the catchment. c) Catchment overview map showing the locations of observational stations.

and annual precipitation sums are much higher. The amount of water stored in the seasonal snow only accounts for about 25% and floods occur mainly in September through December due to periods of heavy precipitation in autumn (Nyberg and Rapp, 1998).

In our study we focused on the time period from September 2006 through August 2012. Four automatic weather stations operated by The Norwegian Water Resources and Energy Directorate (NVE) and The Norwegian Meteorological Institute (MET) have time series of meteorological variables available during in this period. The stations are located at lower elevations (between 701 and 780 masl) in the watershed along the Atna river (Figure 4.1c). Two of which measure precipitation and two measure temperature. Observations of relative humidity and wind speed are taken from stations at locations close to the watershed. Detailed information about the observational stations is given in Table 4.1.

Streamflow of the Atna river is observed at a station located at the outlet of the catchment at lake Atnsjøen (4.1c). The mean annual discharge of the Atna river is approximately 11 m^3s^{-1}, with low flows of 1-3 m^3s^{-1} during the winter months and peak flows of over 130 m^3s^{-1} driven by the spring melt season.

Station name	Station ID	Operator	Observational variable	Elevation [masl]
Atnsjøen 1	8720	MET	precipitation	749
Atndalen-Eriksrud	8770	MET	precipitation	731
Atnsjøen 2	2.32.0	NVE	temperature	701
Li Bru	2.479.0	NVE	temperature	780
Fokstuga	16610	MET	wind speed; relative humidity	973
Kvitfjell	13160	MET	wind speed	1030
Venabu	13420	MET	relative humidity	930

Table 4.1: Information on observational stations.

4.1.2 Global radiation

Due to poor availability of continuous solar radiation observations in Norway, we use for model input of global radiation gridded data from the Water and Global Change (WATCH) Forcing Data methodology Weedon et al. (2014) applied to ERA-Interim reanalysis data (Dee et al., 2011) with a resolution of 0.5° (the six nearest grid-points are shown in Figure 4.1a). The dataset is available from 1979-2012 at 3-hourly time steps. Data provided by the WATCH project is aiming for the use in regional and global studies of the hydrological cycle.

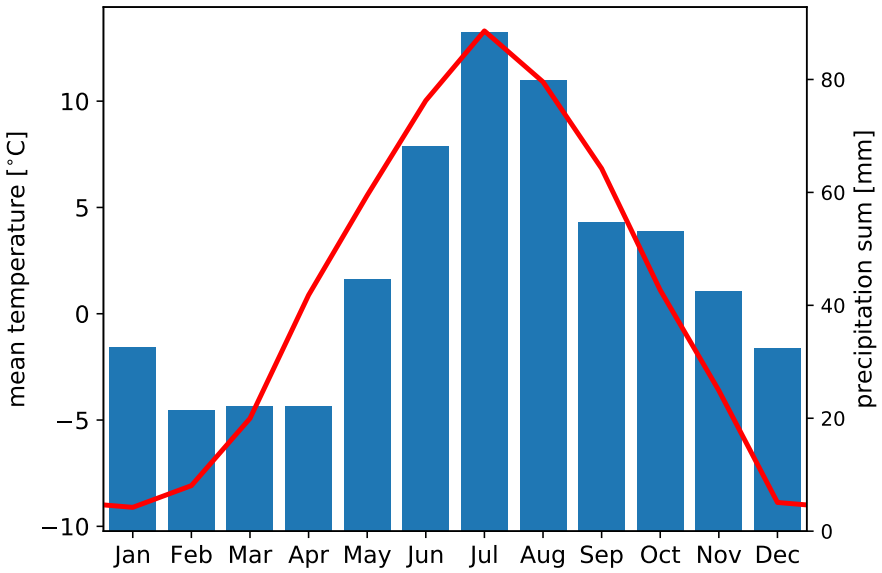

Figure 4.2: Monthly mean temperature (red) and precipitation sums (blue) at the observational stations Li Bru and Atnsjøen 1 (see Table 4.1). Monthly precipitation sums are based on data from 1957 through 2017. Temperature observations are only available from 2005 onwards.

4.1.3 BC deposition data with REMO-HAM

The wet and dry deposition rates of BC for the study area are generated using the regional aerosol-climate model REMO-HAM (Pietikäinen et al., 2012). For the simulations, we follow the approach of Hienola et al. (2013), but with changes to the emission inventory: Hienola et al. (2013) used emissions based on the AeroCom emission inventory for the year 2000 (see Dentener et al., 2006). In the REMO-HAM simulations conducted herein, emissions are made by the International Institute for Applied Systems Analysis and are based on the Evaluating the Climate and Air Quality Impacts of Short-Lived Pollutants (ECLIPSE) V5a inventory for the years 2005, 2010, and 2015 (years in between were linearly interpolated) (Klimont et al., 2017, 2016). We updated also other emissions modules (wildfire, aviation, and shipping) following the approaches presented in Pietikäinen et al. (2015). The only difference between Pietikäinen et al. (2015) and this work is that herein the Global Fire Emissions Database (GFED) version 4 based on an updated version from van der Werf et al. (2010) is used.

REMO-HAM was used for the same European domain as in Pietikäinen et al. (2012) using 0.44° spatial resolution (50 km), 27 vertical levels, and 3 minutes time step. The ERA-Interim

re-analysis data was utilized at the lateral boundaries for meteorological forcing (Dee et al., 2011) and for the lateral aerosol forcing, data from the global aerosol-climate model ECHAM-HAMMOZ (version echam6.1.0-ham2.2) was used. ECHAM-HAMMOZ was simulated in a nudging mode, i.e. the model's meteorology was forced to follow ERA-Interim data, and the ECLIPSE emissions were used (plus other updated emission modules shown in Pietikäinen et al. (2015)). The boundaries were updated every 6 hours for both meteorological and aerosol related variables. Simulations with REMO-HAM were conducted for the time period of 2004-2014 and the first three months were excluded from the analysis (spin-up period). The initial state for the model was taken from the boundary data, except for the soil parameters which were taken from a previous long-term simulation for the same domain (a so called warm-start). The output frequency of REMO-HAM was 3 hours and the total BC deposition flux was calculated from the accumulated dry and wet deposition fluxes.

4.2 Upper Beas Catchment

The Beas river rises from the Indian Himalayas in the state of Himachal Pradesh in Northwest India, from where it flows for some 470 km towards the Sutlej river, the easternmost tributary of the Indus River (Figure 4.3a). The Upper Beas basin is referred to as the drainage basin in the vicinity of the headwaters of the Beas river to the South of Rohtang Pass (Figure 4.3b). The area, located at the southern slopes of the Himalayas, is characterized by strong topographic gradients. Elevations range from 977 masl at the outlet of the basin at Thalout discharge station to over 6500 masl in the eastern part of the catchment. The total drainage area of the Upper Beas basin is approximately 4960 km^2. Some 12.6% of the area is glacier covered. In addition to the discharge station at the outlet (Thalout), there are four more discharge stations located in the Upper Beas basin (Figure 4.3b). Three of which define the sub-basins Tirthan, Sainj, and Bhuntar. The Bhuntar sub-basin is further divided in the sub-basins Parvati and Manali. For the latter no discharge observations are available.

Due to the large fraction of glaciation in the area (about 13%) and the high elevation, a significant portion of the annual water budget comes from snow and glacier melt, dominating the flow in the pre-monsoon period. However, highest flows coincide with high precipitation rates during the monsoon period (Hegdahl et al., 2016).

Meteorological conditions in the area are governed by two different weather regimes (Xu et al., 2008; Bookhagen and Burbank, 2010; Shekhar et al., 2010). While extratropical cyclones, namely the Western Distrubances, are the primary weather system causing winter precipitation, the weather during summer months is largely characterized by the Indian summer

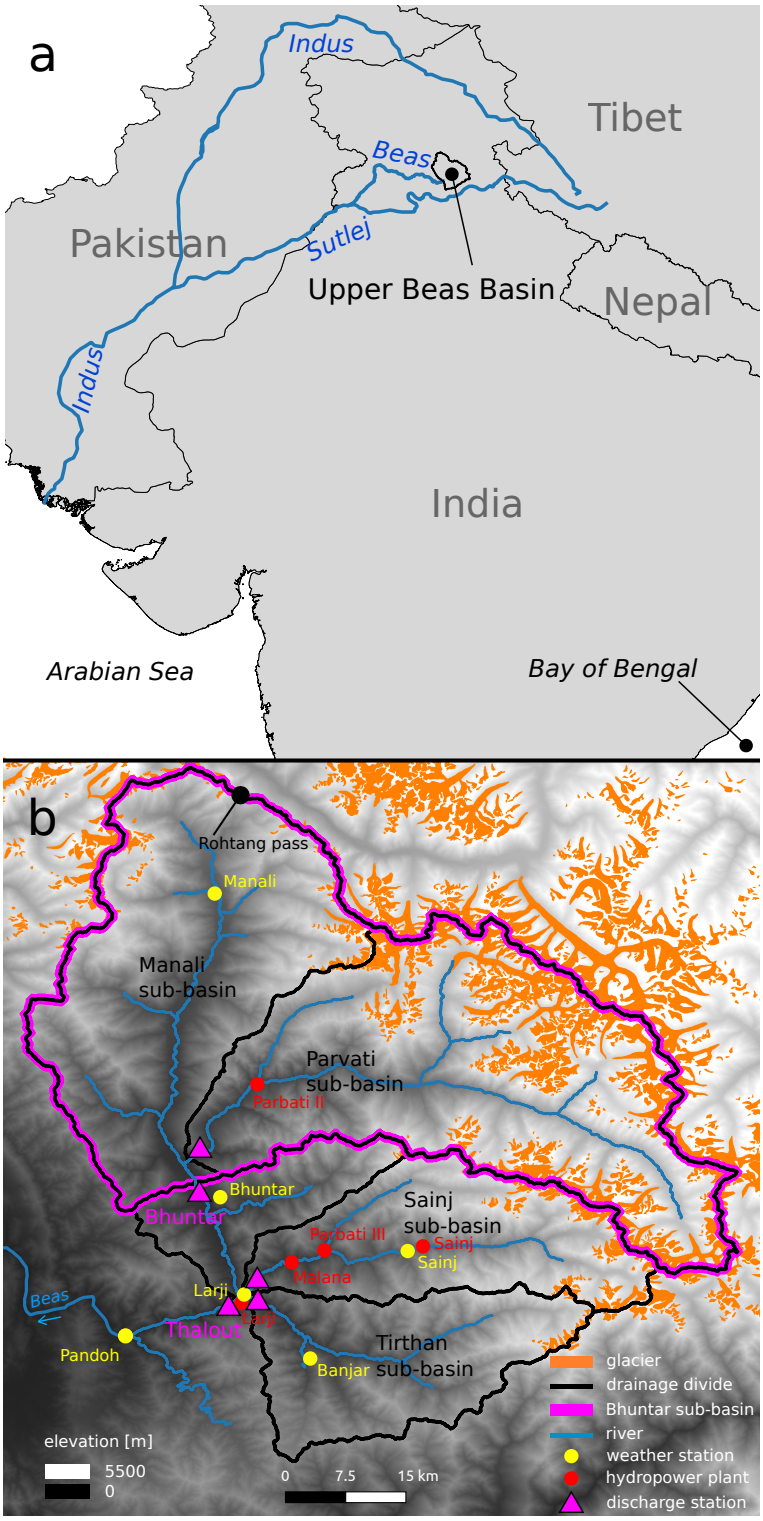

Figure 4.3: a) Location of the Upper Beas basin in India. b) Overview map of the Upper Beas basin.

monsoon. Four seasons can be defined based on monsoon activity: winter (January to March), pre-monsoon (April to June), monsoon (July to September), and post-monsoon (October to December). The generally higher elevated north and north-east are colder and drier compared to the lower valleys in the south of the catchment.

The Upper Beas basin has a large potential for hydropower activities (4.2). A total of 4 plants are under operation providing an installed capacity of 832 MW (Figure 4.3). Furthermore, parts of a large scheme are under construction and will add an additional 520 MW to the currently installed capacity. Due to the high impact of hydropower activities further downstream, we only include analysis from the Bhuntar sub-basin in our hydrologic analysis of Paper III (purple line in Figure 4.3).

The basin has been subject to numerous studies due to the availability of meteorological and hydrological observations and a high interest in hydrological studies from the Indian North focusing on hydropower potential, socio-economic relevance, and climate projections (e.g., Hegdahl et al., 2016; Kumar et al., 2007; Li et al., 2014, 2015a,b, 2017b; Singh and Kumar, 1997; Singh and Jain, 2003).

Powerplant	Capacity [MW]	Status of operation
Manala	86	in operation since 2001
Larji	126	in operation since 2007
Sainj	100	in operation since 2015
Parbati I	750	abandoned
Parbati II	800	under construction (ready 2018)
Parbati III	520	in operation since 2014

Table 4.2: Installed hydropower capacity in the Upper Beas basin. Specifications from Jain et al. (2007, p. 482) and `http://www.nhpcindia.com` (accessed 08.02.2018).

4.2.1 Meteorological observations

Daily observations are available from a network of six weather stations located in the basin measuring precipitation, temperature, and humidity. The stations are located at elevations ranging from 904 masl at Pandoh Dam, to 1971 masl at Manali (Figure 4.3b). The stations Banjar and Sainj measure only precipitation.

4.2.2 Dynamical downscaling using a mesoscale numerical weather prediction system

Several studies report data quality problems of observed meteorological variables (Hegdahl et al., 2016; Li et al., 2017b). On the one hand, hydrologic simulations suffer from the generally low altitude of station locations and related challenges with interpolation of meteorological variables to high altitude locations (Hegdahl et al., 2016): the highest station in Manali is located at 1971 masl, whereas the altitude of the Bhuntar sub-basin averages to about 3470 masl. On the other hand, data does not seem to undergo any quality control (or at least no such information is accessible to our knowledge) and even simple important measures such as geographic position and altitude of automatic weather stations are highly uncertain. Due to this limitation, we choose to dynamically downscale meteorological reanalysis data.

Aiming for high resolution meteorological forcing data for the Upper Beas basin, we conducted downscaling simulations using WRF (version 3.8.1; Skamarock et al., 2008). WRF was run with a nested approach with 1 km grid spacing for the inner domain, 5 km for the intermediate domain, and 25 km for the outer domain (Figure 4.4) from October 1999 through September 2005 (excluding a prior 3 month spin-up time). The outer domain was forced with the ERA-Interim reanalysis data (Dee et al., 2011) from the European Center for Medium Range Weather Forecasting (ECMWF). ERA-Interim comes with a spatial resolution of 0.75° and a 6 hours temporal resolution. WRF was set up with 40 vertical atmospheric levels in all domains. Land use classifications (21 categories) were derived from the Moderate-resolution Imaging Spectroradiometer (MODIS) default dataset for WRF.

The quality of precipitation data is in general of outstanding importance for hydrologic model performance (O'Loughlin et al., 1996; Syed et al., 2003; Tetzlaff and Uhlenbrook, 2005), and the choice of the microphysical scheme in WRF has significant impact on orographically induced precipitation (Cossu and Hocke, 2014). Based on the work of others focusing on a good representation of mountain precipitation in WRF (Maussion et al., 2011; Collier et al., 2013; Rasmussen et al., 2011, 2014), we find that the bulk microphysical parametrization introduced by Thompson et al. (2008) performs well and has shown to accurately reproduce precipitation over highly complex terrain (e.g., Rasmussen et al., 2011, 2014).

An overview of WRF configurations is given in Table 4.3. Furthermore, the contents of the WRF Preprocessing System files and WRF configuration files used to initiate our simulations are listed in Appendix A.

General/Grid settings	
WRF version	3.8.1
Map projection	Lambert conformal
Nr. of nested domains	2
Horizontal grid spacing	25 km, 5 km, 1 km
Unstaggered grid points (west-east x south-north)	217x185, 251x221, 301x251
Nesting approach	Two-way
Number of vertical layers	40
Time settings	
Simulation period	June 1999 - December 2005
Time step	100 s, 25 s, 5 s
Boundary/Forcing settings	
Boundary conditions	ECMWF ERA-Interim reanalysis (1°, 6 h)
Static geographical fields	MODIS standard dataset 30” spatial resolution
Spin up	3 months
Physics schemes	
Short-wave	RRTMG (Iacono et al., 2008)
Long-wave	RRTMG (Iacono et al., 2008)
Cumulus parametrisation	Tiedtke Scheme (only outer domain) (Tiedtke, 1989; Zhang et al., 2011)
Microphysics	Thompson Scheme (Thompson et al., 2008)
Land-surface model	Noah-MP (Niu et al., 2011; Yang et al., 2011)
Planetary boundary layer	Yonsei University Scheme (Hong et al., 2006)

Table 4.3: WRF configuration.

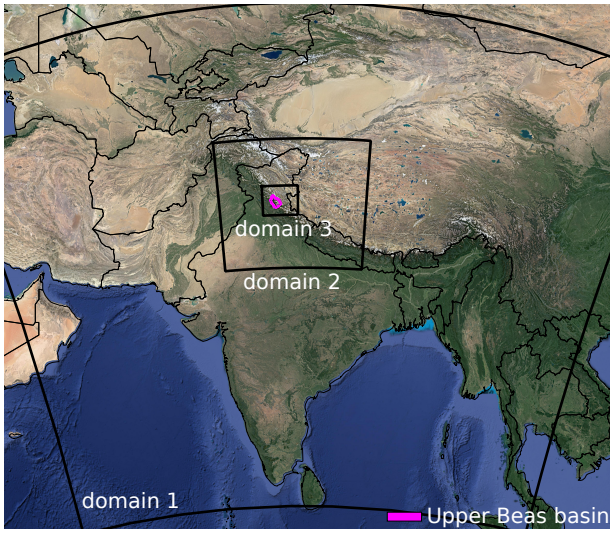

Figure 4.4: WRF domains targeting the Western Himalayas.

4.2.3 BC deposition with FLEXPART

Utilizing the Flexible Particle Dispersion Model (FLEXPART; Stohl et al., 1998, 2005; Stohl and Thomson, 1999), global atmospheric transport simulations were conducted to provide BC wet and dry deposition rates over the Hindu Kush, Karakoram, and Himalayan (HKKH) region. BC emission scenarios were developed that incorporate both contributions from long range transport as well as regional biomass burning. Emission data was retrieved from the ECLIPSE emission inventory version V4a (Klimont et al., 2017). ECLIPSE inventories are based on the GAINS (Greenhouse gas - Air pollution Interactions and Synergies) model (Amann et al., 2011), which provides emissions of long-lived greenhouse gases and shorter-lived species in a consistent framework. Open biomass burning emissions are not calculated in the GAINS model, therefore we used the GFED version 3.1 (van der Werf et al., 2010) for BC emissions from non-agricultural sources. This inventory is based on MODIS remote sensing 'hot spots' as well as other input data and provides a highly detailed record of biomass burning.

FLEXPART simulations were conducted for the period 2003 through 2013 in the forward mode using 3-hourly, operational analyses from ECMWF on a 1° x 1° resolution with 92 vertical layers. A climatology of the BC deposition was used to create a seasonal BC deposition profile used as input to the hydrological model. This provides dual benefits: first, the GFED version 3.1 emissions data is not available prior to 2003 and therefore we were able to use these profiles in a climatological context in hydrologic simulations prior to 2003. Secondly, since the wet deposition rates from FLEXPART are decoupled from the dynamically downscaled and interpolated precipitation input to the hydrological model, we followed the recommended ap-

proach from Doherty et al. (2014) to calculate a monthly mean climatology of BC mixing ratio in snow. This is, the monthly profile of wet deposited BC were converted to BC mixing ratios in falling snow using monthly precipitation sums. Dry deposition rates and mixing ratios in falling snow then constitute the input data to the hydrological model.

4.2.4 MODDRFS

The MODIS Dust Radiative Forcing in Snow (MODDRFS) algorithm presented in Painter et al. (2012a) is the first (and to date only) model that uses satellite retrieved data to estimate the additional energy absorbed by snow due to the presence of LAISI. MODDRFS bases its calculations on surface reflectance data from MODIS on board of NASA's Terra and Aqua satellites. By relating NASA's surface reflectance products Terra MODIS MOD09GA and Aqua MODIS MYD09GA[1] to modelled clean snow albedo, MODDRFS provides instantaneous radiative forcing of snow impurities at satellite overflight times. The spectral hemispherical-directional reflectance factor (Schaepman-Strub et al., 2006), which is the MOD09GA retrieval, varies with OGR and thus allows to determine this quantity. The OGR is then used to simulate clean snow albedo of snow with coherent properties using a radiative transfer model for snow. The clean snow albedo simulations require assumptions on the solar irradiance characteristics during the MODIS overpasses. MODDRFS relies on clear sky incident spectral irradiances modelled with the Santa Barbara DISORT Atmospheric Radiative Transfer (SBDART) model. The spectral reflectance difference between modelled and measured reflectance is then multiplied with terrain-corrected local spectral irradiance from SBDART. Integration of the products over the spectral bands finally gives the clear sky instantaneous at surface radiative forcing from LAISI at satellite overflight times and at per-pixel spatial resolution (~500 m; Figure 4.5).

Two variants of the MODDRFS product are available, compiled from either near-real time or historical data. The historical variant is based on a more mature version of the MOD09GA surface reflectance data with a turnaround time of about 24 hours. In this thesis, only historical data is used, which is available from February 2000 onwards.

The production of MODDRFS is focused on regions where snow cover monitoring is of interest for research activities. Continuously updated data is available for the western part of North America (including the Colorado River Basin) and the HKKH region (Figure 4.5a). Additionally, near-real time data is provided for the Andean Mountains in South America.

[1] `https://lpdaac.usgs.gov/data`

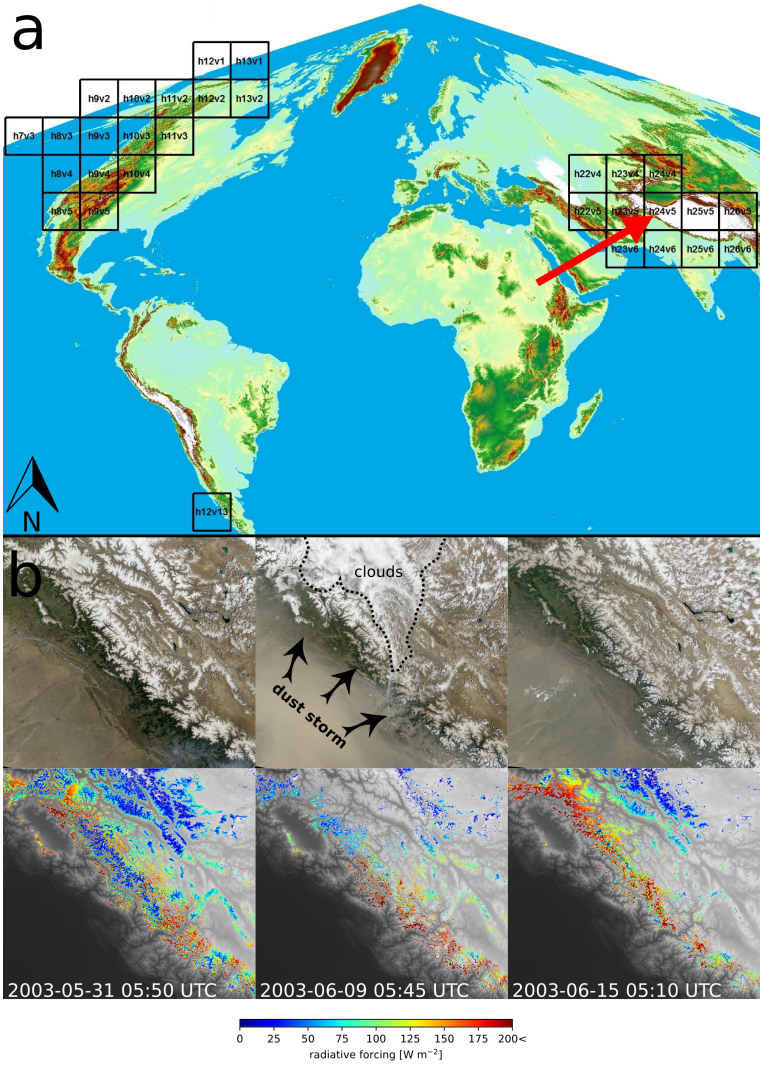

Figure 4.5: a) Tiles of the historical variant of MODDRFS. MODDRFS maintains the MODIS sinusoidal projection and the spatial resolution (500 m) of the MODIS surface reflectance products (MOD09GA). The red arrow marks the location of the image selection in b) (modified from the MODDRFS web portal (`https://snow.jpl.nasa.gov/portal/data/help_moddrfs`). b) True color MODIS images (top row) showing the western Himalayas before, during, and after a dust event in May/June 2003. The corresponding instantaneous radiative forcing in snow predicted by the MODDRFS algorithm is shown in the bottom row (modified from Figure 1 in Paper III).

5 Results

In this chapter, an overview over the main results of the thesis is given. Short summaries of the publications are provided alongside yet unpublished material related to the publications.

5.1 Summary of Paper I: Shyft - A Model Toolbox for Distributed Hydrologic Modelling in Production Environments

In this paper we present a newly developed modern and open source (`https://gitlab.com/shyft-os`) modelling platform that aims to provide distributed hydrologic modelling in research and water management environments. The model framework, namely Statkraft's Hydrologic Forecasting Toolbox (Shyft), is developed by Statkraft AS in collaboration with the University of Oslo. In the current state, the platform supports several models with focus on snow covered regions and application in environments where operational model systems are essential. Focus areas are hydropower production, flood forecasting, and water resource management in business applications and research.

The objectives of Shyft are to:

- provide a flexible hydrologic forecasting toolbox built for operational environments
- enable highly efficient/rapid calculations of hydrologic response at the region scale
- allow for using the multiple working hypothesis (e.g., Clark et al., 2011) to obtain an optimal catchment forecast
- create a mechanism for rapid implementation of improvements identified through research activities

In addition to introducing the model platform details in this paper, we provide a case study in which Shyft is used to compute predictions of natural streamflow for a production system in Norway.

Shyft provides the backbone of this thesis, and several implementations and applications were developed and explored throughout the course of this thesis, which resulted in the publications Paper II and Paper III.

5.2 Summary of Paper II: Modelling hydrologic impacts of light-absorbing aerosol deposition on snow at the catchment scale

In this publication, we present an algorithm that can be used to explore the effect of various species of light-absorbing impurities in snow and ice (LAISI) at the catchment scale. We describe and apply the implementation of an energy balance based snow accumulation/melt algorithm into a hydrologic catchment model within Shyft. The implementation enables the calculation of snow albedo implications from LAISI through a coupling to the SNICAR model (Flanner et al., 2007, 2009). LAISI mixing ratios are determined from atmospheric dry and wet deposition rates of light-absorbing aerosols. The model is able to simulate enrichment of LAISI in surface snow due to post-depositional processes. We apply the model to a region in southern Norway in order to first investigate the sensitivity of newly introduced model parameters, and then address the implications of BC deposition for snow albedo and the subsequent consequences for snowmelt and discharge generation in the region at the catchment scale.

Results from the sensitivity study show that at least two snow layers in the model (a thin surface layer and a bottom layer) is of outstanding importance to capture the potential effect of melt amplification on the LAISI evolution in surface snow. The parametrization of the surface layer thickness has only a small effect on the snow albedo and melt rate as long as it is sufficiently thin (e.g. thinner than the penetration depth of shortwave radiation). However, results also reveal that the evolution of the LAISI surface mixing ratio is highly sensitive to the surface layer thickness. Results further show that the determination of how LAISI are washed out of the snowpack with meltwater has a great effect on the evolution of LAISI concentration near the surface, as well as the snow albedo and melt rate. Due to rare observations of this effect under controlled conditions, parameters governing this effect are uncertain and so are the model predictions of LAISI impacts.

Results from simulating LAISI effects in the study region at the catchment scale show that BC in snow is likely to have a significant impact on snow albedo, particularly in spring, and that the resulting accelerated snow melt leads to a shift in the annual water balance (Figure 5.1). In-

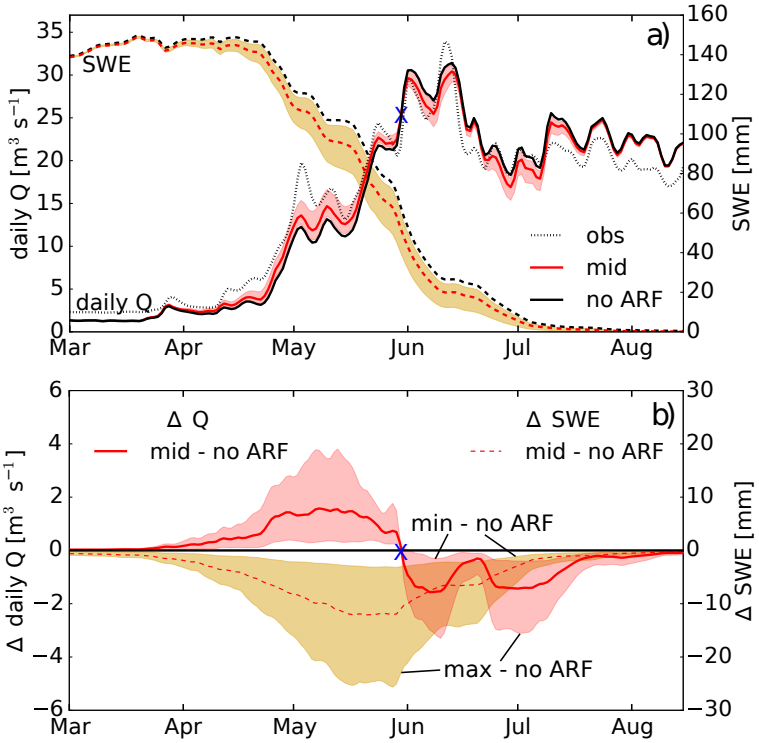

Figure 5.1: (a) Simulated daily discharge (Q; solid lines) and catchment mean SWE (dashed lines) of the Atnsjøen catchment averaged over the 6-year study period. The shaded areas show the impact range of BC (red lines mark the best estimate) for uncertainty estimates. The black lines show the scenario without radiative forcing for LAISI (no-ARF). (b) Differences in daily discharge and SWE between LAISI radiative forcing scenarios and the scenario without LAISI radiative forcing (no-ARF). The blue marker in (a) and (b) separates the periods where BC in snow has an enhancing effect (left of the marker) and a decreasing (right of the marker) effect on discharge.

cluding radiative forcing from BC in the simulations leads to a reduction in volume error during the early and late melt season in our simulations. Results show an increase in discharge of 2.5 to 21.4%, depending on the applied model scenario, over a 2-month period during the spring melt season compared to simulations, where radiative forcing from LAISI is not considered. The increase in discharge is followed by a decrease in discharge due to a faster decrease in the catchment's snow-covered fraction and a trend towards earlier melt in the scenarios where radiative forcing from LAISI is applied. Using a reasonable estimate for critical model parameters, the model simulates realistic BC mixing ratios in surface snow. The model predicts a strong annual cycle in BC mixing ratios, showing increasing surface BC mixing ratios during spring melt as a consequence of melt amplification. The simulations further identify large uncertain-

ties in the representation of the surface BC mixing ratio during snowmelt and the subsequent consequences for the snowpack evolution.

5.3 Summary of Paper III: Assessing satellite derived radiative forcing from snow impurities through inverse hydrologic modelling

In this publication, we present a methodology for comparing LAISI radiative forcing from models with remotely sensed data. We furthermore employ the potential of this method by investigating the impact of LAISI on the discharge generation in the Upper Beas Basin in Himachal Pradesh, India.

The satellite dataset used in our study is based on the MODDRFS algorithm (Painter et al., 2012a). Simulated radiative forcing, on the other hand, is estimated using the snow algorithm described in Paper II implemented in the Shyft model framework (Paper I).

Due to the instantaneous nature of MODDRFS data and the assumption of clear sky solar radiative conditions in the MODDRFS algorithm, we claim that the simulated radiative forcing must be based on coherent atmospheric radiative conditions in order to be comparable to the satellite product. With regards to our model approach, we therefore use the same radiative transfer model for the atmosphere that is used in MODDRFS to determine clear sky solar irradiances, and estimate simulated radiative forcing at MODIS overpass times. The latter is determined from stand-alone simulations with the SNICAR model used to determine snow albedo of clean and impurity bearing snow at MODIS overpass radiative conditions. Snowpack variables required as input to SNICAR (LAISI content of snow, OGR, SWE) are estimated using an inverse hydrologic modelling approach. That is, we estimate model parameters of the hydrologic model by optimizing regional simulated streamflow constrained by observed streamflow. The optimized hydrologic model is then used to simulate the snowpack variables. Deposition rates of BC and dust are considered in the simulation chain. Deposition rates of BC are modelled over the study region using the FLEXPART model. Dust, presumably the most important absorber in the study area, is incorporated in the model simulations using a simple deposition scenario based on quantitative estimates from Himalayan glaciers. Due to the predominant dust deposition during premonsoon season, we add dust to the surface layer on a daily basis during March to June, so that the daily added amount is constant and the annual sum initially has a magnitude consistent with observed annual depositions. However, results show that aiming for

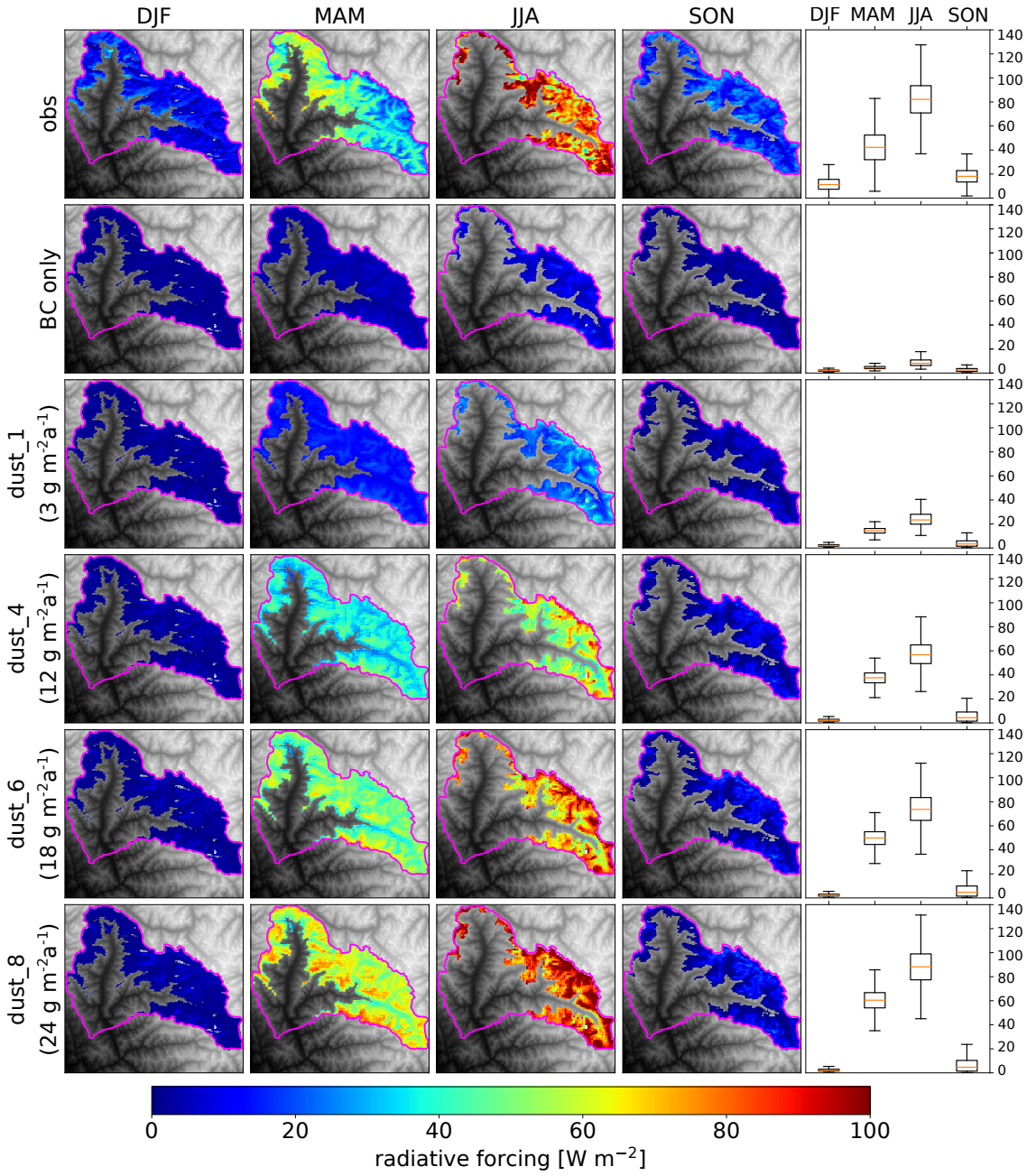

Figure 5.2: Seasonal mean per-pixel instantaneous radiative forcing from MODDRFS observations (row 1) and model simulations using different LAP deposition scenarios (rows 2 to 6). DJF = December,January, February; MAM = March, April, May; JJA = June, July, August; SON = September, October, November.

3 g $m^{-2}a^{-1}$ (dust_1 scenario) observed closest to the study region, produces a strong underestimation of simulated radiative forcing (see top row of Figure 5.2). We therefore scale dust depositions to multiples of this initial deposition scenario, re-estimate model parameters and re-calculate the radiative forcing at MODIS overpass times, in order to achieve an optimization of the simulated radiative forcing of LAISI towards the MODDRFS product (Figure 5.2).

The upward scaling of dust leads to a better representation of the seasonal cycle of radiative forcing from LAISI shown in the observations (row 1 of graphs in Figure 5.2). However, simulated radiative forcing is underestimated during winter months (December, January, February) regardless of the applied dust scenario. According to the root-mean-square error E_{RMS} of basin mean monthly radiative forcing, an annual dust deposition of 18 g $m^{-2}a^{-1}$ (dust_6 scenario) gives the best results.

The optimized radiative forcing simulation allows to estimate the LAISI impact on hydrologic variables (Figure 5.3). On average, LAISI lead to significantly higher discharge from about middle March to end of August. For the rest of the year, no significant difference in discharge is noticeable. The optimized model predicts LAISI-induced radiative forcing in snow contributes to 3.52 to 5.41% of the annual discharge.

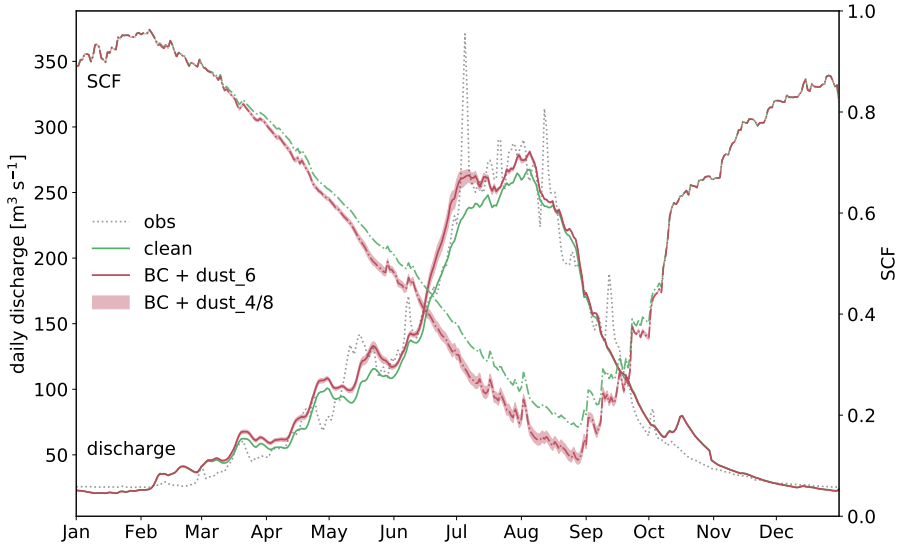

Figure 5.3: Daily discharge and snow-covered fraction averaged over the 6-year study period for the dust_6 scenario (red curve; 18 g $m^{-2}a^{-1}$ dust deposition) and the scenario ignoring radiative forcing by LAISI ("clean"; green curve). The red shaded area shows the difference between the dust_4 (12 g $m^{-2}a^{-1}$) and dust_8 (24 g $m^{-2}a^{-1}$) scenarios used to estimate impact uncertainty.

6 General Discussion

6.1 LAISI impact on hydrology

The model results show significant impact on the hydrology for both study regions, the basin located in southern Norway and the one located in the Indian Himalayas. However, comparing the discharge response to LAISI radiative forcing from both sites reveals large differences in the response patterns. In the Norwegian catchment, a shift in the water balance is observed, manifested in increase in discharge early in the melt season and decrease in the late spring season (Figure 5.1). On an annual scale, increase and decrease cancel each other out, so that the total annual discharge is nearly unaffected. In the Himalayan basin, on the other hand, LAISI lead to an overall increase in discharge, with strongest surplus during spring/summer (Figure 5.3). The reason for the different response patterns can be explained by different availability of snow and ice in the two regions. The Rondane mountains in Norway are a relatively dry area. Despite the cold temperatures and high elevation of the region, the relatively small winter precipitation is preventing the accumulation of snowpacks that are able to survive the spring and summer. Glaciers are not to be found in the area and snow and ice storage only exists during winter and spring. Accelerated melt early in the spring season due to radiative forcing from LAISI and the subsequent increase in discharge must therefore necessarily be balanced by a decrease in discharge later in the season. In Paper II we refer to this as *melt limitation*, meaning that snow melt stops earlier or is less strong during the late melt season.

The Upper Beas basin above Bhuntar station, on the other hand, is characterized by permanent snow and ice cover above an elevation of 4800 masl, and about 13% of the catchment is glaciated. The high fraction of glaciation and permanent snow cover leads to the phenomenon that the accelerated snow melt in spring due to LAISI is not necessarily balanced by a retreat in discharge later in the season but rather leads to a faster ageing of snow and thus darker albedo during summer and earlier exposure of glaciated areas. Consequently, discharge is higher during late spring and summer compared to a scenario where the effect of LAISI on albedo is disregarded in the albedo model. In fact, in our study region discharge does not drop below the discharge of a clean snow scenario when using reasonable assumptions for LAP deposition.

The shift in water balance as found in the Norwegian basin is similar to previous findings from the Colorado mountain range, where mineral dust is the dominating absorber (Painter et al., 2010), and the TP, where BC is the dominating absorber in snow (Qian et al., 2011). These studies observed a shift in the annual water balance with increasing discharge during spring melt season and decrease of discharge later in the season. The increase in discharge throughout the year, however, is firstly observed in our study.

Water resource managers and policy makers are increasingly aware of the impacts LAISI can have on snow and ice covered regions (IPCC, 2013). Our study reveals that for decision making and strategic planning of emission regulations, the predominant snow regime of an area (i.e. the portion of permanent snow cover) determines if changed boundary conditions of aerosol deposition lead to a shift in the water balance, or potentially increase/decrease the annual discharge sum. This distinction is of great importance with respect to water resource management, policy making, and future climate impact estimates.

6.2 The potential of LAISI remote sensing products

6.2.1 Improving impact estimates by using LAISI remote sensing products

Model results reveal that LAISI can significantly impact snow albedo. A challenge is hereby the evaluation of model predictions of LAISI impacts against observable parameters. So far, a model's ability to predict LAISI has been assessed by comparing observed LAISI concentrations with those predicted by the respective model (e.g., Flanner et al., 2007; Forsström et al., 2013; Ménégoz et al., 2014). A good representation of LAISI concentrations in surface snow has been considered a well suited measure of the model's ability to capture LAISI processes. Based on such comparisons, LAISI impacts on glacier mass balance (Kaspari et al., 2011; Zhang et al., 2017), regional hydrology (Qian et al., 2014b), and climate (Jacobson, 2004; Flanner et al., 2007) have been concluded. However, there are a number of disadvantages connected to this approach. Firstly, the approach only evaluates the cause, i.e. the concentrations, but not the subsequent effect, i.e. the radiative forcing. If one aims to estimate LAISI impacts, this is problematic. Because the radiative forcing depends on several other variables, such as the OGR of the snow and incoming solar radiation characteristics, reliably predicted LAISI concentrations are *necessary*, but not necessarily *sufficient* to reliably predict LAISI radiative forcing and impacts. Also, our sensitivity study from Paper II shows large uncertainty in the modelled con-

centrations resulting from the way surface snow is represented in the model, which makes the comparisons between model predictions and observations more challenging.

Furthermore, data collection is extremely time consuming and expensive as sampling of snow is required. The snow is then melted, filtered and further analysed to determine LAISI concentrations. In addition, the available analysis methods introduce large uncertainties to the estimated LAISI concentrations (e.g. BC concentrations can vary by up to a factor of seven depending on the approach used (Petzold et al., 2013)). Due to the requirement of manual snow sampling, measurements are often incomplete in space and time, and limited to accessible regions. LAISI, however, can show large variability on spatial and temporal scales (AMAP, 2015), which requires spatially and temporally consistent measurements.

In particular to capture the annual cycle in seasonal snow, which is mainly caused by vertical redistribution of LAISI within the snowpack during snow melt (see Paper II, III, and Aoki et al., 2011; Doherty et al., 2013; Forsström et al., 2013), requires dense observational coverage in space and time. Due to relatively sparse measurements, some regional (Qian et al., 2009) and global (Jacobson, 2004; Flanner et al., 2007) studies evaluate model predictions using data where observed and modelled years are different, making a discussion beyond potential climatological variations impossible. In particular, the temporal mismatch causes difficulty in the validation because LAISI concentrations can show large seasonal fluctuations at a given location. Furthermore, Ménégoz et al. (2014) pointed out that for high-elevation regions like the Himalayas, there are numerous difficulties when carrying out comparisons of LAISI due to the amount of possible uncertainties.

Some of the discussed issues related to the use of observed LAISI concentration for model evaluation are resolved by using satellite products that estimate LAISI radiative forcing (Painter et al., 2012a). Advantageous are in particular the

1. dense temporal coverage
2. wide spatial coverage
3. low cost data availability

once a satellite suitable for the analysis is in operation. Points 1. and 2. will improve as satellites are improving.

To date, radiative forcing estimates from satellites are limited in that they only provide instantaneous values and are based on critical assumptions about the radiative properties of the atmosphere. Derivation of the total energy absorbed due to the presence of absorbers in the snow (e.g. daily or monthly means) are not possible so far, but might become reality as the temporal resolution of suitable satellites approaches into the sub-daily range (Painter et al., 2012a).

Due to these limitations, the satellite data available up to this point is not directly comparable to model results. In Paper III, we therefore developed a methodology that allows comparison between the instantaneous clear sky radiative forcing retrieved with MODDRFS and model predictions despite these challenges.

The approach enables an additional option for evaluating and improving radiative forcing by LAISI predicted by models. The additional data source represents a valuable contribution in addition to the established snow sampling methods that can be integrated when simulating LAISI effects on glacier mass balance, regional hydrology, and climate. The integration of the satellite product then allows to investigate a model's ability to simulate the spatial and temporal variations of radiative forcing by LAISI at different scales, and, if necessary, reconsider and update the model configuration in order to improve the prediction. This has been done in the case study of Paper III, allowing an improved impact estimate of LAISI on the hydrologic response of a Himalayan catchment, as well as giving an estimate on the annual dust deposition flux of the region, which is known to be highly uncertain.

Targeting the effect of LAISI on climate and hydrology on different scales is important. The possibility to reduce uncertainties in the responses to LAISI allows for more reliable predictions to be utilized by scientists, policy makers, and water resource managers.

6.2.2 Estimating LAISI surface concentrations via satellites - a challenge or impossible?

Retrieving the concentrations of LAISI using satellites could reveal trends in the deposition of LAP on regional to global scales, and help identifying whether policy decisions on LAP emissions, e.g. BC, are showing the desired results. For this reason, the question arises whether the LAISI concentrations could be detected from radiance measurements by satellite.

An answer to this question is presented by Warren (2013), focusing on BC only, claiming that estimating BC content in snow using satellite remote sensing is unlikely to be successful due to several reasons: errors in satellite retrieved albedo on the magnitude of order of the albedo decrease from BC in snow, impacts from undetected thin clouds and blowing snow, implications from bare ground areas at the sub-pixel scale.

Seemingly opposing Warren's concerns, Painter et al. (2012a) presented the MODDRFS algorithm to detect radiative forcing from LAISI from MODIS surface reflectance data showing that the algorithm gives relatively good results for the Colorado mountain range, and a plausible range of values for the HKKH. However, MODDRFS does not address the direct retrieval of LAISI content, which would add another level of complexity, as a certain reduction in albedo

does not stand in unambiguous relation to LAISI content: a theoretically infinite amount of combinations of LAISI species compositions, optical grain sizes, and vertical profiles of LAISI concentrations lead to similar reductions in albedo (Warren and Wiscombe, 1980; Warren, 2013). For this reason, an unambiguous detection of LAISI concentrations is not possible without further information.

Even though our study does not directly address the satellite retrieval of LAISI content, we are arguing that our approach, which combines modelling (Paper II) with a model-satellite data analysis chain (Paper III), could pave the way for a satellite supported product predicting LAISI content in snow.

The approach introduced in Paper III is the first allowing the comparison of clear sky radiative forcing from LAISI observed by a satellite and predicted by a model. By using coherent atmospheric radiative conditions for the model prediction, we minimize impacts from differences in atmospheric radiation used in the model and satellite product. Based on this, we argue that differences in the radiative forcing outside the bounds of uncertainty of the satellite product are mainly due to shortcomings in modelling LAISI in surface snow. Thus, by adapting and improving the aerosol deposition scenarios, an optimization towards the satellite product can be achieved.

In Paper III, we adapted LAP depositions in order to get an improved estimate on the hydrologic impact of LAISI. Generalizing the approach and shifting the focus on LAISI representation in surface snow, the model/satellite coupled approach opens the possibility to estimate LAISI concentrations in snow. In this context, the model part of the approach can help to overcome the problem of equifinality stressed by Warren (2013). That is, due to inclusion of post-depositional processes in the snow model, the processes determining the vertical profile of snowpack variables are represented in a physically coherent way. Uncertainties in estimated snow variables can be reduced by improving the snowpack scheme and input data used for the model. Differences in radiative forcing between satellite observations and models can then be minimized by e.g. improving certain aspects of the atmospheric transport schemes or scaling deposition rates, as done in the case study of Paper III.

The proposed approach is primarily suitable for regions where a single LAISI species dominates radiative impacts and which are exposed to high levels of contamination. Despite these limitations, further developing the approach described in Paper III has the potential to fill the gap of a temporally and spatially continuous product of LAISI content in surface snow.

6.3 Improvement of hydrologic modelling and uncertainty

By implementing the effects of LAISI in the snow routine of the hydrological model, we are adding complexity to the model. As indicated by e.g. Orth et al. (2015), adding complexity to hydrologic models operating at the catchment scale does not necessarily lead to improved performance and, in general, the quality of input data is more important than model complexity (Finger et al., 2015).

Due to the physical meaning of processes included in the model we in fact reduced the parameter space by two parameters that require estimation through model calibration compared to the *Gamma Snow* algorithm of Shyft, which is based on similar energy balance calculations. The parameters removed define the albedo decay function. On the other hand, new parameters have been introduced to the model. These parameters (melt scavenging ratios k_i) are based on observable parameters and do not require calibration. Reducing the parameter space of the hydrologic models is advantageous as it reduces the risk of equifinality (Beven, 2006), and provides more robust predictions for future climatic conditions as catchment characteristics change with altered boundary conditions.

Accounting for post-depositional processes in models is important in order to capture the seasonal cycle in surface LAISI content and radiative forcing, and the consequences for hydrologic variables (Paper II and III) as well as climate forcing on a regional and global scale (e.g. Flanner et al., 2007; Qian et al., 2011; Oaida et al., 2015).

However, as field observations are rare, the parameters governing scavenging processes are, to date, connected with large uncertainties. Though many studies have reported increasing accumulation of absorbers at the snow surface during melt (Higuchi and Nagoshi, 1977; Conway et al., 1996; Doherty et al., 2013; Aamaas et al., 2011; Sterle et al., 2013), hardly any allow for quantification of scavenging parameters. In fact, most models that allow for post-depositional LAISI processes base the parametrization of LAISI scavenging on only few experimental investigations. Primarily the results from Conway et al. (1996) are used to quantify the scavenging parameters even though the model experiments conducted in this study were not designed with the aim to estimate these parameters. Due to the limited experimental bases, the uncertainty on the parameter estimates is large (Flanner et al., 2007). Despite these issues, a number of studies use these estimates to investigate LAISI impacts on different spatial scales (Flanner et al., 2007, 2009; Qian et al., 2011; Oaida et al., 2015), including the herein presented work. As a direct consequence form the large uncertainties of LAISI scavenging, the impact estimates of LAISI in surface snow and the hydrologic response are connected with considerable uncertainties, as revealed in Paper II of this thesis. Due to the importance of the effect of LAISI on snow-melt

processes and climate forcing, we therefore strongly argue for further experimental work regarding the fate of different LAISI species during post-depositional processes in order to better understand these processes and reduce uncertainties in modelling.

7 Conclusions

The main goal of this thesis was to further the knowledge about the role of LAISI on hydrologic processes in snow dominated regions through hydrologic catchment modelling. The main outcome of this thesis is a novel snow routine applied within a novel distributed hydrologic model framework and an improved understanding about the sensitivity, uncertainty, and magnitude of impacts of different LAISI species on discharge generation in two drastically different regions.

The main objective listed in the introduction have been addressed as follows:

- **Objective 1:** *Develop a snow algorithm able to take effects from light absorbing aerosols into account.*

  In this thesis, a novel snow algorithm has been developed that is able to account for LAISI implications on snow (Paper I). The snow algorithm conducts energy balance calculation to determine snow melt, where snow albedo is calculated from a coupling to a radiative transfer model for snow. The albedo model accounts for LAISI in two snow layers, originating from wet and dry deposition of LAP. The model further allows for melt water transport of LAISI between the layers and out of the snowpack.

  Even though the effect of LAISI has been implemented in a number of models operating at different scales, the herein presented contribution provides the first snow algorithm accounting for LAISI within a hydrologic catchment model.

- **Objective 2:** *Investigate the sensitivity and uncertainty of processes related to light absorbing impurities.*

  The new model has been applied in catchments in Norway (Paper I) and the Indian Himalayas (Paper II). The studies reveal the significance of LAISI forcing for snow melt and discharge generation and highlight potential improvements of hydrologic forecasting by including these effects, in particular in regions with high deposition rates of LAP, and in regions that are under the impact of event based deposition scenarios. However, the studies also demonstrate large uncertainties in the effect of LAISI on discharge generation. Uncertainties originate in particular from uncertainties in melt amplification. As

parametrizations available to date are based only on limited empirical data, more field data is required in order to improve process understanding and reduce uncertainties.

- **Objective 3:** *Integrate remotely sensed snowpack information in order to improve model predictions of light absorbing impurity impacts on the hydrologic response.*

  In this thesis, a first-of-its-kind approach to integrate remotely sensed radiative forcing from LAISI is presented. The approach has a wide field of application as it enables a new method to test and evaluate model predictions of LAISI radiative forcing on a large number of scales. This will reduce uncertainty of future LAISI predictions, as traditional methods to evaluate model predictions rely on costly fieldwork and are limited in time and space. As satellites will improve in temporal and spatial resolution, the significance of the herein presented approach will further increase. By applying the method in a region located in the Indian Himalayas, an improvement of the estimates of LAP deposition and LAISI impacts on hydrologic processes could be achieved.

References

Aamaas, B., Bøggild, C. E., Stordal, F., Berntsen, T., Holmen, K., and Ström, J.: Elemental carbon deposition to Svalbard snow from Norwegian settlements and long-range transport, Tellus B, 63, 340–351, doi:10.1111/j.1600-0889.2011.00531.x, 2011.

Aas, K. S., Gisnås, K., Westermann, S., and Berntsen, T. K.: A Tiling Approach to Represent Subgrid Snow Variability in Coupled Land Surface-Atmosphere Models, Journal of Hydrometeorology, 18, 49–63, doi:10.1175/JHM-D-16-0026.1, 2017.

Albrecht, B. A.: Aerosols, Cloud Microphysics, and Fractional Cloudiness, Science, 245, 1227–1230, doi:10.1126/science.245.4923.1227, 1989.

Amann, M., Bertok, I., Borken-Kleefeld, J., Cofala, J., Heyes, C., Höglund-Isaksson, L., Klimont, Z., Nguyen, B., Posch, M., Rafaj, P., Sandler, R., Schöpp, W., Wagner, F., and Winiwarter, W.: Cost-effective control of air quality and greenhouse gases in Europe: Modeling and policy applications, Environmental Modelling & Software, 26, 1489–1501, doi:10.1016/j.envsoft.2011.07.012, 2011.

AMAP, .: AMAP Assessment 2015: Black carbon and ozone as Arctic climate forcers, Arctic Monitoring and Assessment Programme (AMAP), 2015.

Anderson, E. A.: A Point Energy and Mass Balance Model of a Snow Cover, NOAA Technical Report NWS, 19, 1976.

Aoki, T., Aoki, T., Fukabori, M., Hachikubo, A., Tachibana, Y., and Nishio, F.: Effects of snow physical parameters on spectral albedo and bidirectional reflectance of snow surface, Journal of Geophysical Research: Atmospheres, 105, 10 219, doi:10.1029/1999JD901122, 2000.

Aoki, T., Kuchiki, K., Niwano, M., Kodama, Y., Hosaka, M., and Tanaka, T.: Physically based snow albedo model for calculating broadband albedos and the solar heating profile in snowpack for general circulation models, Journal of Geophysical Research: Atmospheres, 116, D11 114, doi:10.1029/2010JD015507, 2011.

Barnett, T. P., Adam, J. C., and Lettenmaier, D. P.: Potential impacts of a warming climate on water availability in snow-dominated regions, Nature, 438, 303–309, doi:10.1038/nature04141, 2005.

Bennett, N. D., Croke, B. F., Guariso, G., Guillaume, J. H., Hamilton, S. H., Jakeman, A. J., Marsili-Libelli, S., Newham, L. T., Norton, J. P., Perrin, C., Pierce, S. A., Robson, B., Seppelt, R., Voinov, A. A., Fath, B. D., and Andreassian, V.: Characterising performance of environmental models, Environmental Modelling & Software, 40, 1–20, doi:10.1016/j.envsoft.2012.09.011, 2013.

Berghuijs, W. R., Woods, R. A., Hutton, C. J., and Sivapalan, M.: Dominant flood generating mechanisms across the United States, Geophysical Research Letters, 43, 4382–4390, doi: 10.1002/2016GL068070, 2016.

Bergström, S.: Development and application of a conceptual runoff model for Scandinavian catchments, SMHI, Report RH07, Norrköping, Sweden, 1976.

Bergström, S.: The HBV model, pp. 443–476, Water Resources Publications, Highlands Ranch, CO., 1995.

Beven, K.: A manifesto for the equifinality thesis, Journal of Hydrology, 320, 18–36, doi: 10.1016/j.jhydrol.2005.07.007, 2006.

Bond, T. C. and Bergstrom, R. W.: Light Absorption by Carbonaceous Particles: An Investigative Review, Aerosol Science and Technology, 40, 27–67, doi:10.1080/02786820500421521, 2006.

Bond, T. C., Habib, G., and Bergstrom, R. W.: Limitations in the enhancement of visible light absorption due to mixing state, Journal of Geophysical Research, 111, D20 211, doi:10.1029/2006JD007315, 2006.

Bond, T. C., Doherty, S. J., Fahey, D. W., Forster, P. M., Berntsen, T., DeAngelo, B. J., Flanner, M. G., Ghan, S., Kärcher, B., Koch, D., Kinne, S., Kondo, Y., Quinn, P. K., Sarofim, M. C., Schultz, M. G., Schulz, M., Venkataraman, C., Zhang, H., Zhang, S., Bellouin, N., Guttikunda, S. K., Hopke, P. K., Jacobson, M. Z., Kaiser, J. W., Klimont, Z., Lohmann, U., Schwarz, J. P., Shindell, D., Storelvmo, T., Warren, S. G., and Zender, C. S.: Bounding the role of black carbon in the climate system: A scientific assessment, Journal of Geophysical Research: Atmospheres, 118, 5380–5552, doi:10.1002/jgrd.50171, 2013.

Bookhagen, B. and Burbank, D. W.: Toward a complete Himalayan hydrological budget: Spatiotemporal distribution of snowmelt and rainfall and their impact on river discharge, Journal of Geophysical Research: Earth Surface, 115, F03 019, doi:10.1029/2009JF001426, 2010.

Brock, B. W., Willis, I. C., and Sharp, M. J.: Measurement and parameterization of albedo variations at Haut Glacier d'Arolla, Switzerland, Journal of Glaciology, 46, 675–688, doi: 10.3189/172756500781832675, 2000.

Brun, E.: Investigation on wet-snow metamorphims in respect of liquid water content, Annals of Glaciology, 13, 22–26, doi:10.3189/S0260305500007576, 1989.

Brun, E., David, P., Sudul, M., and Brunot, G.: A numerical model to simulate snow-cover stratigraphy for operational avalanche forecasting, Journal of Glaciology, 38, 13–22, doi: 10.3189/S0022143000009552, 1992.

Bryant, A. C., Painter, T. H., Deems, J. S., and Bender, S. M.: Impact of dust radiative forcing in snow on accuracy of operational runoff prediction in the Upper Colorado River Basin, Geophysical Research Letters, 40, 3945–3949, doi:10.1002/grl.50773, 2013.

Clark, M. P., Kavetski, D., and Fenicia, F.: Pursuing the method of multiple working hypotheses for hydrological modeling, Water Resources Research, 47, 1–16, doi:10.1029/2010WR009827, 2011.

Clarke, A. D. and Noone, K. J.: Soot in the arctic snowpack a cause for perturbations in radiative transfer, Atmospheric Environment, 19, 2045–2053, 1985.

Collier, E., Mölg, T., Maussion, F., Scherer, D., Mayer, C., and Bush, A. B. G.: High-resolution interactive modelling of the mountain glacier-atmosphere interface: an application over the Karakoram, The Cryosphere, 7, 779–795, doi:10.5194/tc-7-779-2013, 2013.

Conway, H., Gades, A., and Raymond, C. F.: Albedo of dirty snow during conditions of melt, Water Resources Research, 32, 1713–1718, doi:10.1029/96WR00712, 1996.

Cooper, V. A., Nguyen, V. T. V., and Nicell, J. A.: Evaluation of global optimization methods for conceptual rainfall-runoff model calibration, Water Science and Technology, 36, 53–60, doi:10.1016/S0273-1223(97)00461-7, 1997.

Cosgrove, W. J. and Loucks, D. P.: Water management: Current and future challenges and research directions, Water Resources Research, 51, 4823–4839, doi:10.1002/2014WR016869, 2015.

Cossu, F. and Hocke, K.: Influence of microphysical schemes on atmospheric water in the Weather Research and Forecasting model, Geoscientific Model Development, 7, 147–160, doi:10.5194/gmd-7-147-2014, 2014.

Coulson, K. L., Bouricius, G. M., and Gray, E. L.: Optical reflection properties of natural surfaces, Journal of Geophysical Research, 70, 4601–4611, doi:10.1029/JZ070i018p04601, 1965.

Dang, C., Fu, Q., and Warren, S. G.: Effect of Snow Grain Shape on Snow Albedo, Journal of the Atmospheric Sciences, 73, 3573–3583, doi:10.1175/JAS-D-15-0276.1, 2016.

Dee, D. P., Uppala, S. M., Simmons, A. J., Berrisford, P., Poli, P., Kobayashi, S., Andrae, U., Balmaseda, M. A., Balsamo, G., Bauer, P., Bechtold, P., Beljaars, A. C. M., van de Berg, L., Bidlot, J., Bormann, N., Delsol, C., Dragani, R., Fuentes, M., Geer, A. J., Haimberger, L., Healy, S. B., Hersbach, H., Hólm, E. V., Isaksen, L., Kållberg, P., Köhler, M., Matricardi, M., McNally, A. P., Monge-Sanz, B. M., Morcrette, J.-J., Park, B.-K., Peubey, C., de Rosnay, P., Tavolato, C., Thépaut, J.-N., and Vitart, F.: The ERA-Interim reanalysis: configuration and performance of the data assimilation system, Quarterly Journal of the Royal Meteorological Society, 137, 553–597, doi:10.1002/qj.828, 2011.

Dentener, F., Kinne, S., Bond, T., Boucher, O., Cofala, J., Generoso, S., Ginoux, P., Gong, S., Hoelzemann, J. J., Ito, A., Marelli, L., Penner, J. E., Putaud, J.-P., Textor, C., Schulz, M., van der Werf, G. R., and Wilson, J.: Emissions of primary aerosol and precursor gases in the years 2000 and 1750 prescribed data-sets for AeroCom, Atmospheric Chemistry and Physics, 6, 4321–4344, doi:10.5194/acp-6-4321-2006, 2006.

Di Mauro, B., Fava, F., Ferrero, L., Garzonio, R., Baccolo, G., Delmonte, B., and Colombo, R.: Mineral dust impact on snow radiative properties in the European Alps combining ground, UAV, and satellite observations, Journal of Geophysical Research: Atmospheres, 120, 6080–6097, doi:10.1002/2015JD023287, 2015.

Doherty, S. J., Warren, S. G., Grenfell, T. C., Clarke, A. D., and Brandt, R. E.: Light-absorbing impurities in Arctic snow, Atmospheric Chemistry and Physics, 10, 11 647–11 680, doi:10.5194/acp-10-11647-2010, 2010.

Doherty, S. J., Grenfell, T. C., Forsström, S., Hegg, D. L., Brandt, R. E., and Warren, S. G.: Observed vertical redistribution of black carbon and other insoluble light-absorbing particles in melting snow, Journal of Geophysical Research: Atmospheres, 118, 5553–5569, doi:10.1002/jgrd.50235, 2013.

Doherty, S. J., Bitz, C. M., and Flanner, M. G.: Biases in modeled surface snow BC mixing ratios in prescribed-aerosol climate model runs, Atmospheric Chemistry and Physics, 14, 11 697–11 709, doi:10.5194/acp-14-11697-2014, 2014.

Domine, F., Taillandier, A.-S., and Simpson, W. R.: A parameterization of the specific surface area of seasonal snow for field use and for models of snowpack evolution, Journal of Geophysical Research: Earth Surface, 112, F02 031, doi:10.1029/2006JF000512, 2007.

Duan, Q., Sorooshian, S., and Gupta, V. K.: Effective and efficient global optimization for conceptual rainfall-runoff models, Water Resources Research, 28, 1015–1031, doi:10.1029/91WR02985, 1992.

Duan, Q., Sorooshian, S., and Gupta, V. K.: Optimal use of the SCE-UA global optimization method for calibrating watershed models, Journal of Hydrology, 158, 265–284, doi:10.1016/0022-1694(94)90057-4, 1994.

Duchi, R., Cristofanelli, P., Marinoni, A., Bourcier, L., Laj, P., Calzolari, F., Adhikary, B., Verza, G. P., Vuillermoz, E., and Bonasoni, P.: Synoptic-scale dust transport events in the southern Himalaya, Aeolian Research, 13, 51–57, doi:10.1016/j.aeolia.2014.03.008, 2014.

Dusek, U., Reischl, G. P., and Hitzenberger, R.: CCN Activation of Pure and Coated Carbon Black Particles, Environmental Science & Technology, 40, 1223–1230, doi:10.1021/es0503478, 2006.

Engelhardt, M., Schuler, T. V., and Andreassen, L. M.: Contribution of snow and glacier melt to discharge for highly glacierised catchments in Norway, Hydrology and Earth System Sciences, 18, 511–523, doi:10.5194/hess-18-511-2014, 2014.

Finger, D., Vis, M., Huss, M., and Seibert, J.: The value of multiple data set calibration versus model complexity for improving the performance of hydrological models in mountain catchments, Water Resources Research, 51, 1939–1958, doi:10.1002/2014WR015712, 2015.

Flanner, M. G. and Zender, C. S.: Linking snowpack microphysics and albedo evolution, Journal of Geophysical Research: Atmospheres, 111, D12 208, doi:10.1029/2005JD006834, 2006.

Flanner, M. G., Zender, C. S., Randerson, J. T., and Rasch, P. J.: Present-day climate forcing and response from black carbon in snow, Journal of Geophysical Research: Atmospheres, 112, D11 202, doi:10.1029/2006JD008003, 2007.

Flanner, M. G., Zender, C. S., Hess, P. G., Mahowald, N. M., Painter, T. H., Ramanathan, V., and Rasch, P. J.: Springtime warming and reduced snow cover from carbonaceous particles, Atmospheric Chemistry and Physics, 9, 2481–2497, doi:10.1029/2005JD006356, 2009.

Forsström, S., Isaksson, E., Skeie, R. B., Ström, J., Pedersen, C. A., Hudson, S. R., Berntsen, T. K., Lihavainen, H., Godtliebsen, F., and Gerland, S.: Elemental carbon measurements in European Arctic snow packs, Journal of Geophysical Research: Atmospheres, 118, 13,614–13,627, doi:10.1002/2013JD019886, 2013.

Gabbi, J., Huss, M., Bauder, A., Cao, F., and Schwikowski, M.: The impact of Saharan dust and black carbon on albedo and long-term mass balance of an Alpine glacier, The Cryosphere, 9, 1385–1400, doi:10.5194/tc-9-1385-2015, 2015.

Gardner, A. S. and Sharp, M. J.: A review of snow and ice albedo and the development of a new physically based broadband albedo parameterization, Journal of Geophysical Research, 115, F01 009, doi:10.1029/2009JF001444, 2010.

Gautam, R., Hsu, N. C., Tsay, S. C., Lau, K. M., Holben, B., Bell, S., Smirnov, A., Li, C., Hansell, R., Ji, Q., Payra, S., Aryal, D., Kayastha, R., and Kim, K. M.: Accumulation of aerosols over the Indo-Gangetic plains and southern slopes of the Himalayas: distribution, properties and radiative effects during the 2009 pre-monsoon season, Atmospheric Chemistry and Physics, 11, 12 841–12 863, doi:10.5194/acp-11-12841-2011, 2011.

Gautam, R., Hsu, N. C., Lau, W. K.-M., and Yasunari, T. J.: Satellite observations of desert dust-induced Himalayan snow darkening, Geophysical Research Letters, 40, 988–993, doi:10.1002/grl.50226, 2013.

Gisnås, K., Westermann, S., Schuler, T. V., Melvold, K., and Etzelmüller, B.: Small-scale variation of snow in a regional permafrost model, The Cryosphere, 10, 1201–1215, doi:10.5194/tc-10-1201-2016, 2016.

Grenfell, T. C., Perovich, D. K., and Ogren, J. A.: Spectral albedos of an alpine snowpack, Cold Regions Science and Technology, 4, 121–127, doi:10.1016/0165-232X(81)90016-1, 1981.

Gueymard, C. A.: Parameterized transmittance model for direct beam and circumsolar spectral irradiance, Solar Energy, 71, 325–346, doi:10.1016/S0038-092X(01)00054-8, 2001.

Gueymard, C. A., Myers, D., and Emery, K.: Proposed reference irradiance spectra for solar energy systems testing, Solar Energy, 73, 443–467, doi:10.1016/S0038-092X(03)00005-7, 2002.

Hadley, O. L. and Kirchstetter, T. W.: Black-carbon reduction of snow albedo, Nature Climate Change, 2, 437–440, doi:10.1038/NCLIMATE1433, 2012.

Hansen, J. and Nazarenko, L.: Soot climate forcing via snow and ice albedos, Proceedings of the National Academy of Sciences, 101, 423–428, doi:10.1073/pnas.2237157100, 2004.

Hansen, J., Sato, M., and Ruedy, R.: Radiative forcing and climate response, Journal of Geophysical Research: Atmospheres, 102, 6831–6864, doi:10.1029/96JD03436, 1997.

Hansen, J., Sato, M., Ruedy, R., Nazarenko, L., Lacis, A., Schmidt, G. A., Russell, G., Aleinov, I., Bauer, M., Bauer, S., Bell, N., Cairns, B., Canuto, V., Chandler, M., Cheng, Y., Del Genio, A., Faluvegi, G., Fleming, E., Friend, A., Hall, T., Jackman, C., Kelley, M., Kiang, N., Koch, D., Lean, J., Lerner, J., Lo, K., Menon, S., Miller, R., Minnis, P., Novakov, T., Oinas, V., Perlwitz, J., Perlwitz, J., Rind, D., Romanou, A., Shindell, D., Stone, P., Sun, S., Tausnev, N., Thresher, D., Wielicki, B., Wong, T., Yao, M., and Zhang, S.: Efficacy of climate forcings, Journal of Geophysical Research: Atmospheres, 110, D18 104, doi:10.1029/2005JD005776, 2005.

Hegdahl, T. J., Tallaksen, L. M., Engeland, K., Burkhart, J. F., and Xu, C.-Y.: Discharge sensitivity to snowmelt parameterization: a case study for Upper Beas basin in Himachal Pradesh, India, Hydrology Research, 47, 683–700, doi:10.2166/nh.2016.047, 2016.

Hegde, P., Pant, P., Naja, M., Dumka, U. C., and Sagar, R.: South Asian dust episode in June 2006: Aerosol observations in the central Himalayas, Geophysical Research Letters, 34, L23 802, doi:10.1029/2007GL030692, 2007.

Hienola, A. I., Pietikäinen, J.-P., Jacob, D., Pozdun, R., Petäjä, T., Hyvärinen, A.-P., Sogacheva, L., Kerminen, V.-M., Kulmala, M., and Laaksonen, A.: Black carbon concentration and deposition estimations in Finland by the regional aerosol-climate model REMO-HAM, Atmospheric Chemistry and Physics, 13, 4033–4055, doi:10.5194/acp-13-4033-2013, 2013.

Higuchi, K. and Nagoshi, A.: Effect of particulate matter in surface snow layers on the albedo of perennial snow patches, Isotopes and Impurities in Snow and Ice, IAHS publication, 118, 95–97, 1977.

Hock, R.: Temperature index melt modelling in mountain areas, Journal of Hydrology, 282, 104–115, doi:10.1016/S0022-1694(03)00257-9, 2003.

Hock, R., Rees, G., Williams, M. W., and Ramirez, E.: Contribution from glaciers and snow cover to runoff from mountains in different climates, Hydrological Processes, 20, 2089–2090, doi:10.1002/hyp.6206, 2006.

Hong, S.-Y., Noh, Y., and Dudhia, J.: A New Vertical Diffusion Package with an Explicit Treatment of Entrainment Processes, Monthly Weather Review, 134, 2318–2341, doi:10.1175/MWR3199.1, 2006.

Iacono, M. J., Delamere, J. S., Mlawer, E. J., Shephard, M. W., Clough, S. A., and Collins, W. D.: Radiative forcing by long-lived greenhouse gases: Calculations with the AER radiative transfer models, Journal of Geophysical Research: Atmospheres, 113, D13 103, doi:10.1029/2008JD009944, 2008.

IPCC, W. G. I.: Climate Change 2013: The Physical Science Basis. Contribution of Working Group I to the Fifth Assessment Report of the Intergovernmental Panel on Climate Change, Cambridge University Press, Cambridge, United Kingdom and New York, NY, USA, doi: 10.1017/CBO9781107415324, 2013.

Jacobi, H.-W., Lim, S., Ménégoz, M., Ginot, P., Laj, P., Bonasoni, P., Stocchi, P., Marinoni, A., and Arnaud, Y.: Black carbon in snow in the upper Himalayan Khumbu Valley, Nepal: observations and modeling of the impact on snow albedo, melting, and radiative forcing, The Cryosphere, 9, 1685–1699, doi:10.5194/tc-9-1685-2015, 2015.

Jacobson, M. Z.: Climate response of fossil fuel and biofuel soot, accounting for soot's feedback to snow and sea ice albedo and emissivity, Journal of Geophysical Research: Atmospheres, 109, D21 201, doi:10.1029/2004JD004945, 2004.

Jain, S. K., Agarwal, P. K., and Singh, V. P.: Hydrology and Water Resources of India, Water Science and Technology Library, Springer, Dordrecht, The Netherlands, 2007.

Jayawardena, A. W., Muttil, N., and Lee, J. H.: Comparative Analysis of Data-Driven and GIS-Based Conceptual Rainfall-Runoff Model, Journal of Hydrologic Engineering, 11, doi: 10.1061/(ASCE)1084-0699(2006)11:1(1), 2006.

Jeelani, G., Feddema, J. J., van der Veen, C. J., and Stearns, L.: Role of snow and glacier melt in controlling river hydrology in Liddar watershed (western Himalaya) under current and future climate, Water Resources Research, 48, 1–16, doi:10.1029/2011WR011590, 2012.

Joseph, J. H., Wiscombe, W. J., and Weinman, J. A.: The Delta-Eddington Approximation for Radiative Flux Transfer, Journal of the Atmospheric Sciences, 33, 2452–2459, doi:10.1175/1520-0469(1976)033<2452:TDEAFR>2.0.CO;2, 1976.

Junghans, N., Cullmann, J., and Huss, M.: Evaluating the effect of snow and ice melt in an Alpine headwater catchment and further downstream in the River Rhine, Hydrological Sciences Journal, 56, 981–993, doi:10.1080/02626667.2011.595372, 2011.

Kapil, J. C., Prasher, C., Datt, P., and Satyawali, P. K.: Growth of melt-freeze clusters and formation of impeding layers to water flow in snow irradiated by a sun simulator under controlled laboratory conditions, Annals of Glaciology, 51, 19–26, doi:10.3189/172756410791386599, 2010.

Kashiwase, H., Ohshima, K. I., Nihashi, S., and Eicken, H.: Evidence for ice-ocean albedo feedback in the Arctic Ocean shifting to a seasonal ice zone., Scientific reports, 7, 8170, doi:10.1038/s41598-017-08467-z, 2017.

Kaspari, S., McKenzie Skiles, S., Delaney, I., Dixon, D., and Painter, T. H.: Accelerated glacier melt on Snow Dome, Mount Olympus, Washington, USA, due to deposition of black carbon and mineral dust from wildfire, Journal of Geophysical Research: Atmospheres, 120, 2793–2807, doi:10.1002/2014JD022676, 2015.

Kaspari, S. D., Schwikowski, M., Gysel, M., Flanner, M. G., Kang, S., Hou, S., and Mayewski, P. A.: Recent increase in black carbon concentrations from a Mt. Everest ice core spanning 1860-2000 AD, Geophysical Research Letters, 38, L04 703, doi:10.1029/2010GL046096, 2011.

Kawagoe, S., Kazama, S., and Ranjan Sarukkalige, P.: Assessment of snowmelt triggered landslide hazard and risk in Japan, Cold Regions Science and Technology, 58, 120–129, doi:10.1016/j.coldregions.2009.05.004, 2009.

Keyes, R. W.: The Impact of Moore's Law, IEEE Solid-State Circuits Society Newsletter, 11, 25–27, doi:10.1109/N-SSC.2006.4785857, 2006.

Kim, H., Kang, S. M., Hwang, Y.-T., and Yang, Y.-M.: Sensitivity of the Climate Response to the Altitude of Black Carbon in the Northern Subtropics in an Aquaplanet GCM, Journal of Climate, 28, 6351–6359, doi:10.1175/JCLI-D-15-0037.1, 2015.

Kirchner, J. W.: Catchments as simple dynamical systems: Catchment characterization, rainfall-runoff modeling, and doing hydrology backward, Water Resources Research, 45, W2429, doi:10.1029/2008WR006912, 2009.

Klimont, Z., Höglund-Isaksson, L., Heyes, C., Rafaj, P., Schöpp, W., Cofala, J., Borken-Kleefeld, J., Purohit, P., Kupiainen, K., Winiwarter, W., Amann, M., Zhao, B., Wang, S., Bertok, I., and Sander, R.: Global scenarios of air pollutants and methane: 1990-2050, In preparation for ACPD, 2016.

Klimont, Z., Kupiainen, K., Heyes, C., Purohit, P., Cofala, J., Rafaj, P., Borken-Kleefeld, J., and Schöpp, W.: Global anthropogenic emissions of particulate matter including black carbon, Atmospheric Chemistry and Physics, 17, 8681–8723, doi:10.5194/acp-17-8681-2017, 2017.

Koch, D., Menon, S., Del Genio, A., Ruedy, R., Alienov, I., and Schmidt, G. A.: Distinguishing Aerosol Impacts on Climate over the Past Century, Journal of Climate, 22, 2659–2677, doi:10.1175/2008JCLI2573.1, 2009.

Kolberg, S. and Gottschalk, L.: Interannual stability of grid cell snow depletion curves as estimated from MODIS images, Water Resources Research, 46, W11 555, doi:10.1029/2008WR007617, 2010.

Kolberg, S., Rue, H., and Gottschalk, L.: A Bayesian spatial assimilation scheme for snow coverage observations in a gridded snow model, Hydrology and Earth System Sciences, 10, 369–381, doi:10.5194/hess-10-369-2006, 2006.

Kolberg, S. A. and Gottschalk, L.: Updating of snow depletion curve with remote sensing data, Hydrological Processes, 20, 2363–2380, doi:10.1002/hyp.6060, 2006.

Krinner, G., Boucher, O., and Balkanski, Y.: Ice-free glacial northern Asia due to dust deposition on snow, Climate Dynamics, 27, 613–625, doi:10.1007/s00382-006-0159-z, 2006.

Kumar, V., Singh, P., and Singh, V.: Snow and glacier melt contribution in the Beas River at Pandoh Dam, Himachal Pradesh, India, Hydrological Sciences Journal, 52, 376–388, doi: 10.1623/hysj.52.2.376, 2007.

Lachapelle, E. R.: Field Guide to Snow Crystals, University of Washington Press, 1969.

Lau, K.-M. and Kim, K.-M.: Observational relationships between aerosol and Asian monsoon rainfall, and circulation, Geophysical Research Letters, 33, L21 810, doi:10.1029/2006GL027546, 2006.

Lau, W. K. M., Kim, M.-K., Kim, K.-M., and Lee, W.-S.: Enhanced surface warming and accelerated snow melt in the Himalayas and Tibetan Plateau induced by absorbing aerosols, Environmental Research Letters, 5, 025 204, doi:10.1088/1748-9326/5/2/025204, 2010.

Leclercq, P.: Glacier fluctuations, global temperature and sea-level change, Ph.D. thesis, Utrecht, Netherlands, 2012.

Li, D., Wrzesien, M. L., Durand, M., Adam, J., and Lettenmaier, D. P.: How much runoff originates as snow in the western United States, and how will that change in the future?, Geophysical Research Letters, 44, 6163–6172, doi:10.1002/2017GL073551, 2017a.

Li, H., Xu, C.-Y., and Jain, S. K.: Modelling runoff and its components in Himalayan basins, Hydrology in a Changing World: Environmental and Human Dimensions - Proceedings of FRIEND-Water 2014, pp. 158–164, doi:10.1002/hyp.9668, 2014.

Li, H., Beldring, S., Xu, C.-Y., Huss, M., Melvold, K., and Jain, S. K.: Integrating a glacier retreat model into a hydrological model - Case studies of three glacierised catchments in Norway and Himalayan region, Journal of Hydrology, 527, 656–667, doi:10.1016/j.jhydrol.2015.05.017, 2015a.

Li, H., Xu, C.-Y., Beldring, S., Tallaksen, L. M., and Jain, S. K.: Water Resources Under Climate Change in Himalayan Basins, Water Resources Management, 30, 843–859, doi:10.1007/s11269-015-1194-5, 2015b.

Li, L., Gochis, D. J., Sobolowski, S., Mesquita, M. D. S., Burnash, R. J. C., Ferral, R. L., and McGuire, R.: Evaluating the present annual water budget of a Himalayan headwater river basin using a high-resolution atmosphere-hydrology model, Journal of Geophysical Research: Atmospheres, 122, 4786–4807, doi:10.1002/2016JD026279, 2017b.

Liston, G. E.: Interrelationships among Snow Distribution, Snowmelt, and Snow Cover Depletion: Implications for Atmospheric, Hydrologic, and Ecologic Modeling, Journal of Applied Meteorology, 38, 1474–1487, doi:10.1175/1520-0450(1999)038<1474:IASDSA>2.0.CO;2, 1999.

Liston, G. E.: Representing Subgrid Snow Cover Heterogeneities in Regional and Global Models, Journal of Climate, 17, 1381–1397, 2004.

Lutz, S., Anesio, A. M., Raiswell, R., Edwards, A., Newton, R. J., Gill, F., and Benning, L. G.: The biogeography of red snow microbiomes and their role in melting arctic glaciers, Nature Communications, 7, 11 968, doi:10.1038/ncomms11968, 2016.

Madsen, H.: Automatic calibration of a conceptual rainfall–runoff model using multiple objectives, Journal of Hydrology, 235, 276–288, doi:10.1016/S0022-1694(00)00279-1, 2000.

Madsen, H., Wilson, G., and Ammentorp, H. C.: Comparison of different automated strategies for calibration of rainfall-runoff models, Journal of Hydrology, 261, 48–59, doi:https://doi.org/10.1016/S0022-1694(01)00619-9, 2002.

Malik, M. J., van der Velde, R., Vekerdy, Z., and Su, Z.: Improving modeled snow albedo estimates during the spring melt season, Journal of Geophysical Research: Atmospheres, 119, 7311–7331, doi:10.1002/2013JD021344, 2014.

Marshall, S. E.: A Physical Parameterization of Snow Albedo for Use in Climate Models, Ph.D. thesis, University of Colorado, 1989.

Maskey, S., Chong, K. Y., Seo, A., Park, M., Lee, K., and Park, K.: Cloud Condensation Nuclei Activation of Internally Mixed Black Carbon Particles, Aerosol and Air Quality Research, 17, 867–877, doi:10.4209/aaqr.2016.06.0229, 2017.

Maussion, F., Scherer, D., Finkelnburg, R., Richters, J., Yang, W., and Yao, T.: WRF simulation of a precipitation event over the Tibetan Plateau, China - an assessment using remote sensing and ground observations, Hydrology and Earth System Sciences, 15, 1795–1817, doi:10.5194/hess-15-1795-2011, 2011.

Ménégoz, M., Krinner, G., Balkanski, Y., Boucher, O., Cozic, A., Lim, S., Ginot, P., Laj, P., Gallée, H., Wagnon, P., Marinoni, A., Jacobi, H. W., Qian, Y., Wang, H., Zhang, R., Flanner, M. G., and Rasch, P. J.: Snow cover sensitivity to black carbon deposition in the Himalayas: from atmospheric and ice core measurements to regional climate simulations, Atmospheric Chemistry and Physics, 14, 4237–4249, doi:10.5194/acp-14-4237-2014, 2014.

Ming, J., Cachier, H., Xiao, C., Qin, D., Kang, S., Hou, S., and Xu, J.: Black carbon record based on a shallow Himalayan ice core and its climatic implications, Atmospheric Chemistry and Physics, 8, 1343–1352, doi:10.5194/acp-8-1343-2008, 2008.

Molina, L. T., Gallardo, L., Andrade, M., Baumgardner, D., Borbor-Córdova, M., Bórquez, R., Casassa, G., Cereceda-Balic, F., Dawidowski, L., Garreaud, R., Huneeus, N., Lambert, F., McCarty, J. L., Mc Phee, J., Mena-Carrasco, M., Raga, G. B., Schmitt, C., and Schwarz, J. P.: Pollution and its Impacts on the South American Cryosphere, Earth's Future, 3, 345–369, doi:10.1002/2015EF000311, 2015.

Moore, G.: Chapter 7: Moore's law at 40, in: Understanding Moore's Law: Four Decades of Innovation, edited by Brock, D., pp. 67–84, Chemical Heritage Foundation, Philadelphia, United States, 2006.

Nash, J. E. and Sutcliffe, J. V.: River flow forecasting through conceptual models part I - A discussion of principles, Journal of Hydrology, 10, 282–290, doi:10.1016/0022-1694(70)90255-6, 1970.

Neff, J. C., Reynolds, R. L., Belnap, J., and Lamothe, P.: Multi-decadal impacts of grazing on soil physical and biogeochemical properties in southeast Utah, Ecological Applications, 15, 87–95, doi:10.1890/04-0268, 2005.

Nesje, A., Dahl, S. O., Matthews, J. A., and Berrisford, M. S.: A 4500-yr record of river floods obtained from a sediment core in Lake Atnsjøen, eastern Norway, J. Paleolimnol., 25, 329–342, 2000.

Newman, A. J., Clark, M. P., Sampson, K., Wood, A., Hay, L. E., Bock, A., Viger, R. J., Blodgett, D., Brekke, L., Arnold, J. R., Hopson, T., and Duan, Q.: Development of a large-sample watershed-scale hydrometeorological data set for the contiguous USA: data set characteristics and assessment of regional variability in hydrologic model performance, Hydrology and Earth System Sciences, 19, 209–223, doi:10.5194/hess-19-209-2015, 2015.

Niu, G.-Y., Yang, Z.-L., Mitchell, K. E., Chen, F., Ek, M. B., Barlage, M., Kumar, A., Manning, K., Niyogi, D., Rosero, E., Tewari, M., and Xia, Y.: The community Noah land surface model with multiparameterization options (Noah-MP): 1. Model description and evaluation with local-scale measurements, Journal of Geophysical Research: Atmospheres, 116, D12 109, doi:10.1029/2010JD015139, 2011.

Nyberg, R. and Rapp, A.: Extreme erosional events and natural hazards in Scandinavian mountains, Ambio, 27, 292–299, 1998.

Oaida, C. M., Xue, Y., Flanner, M. G., Skiles, S. M., De Sales, F., and Painter, T. H.: Improving snow albedo processes in WRF/SSiB regional climate model to assess impact of dust and black carbon in snow on surface energy balance and hydrology over western U.S., Journal of Geophysical Research: Atmospheres, 120, 3228–3248, doi:10.1002/2014JD022444, 2015.

O'Loughlin, G., Huber, W., and Chocat, B.: Rainfall-runoff processes and modelling, Journal of Hydraulic Research, 34, 733–751, doi:10.1080/00221689609498447, 1996.

Orth, R., Staudinger, M., Seneviratne, S. I., Seibert, J., and Zappa, M.: Does model performance improve with complexity? A case study with three hydrological models, Journal of Hydrology, 523, 147–159, doi:10.1016/j.jhydrol.2015.01.044, 2015.

Painter, T. H., Barrett, A. P., Landry, C. C., Neff, J. C., Cassidy, M. P., Lawrence, C. R., McBride, K. E., and Farmer, G. L.: Impact of disturbed desert soils on duration of mountain snow cover, Geophysical Research Letters, 34, L12 502, doi:10.1029/2007GL030284, 2007.

Painter, T. H., Deems, J. S., Belnap, J., Hamlet, A. F., Landry, C. C., and Udall, B.: Response of Colorado River runoff to dust radiative forcing in snow, Proceedings of the National Academy of Sciences of the United States of America, 107, 17 125–17 130, doi:10.1073/pnas.0913139107/-/DCSupplemental, 2010.

Painter, T. H., Bryant, A. C., and Skiles, S. M.: Radiative forcing by light absorbing impurities in snow from MODIS surface reflectance data, Geophysical Research Letters, 39, L17 502, doi:10.1029/2012GL052457, 2012a.

Painter, T. H., Skiles, S. M., Deems, J. S., Bryant, A. C., and Landry, C. C.: Dust radiative forcing in snow of the Upper Colorado River Basin: 1. A 6 year record of energy balance, radiation, and dust concentrations, Water Resources Research, 48, W07 521, doi:10.1029/2012WR011985, 2012b.

Painter, T. H., McKenzie Skiles, S., Deems, J. S., Tyler Brandt, W., and Dozier, J.: Variation in rising limb of Colorado River snowmelt runoff hydrograph controlled by dust radiative forcing in snow, Geophysical Research Letters, 45, 797–808, doi:10.1002/2017GL075826, 2017.

Pedersen, C. A. and Winther, J.-G.: Intercomparison and validation of snow albedo parameterization schemes in climate models, Climate Dynamics, 25, 351–362, doi:10.1007/s00382-005-0037-0, 2005.

Pepin, N., Bradley, R. S., Diaz, H. F., Baraer, M., Caceres, E. B., Forsythe, N., Fowler, H., Greenwood, G., Hashmi, M. Z., Liu, X. D., Miller, J. R., Ning, L., Ohmura, A., Palazzi, E., Rangwala, I., Schöner, W., Severskiy, I., Shahgedanova, M., Wang, M. B., Williamson, S. N., and Yang, D. Q.: Elevation-dependent warming in mountain regions of the world, Nature Climate Change, 5, 424–430, doi:10.1038/nclimate2563, 2015.

Petzold, A., Ogren, J. A., Fiebig, M., Laj, P., Li, S.-M., Baltensperger, U., Holzer-Popp, T., Kinne, S., Pappalardo, G., Sugimoto, N., Wehrli, C., Wiedensohler, A., and Zhang, X.-Y.: Recommendations for reporting "black carbon" measurements, Atmospheric Chemistry and Physics, 13, 8365–8379, doi:10.5194/acp-13-8365-2013, 2013.

Pietikäinen, J.-P., O'Donnell, D., Teichmann, C., Karstens, U., Pfeifer, S., Kazil, J., Podzun, R., Fiedler, S., Kokkola, H., Birmili, W., O'Dowd, C., Baltensperger, U., Weingartner, E., Gehrig, R., Spindler, G., Kulmala, M., Feichter, J., Jacob, D., and Laaksonen, A.: The regional aerosol-climate model REMO-HAM, Geoscientific Model Development, 5, 1323–1339, doi:10.5194/gmd-5-1323-2012, 2012.

Pietikäinen, J.-P., Kupiainen, K., Klimont, Z., Makkonen, R., Korhonen, H., Karinkanta, R., Hyvärinen, A.-P., Karvosenoja, N., Laaksonen, A., Lihavainen, H., and Kerminen, V.-M.: Impacts of emission reductions on aerosol radiative effects, Atmospheric Chemistry and Physics, 15, 5501–5519, doi:10.5194/acp-15-5501-2015, 2015.

Planck, M. and Masius, M.: The Theory of Heat Radiation, Blakiston's Son & Co., Phiadelphia, 1914.

Powell, M.: The BOBYQA algorithm for bound constrained optimization without derivatives, Cambridge NA Report NA2009/06, pp. 1–39, 2009.

Prasad, A. K. and Singh, R. P.: Changes in Himalayan snow and glacier cover between 1972 and 2000, Eos, Transactions American Geophysical Union, 88, 326–326, doi:10.1029/2007EO330002, 2007.

Priestley, C. H. B. and Taylor, R. J.: On the assessment of surface heat flux and evaporation using large-scale parameters, Monthly Weather Review, 100, 81–92, 1972.

Qian, Y., Gustafson, W. I., Leung, L. R., and Ghan, S. J.: Effects of soot-induced snow albedo change on snowpack and hydrological cycle in western United States based on Weather Research and Forecasting chemistry and regional climate simulations, Journal of Geophysical Research: Atmospheres, 114, D03 108, doi:10.1029/2008JD011039, 2009.

Qian, Y., Flanner, M. G., Leung, L. R., and Wang, W.: Sensitivity studies on the impacts of Tibetan Plateau snowpack pollution on the Asian hydrological cycle and monsoon climate, Atmospheric Chemistry and Physics, 11, 1929–1948, doi:10.5194/acp-11-1929-2011, 2011.

Qian, Y., Wang, H., Zhang, R., Flanner, M. G., and Rasch, P. J.: A sensitivity study on modeling black carbon in snow and its radiative forcing over the Arctic and Northern China, Environmental Research Letters, 9, 064 001, doi:10.1088/1748-9326/9/6/064001, 2014a.

Qian, Y., Yasunari, T. J., Doherty, S. J., Flanner, M. G., Lau, W. K. M., Ming, J., Wang, H., Wang, M., Warren, S. G., and Zhang, R.: Light-absorbing particles in snow and ice: Measurement and modeling of climatic and hydrological impact, Advances in Atmospheric Sciences, 32, 64–91, doi:10.1007/s00376-014-0010-0, 2014b.

Raleigh, M. S., Landry, C. C., Hayashi, M., Quinton, W. L., and Lundquist, J. D.: Approximating snow surface temperature from standard temperature and humidity data: New possibilities for snow model and remote sensing evaluation, Water Resources Research, 49, 8053–8069, doi:10.1002/2013WR013958, 2013.

Ramanathan, V. and Carmichael, G.: Global and regional climate changes due to black carbon, Nature Geoscience, 1, 221–227, doi:10.1038/ngeo156, 2008.

Ramanathan, V., Crutzen, P. J., Kiehl, J. T., and Rosenfeld, D.: Aerosols, Climate, and the Hydrological Cycle, Science, 294, 2119–2124, doi:10.1126/science.1064034, 2001.

Ramanathan, V., Li, F., Ramana, M. V., Praveen, P. S., Kim, D., Corrigan, C. E., Nguyen, H., Stone, E. A., Schauer, J. J., Carmichael, G. R., Adhikary, B., and Yoon, S. C.: Atmospheric brown clouds: Hemispherical and regional variations in long-range transport, absorption, and radiative forcing, Journal of Geophysical Research: Atmospheres, 112, D22S21, doi:10.1029/2006JD008124, 2007.

Rasmussen, R., Liu, C., Ikeda, K., Gochis, D., Yates, D., Chen, F., Tewari, M., Barlage, M., Dudhia, J., Yu, W., Miller, K., Arsenault, K., Grubisic, V., Thompson, G., and Gutmann, E.: High-Resolution Coupled Climate Runoff Simulations of Seasonal Snowfall over Colorado: A Process Study of Current and Warmer Climate, Journal of Climate, 24, 3015–3048, doi:10.1175/2010JCLI3985.1, 2011.

Rasmussen, R., Ikeda, K., Liu, C., Gochis, D., Clark, M., Dai, A., Gutmann, E., Dudhia, J., Chen, F., Barlage, M., Yates, D., and Zhang, G.: Climate Change Impacts on the Water Balance of the Colorado Headwaters: High-Resolution Regional Climate Model Simulations, Journal of Hydrometeorology, 15, 1091–1116, doi:10.1175/JHM-D-13-0118.1, 2014.

Rhodes, J. J., Armstrong, R. L., and Warren, S. G.: Mode of formation of "ablation hollows" controlled by dirt content of snow, Journal of Glaciology, 33, 135–139, 1987.

Robinson, M., Rodda, J. C., and Sutcliffe, J. V.: Long-term environmental monitoring in the UK: origins and achievements of the Plynlimon catchment study, Transactions of the Institute of British Geographers, 38, 451–463, doi:10.1111/j.1475-5661.2012.00534.x, 2013.

Rosenthal, W., Saleta, J., and Dozier, J.: Scanning electron microscopy of impurity structures in snow, Cold Regions Science and Technology, 47, 80–89, doi:10.1016/j.coldregions.2006.08.006, 2007.

Roy, A., Royer, A., Montpetit, B., Bartlett, P. A., and Langlois, A.: Snow specific surface area simulation using the one-layer snow model in the Canadian LAnd Surface Scheme (CLASS), The Cryosphere, 7, 961–975, doi:10.5194/tc-7-961-2013, 2013.

Sandlund, O. T. and Aagaard, K., eds.: The Atna River: Studies in an Alpine-Boreal Watershed, vol. 521 of *Hydrobiologia*, Springer, Dordrecht, doi:10.1007/978-1-4020-2254-8, 2004.

Schaepman-Strub, G., Schaepman, M. E., Painter, T. H., Dangel, S., and Martonchik, J. V.: Reflectance quantities in optical remote sensing—definitions and case studies, Remote Sensing of Environment, 103, 27–42, doi:10.1016/j.rse.2006.03.002, 2006.

Seibert, J. and Vis, M. J. P.: Teaching hydrological modeling with a user-friendly catchment-runoff-model software package, Hydrology and Earth System Sciences, 16, 3315–3325, doi:10.5194/hess-16-3315-2012, 2012.

Serreze, M. C. and Francis, J. A.: The Arctic Amplification Debate, Climatic Change, 76, 241–264, doi:10.1007/s10584-005-9017-y, 2006.

Shekhar, M. S., Chand, H., Kumar, S., Srinivasan, K., and Ganju, A.: Climate change studies in the western Himalaya, Annals of Glaciology, 51, 105–112, doi:10.1029/2005GL023528., 2010.

Shindell, D. and Faluvegi, G.: Climate response to regional radiative forcing during the twentieth century, Nature Geoscience, 2, 294–300, doi:10.1038/ngeo473, 2009.

Singh, P. and Jain, S. K.: Modelling of streamflow and its components for a large Himalayan basin with predominant snowmelt yields, Hydrological Sciences Journal, 48, 257–276, doi:10.1623/hysj.48.2.257.44693, 2003.

Singh, P. and Kumar, N.: Effect of orography on precipitation in the western Himalayan region, Journal of Hydrology, 199, 183–206, doi:10.1016/S0022-1694(96)03222-2, 1997.

Skamarock, W. C., Klemp, J. B., Dudhia, J., Gill, D. O., Barker, D., Duda, M. G., Huang, X.-y., Wang, W., and Powers, J. G.: A Description of the Advanced Research WRF Version 3, Tech. rep., Boulder, Colorado, USA, doi:10.5065/D68S4MVH, 2008.

Skaugen, T.: Modelling the spatial variability of snow water equivalent at the catchment scale, Hydrology and Earth System Sciences, 11, 1543–1550, doi:10.5194/hess-11-1543-2007, 2007.

Skaugen, T. and Randen, F.: Modeling the spatial distribution of snow water equivalent, taking into account changes in snow-covered area, Annals of Glaciology, 54, 305–313, doi:10.3189/2013AoG62A162, 2013.

Skaugen, T. and Weltzien, I. H.: A model for the spatial distribution of snow water equivalent parameterized from the spatial variability of precipitation, The Cryosphere, 10, 1947–1963, doi:10.5194/tc-10-1947-2016, 2016.

Skiles, S. M., Painter, T. H., Deems, J. S., Bryant, A. C., and Landry, C. C.: Dust radiative forcing in snow of the Upper Colorado River Basin: 2. Interannual variability in radiative forcing and snowmelt rates, Water Resources Research, 48, W07 522, doi:10.1029/2012WR011986, 2012.

Sterle, K. M., McConnell, J. R., Dozier, J., Edwards, R., and Flanner, M. G.: Retention and radiative forcing of black carbon in eastern Sierra Nevada snow, The Cryosphere, 7, 365–374, doi:10.5194/tc-7-365-2013, 2013.

Stohl, A. and Thomson, D. J.: A Density Correction for Lagrangian Particle Dispersion Models, Boundary-Layer Meteorology, 90, 155–167, doi:10.1023/A:1001741110696, 1999.

Stohl, A., Hittenberger, M., and Wotawa, G.: Validation of the lagrangian particle dispersion model FLEXPART against large-scale tracer experiment data, Atmospheric Environment, 32, 4245–4264, doi:10.1016/S1352-2310(98)00184-8, 1998.

Stohl, A., Forster, C., Frank, A., Seibert, P., and Wotawa, G.: Technical note: The Lagrangian particle dispersion model FLEXPART version 6.2, Atmospheric Chemistry and Physics, 5, 2461–2474, doi:10.5194/acp-5-2461-2005, 2005.

Sumner, N. R., Fleming, P. M., and Bates, B. C.: Calibration of a modified SFB model for twenty-five Australian catchments using simulated annealing, Journal of Hydrology, 197, 166–188, doi:10.1016/S0022-1694(96)03277-5, 1997.

Syed, K. H., Goodrich, D. C., Myers, D. E., and Sorooshian, S.: Spatial characteristics of thunderstorm rainfall fields and their relation to runoff, Journal of Hydrology, 271, 1–21, doi:10.1016/S0022-1694(02)00311-6, 2003.

Taillandier, A.-S., Domine, F., Simpson, W. R., Sturm, M., and Douglas, T. A.: Rate of decrease of the specific surface area of dry snow: Isothermal and temperature gradient conditions, Journal of Geophysical Research, 112, F03 003, doi:10.1029/2006JF000514, 2007.

Tetzlaff, D. and Uhlenbrook, S.: Significance of spatial variability in precipitation for process-oriented modelling: results from two nested catchments using radar and ground station data, Hydrology and Earth System Sciences, 9, 29–41, doi:10.5194/hess-9-29-2005, 2005.

Thackeray, C. W. and Fletcher, C. G.: Snow albedo feedback: Current knowledge, importance, outstanding issues and future directions, Progress in Physical Geography: Earth and Environment, 40, 392–408, doi:10.1177/0309133315620999, 2016.

Thompson, G., Field, P. R., Rasmussen, R. M., and Hall, W. D.: Explicit Forecasts of Winter Precipitation Using an Improved Bulk Microphysics Scheme. Part II: Implementation of a New Snow Parameterization, Monthly Weather Review, 136, 5095–5115, doi:10.1175/2008MWR2387.1, 2008.

Tiedtke, M.: A Comprehensive Mass Flux Scheme for Cumulus Parameterization in Large-Scale Models, Monthly Weather Review, 117, 1779–1800, doi:10.1175/1520-0493(1989)117<1779:ACMFSF>2.0.CO;2, 1989.

Toon, O. B., Mckay, C. P., and Ackerman, T. P.: Rapid Calculation of Radiative Heating Rates and Photodissociation Rates in Inhomogeneous Multiple Scattering Atmospheres, Journal of Geophysical Research, 94, 16,287–16,301, 1989.

Tuzet, F., Dumont, M., Lafaysse, M., Picard, G., Arnaud, L., Voisin, D., Lejeune, Y., Charrois, L., Nabat, P., and Morin, S.: A multilayer physically based snowpack model simulating direct and indirect radiative impacts of light-absorbing impurities in snow, The Cryosphere, 11, 2633–2653, doi:10.5194/tc-11-2633-2017, 2017.

Twomey, S. A., Piepgrass, M., and Wolfe, T. L.: An assessment of the impact of pollution on global cloud albedo, Tellus B: Chemical and Physical Meteorology, 36, 356–366, doi:10.3402/tellusb.v36i5.14916, 1984.

van de Hulst, H. C.: Light scattering by small particles, John Wiley and Sons, New York, doi:10.1002/qj.49708436025, 1957.

van der Werf, G. R., Randerson, J. T., Giglio, L., Collatz, G. J., Mu, M., Kasibhatla, P. S., Morton, D. C., DeFries, R. S., Jin, Y., and van Leeuwen, T. T.: Global fire emissions and the contribution of deforestation, savanna, forest, agricultural, and peat fires (1997-2009), Atmospheric Chemistry and Physics, 10, 11 707–11 735, doi:10.5194/acp-10-11707-2010, 2010.

Wang, Q. J.: The Genetic Algorithm and Its Application to Calibrating Conceptual Rainfall-Runoff Models, Water Resources Research, 27, 2467–2471, doi:10.1029/91WR01305, 1991.

Wang, X., Doherty, S. J., and Huang, J.: Black carbon and other light-absorbing impurities in snow across Northern China, Journal of Geophysical Research: Atmospheres, 118, 1471–1492, doi:10.1029/2012JD018291, 2013.

Warren, S. G.: Can black carbon in snow be detected by remote sensing?, Journal of Geophysical Research: Atmospheres, 118, 779–786, doi:10.1029/2012JD018476, 2013.

Warren, S. G. and Wiscombe, W. J.: A Model for the Spectral Albedo of Snow. II: Snow Containing Atmospheric Aerosols, Journal of the Atmospheric Sciences, 37, 2734–2745, doi:10.1175/1520-0469(1980)037<2734:AMFTSA>2.0.CO;2, 1980.

Weedon, G. P., Balsamo, G., Bellouin, N., Gomes, S., Best, M. J., and Viterbo, P.: The WFDEI meteorological forcing data set: WATCH Forcing Data methodology applied to ERA-Interim reanalysis data, Water Resources Research, 50, 7505–7514, doi:10.1002/2014WR015638, 2014.

Wiscombe, W. J.: Improved Mie scattering algorithms, Applied Optics, 19, 1505–1509, doi: 10.1364/AO.19.001505, 1980.

Wiscombe, W. J. and Warren, S. G.: A Model for the Spectral Albedo of Snow. I: Pure Snow, Journal of the Atmospheric Sciences, 37, 2712–2733, doi:10.1175/1520-0469(1980) 037<2712:AMFTSA>2.0.CO;2, 1980.

Wold, K.: Vann, snø og is. Nasjonalatlas for Norge., Statens kartverk, 1992.

Xu, B., Cao, J., Hansen, J., Yao, T., Joswiak, D. R., Wang, N., Wu, G., Wang, M., Zhao, H., Yang, W., Liu, X., and He, J.: Black soot and the survival of Tibetan glaciers, Proceedings of the National Academy of Sciences, 106, 22 114–22 118, doi:10.1073/pnas.0910444106, 2009.

Xu, B., Cao, J., Joswiak, D. R., Liu, X., Zhao, H., and He, J.: Post-depositional enrichment of black soot in snow-pack and accelerated melting of Tibetan glaciers, Environmental Research Letters, 7, 014 022, doi:10.1088/1748-9326/7/1/014022, 2012.

Xu, X., Lu, C., Shi, X., and Gao, S.: World water tower: An atmospheric perspective, Geophysical Research Letters, 35, L20 815, doi:10.1029/2008GL035867, 2008.

Yang, Z.-L., Niu, G.-Y., Mitchell, K. E., Chen, F., Ek, M. B., Barlage, M., Longuevergne, L., Manning, K., Niyogi, D., Tewari, M., and Xia, Y.: The community Noah land surface model with multiparameterization options (Noah-MP): 2. Evaluation over global river basins, Journal of Geophysical Research: Atmospheres, 116, D12 110, doi:10.1029/2010JD015140, 2011.

Zhang, C., Wang, Y., and Hamilton, K.: Improved Representation of Boundary Layer Clouds over the Southeast Pacific in ARW-WRF Using a Modified Tiedtke Cumulus Parameterization Scheme, Monthly Weather Review, 139, 3489–3513, doi:10.1175/MWR-D-10-05091.1, 2011.

Zhang, R., Khalizov, A. F., Pagels, J., Zhang, D., Xue, H., and McMurry, P. H.: Variability in morphology, hygroscopicity, and optical properties of soot aerosols during atmospheric processing, Proceedings of the National Academy of Sciences, 105, 10 291–10 296, doi:10.1073/pnas.0804860105, 2008.

Zhang, Y., Kang, S., Cong, Z., Schmale, J., Sprenger, M., Li, C., Yang, W., Gao, T., Sillanpää, M., Li, X., Liu, Y., Chen, P., and Zhang, X.: Light-absorbing impurities enhance glacier albedo reduction in the southeastern Tibetan plateau, Journal of Geophysical Research: Atmospheres, 122, 6915–6933, doi:10.1002/2016JD026397, 2017.

Part II

Journal Publications

Paper II

Matt, F. N., Burkhart, J. F., Pietikäinen, J.-P. (2018): Modelling hydrologic impacts of light absorbing aerosol deposition on snow at the catchment scale, *Hydrology and Earth System Sciences, 22, 179-201*, doi:10.5194/hess-22-179-2018.

II

Hydrol. Earth Syst. Sci., 22, 179–201, 2018
https://doi.org/10.5194/hess-22-179-2018

Hydrology and Earth System Sciences
Open Access
EGU

Modelling hydrologic impacts of light absorbing aerosol deposition on snow at the catchment scale

Felix N. Matt[1], **John F. Burkhart**[1,2], **and Joni-Pekka Pietikäinen**[3]

[1]Department of Geosciences, University of Oslo, Oslo, Norway
[2]Statkraft AS, Oslo, Norway
[3]Finnish Meteorological Institute, Helsinki, Finland

Correspondence: Felix N. Matt (f.n.matt@geo.uio.no)

Received: 19 October 2016 – Discussion started: 15 November 2016
Revised: 21 October 2017 – Accepted: 7 November 2017 – Published: 10 January 2018

Abstract. Light absorbing impurities in snow and ice (LAISI) originating from atmospheric deposition enhance snowmelt by increasing the absorption of shortwave radiation. The consequences are a shortening of the snow duration due to increased snowmelt and, at the catchment scale, a temporal shift in the discharge generation during the spring melt season.

In this study, we present a newly developed snow algorithm for application in hydrological models that allows for an additional class of input variable: the deposition mass flux of various species of light absorbing aerosols. To show the sensitivity of different model parameters, we first use the model as a 1-D point model forced with representative synthetic data and investigate the impact of parameters and variables specific to the algorithm determining the effect of LAISI. We then demonstrate the significance of the radiative forcing by simulating the effect of black carbon (BC) deposited on snow of a remote southern Norwegian catchment over a 6-year period, from September 2006 to August 2012. Our simulations suggest a significant impact of BC in snow on the hydrological cycle. Results show an average increase in discharge of 2.5, 9.9, and 21.4 %, depending on the applied model scenario, over a 2-month period during the spring melt season compared to simulations where radiative forcing from LAISI is not considered. The increase in discharge is followed by a decrease in discharge due to a faster decrease in the catchment's snow-covered fraction and a trend towards earlier melt in the scenarios where radiative forcing from LAISI is applied. Using a reasonable estimate of critical model parameters, the model simulates realistic BC mixing ratios in surface snow with a strong annual cycle, showing increasing surface BC mixing ratios during spring melt as a consequence of melt amplification. However, we further identify large uncertainties in the representation of the surface BC mixing ratio during snowmelt and the subsequent consequences for the snowpack evolution.

1 Introduction

The representation of the seasonal snowpack is of outstanding importance in hydrological models aiming for application in cold or mountainous environments. In many mountain regions, the seasonal snowpack constitutes a major portion of the water budget, contributing up to 50 %, and even more, to the annual discharge (e.g. Junghans et al., 2011). Snowmelt plays a key role in the dynamic of the hydrology of catchments of various high mountain areas such as the Himalayas (Jeelani et al., 2012), the Alps (Junghans et al., 2011), and the Norwegian mountains (Engelhardt et al., 2014), and is an equally important contributor to streamflow generation as rain in these areas. Furthermore, timing and magnitude of the snowmelt are major predictors for flood (Berghuijs et al., 2016) and landslide (Kawagoe et al., 2009) forecasts, and important factors in water resource management and operational hydropower forecasting. Lastly, the extent and the temporal evolution of the snow cover is a controlling factor in the processes determining the growing season of plants (Jonas et al., 2008). For all these reasons, a good representation of the seasonal snowpack in hydrological models is paramount. However, there are large uncertainties in many variables specifying the temporal evolution of the snowpack,

and the snow albedo is one of the most important among those due to the direct effect on the energy input to the snowpack from solar radiation (Anderson, 1976). Fresh snow reflects most of the incoming solar radiation in the near-UV and visible spectrum (Warren and Wiscombe, 1980). However, as snow ages and snow grain size increases, the snow albedo will drop as a result of the altered scattering properties of the larger snow grains (Flanner and Zender, 2006). Furthermore, ambient conditions also play a large role. The ratio of diffuse and direct incoming shortwave radiation, the zenith angle of the sun, and the albedo of the underlying ground in combination with the snow thickness can have a large impact on the snow albedo (Warren and Wiscombe, 1980). Of recent significance is the role light absorbing impurities, or particles, which absorb in the range of the solar spectrum, have on albedo when present in the snowpack (e.g. Flanner et al., 2007; Painter et al., 2007; Skiles et al., 2012). These light absorbing impurities in snow and ice (LAISI) can originate from fossil fuel combustion and forest fires in the form of black carbon, BC, and organic carbon (Bond et al., 2013; AMAP, 2015), mineral dust (Painter et al., 2012), volcanic ash (Rhodes et al., 1987), organic compounds in soils (Wang et al., 2013), and biological activity (Lutz et al., 2016), and have species-specific radiative properties.

As LAISI lower the snow albedo, the effect on the snowmelt has the potential to alter the hydrological characteristics of catchments where snowmelt significantly contributes to the water budget. Recent research investigates the impact of LAISI on discharge generation in mountain regions at different scales. Qian et al. (2011) used a global climate model to simulate the effect black carbon and dust in snow have on the hydrological cycle of the Tibetan Plateau. They found a significant impact on the hydrology, with runoff increasing during late winter/early spring and decreasing during late spring/early summer due to a trend to earlier melt dates. Oaida et al. (2015) implemented radiative transfer calculations to determine snow albedo in the Simple Simplified Biosphere (SSiB) land surface model of the Weather Research and Forecasting (WRF) regional climate model. They showed that physically based snow albedo representation can be significantly improved by considering the deposition of light absorbing aerosols on snow. Qian et al. (2009) simulated hydrological impacts due to BC deposition in the western United States using WRF coupled with chemistry (WRF-Chem). They found a decrease in net snow accumulation and spring snowmelt due to BC-in-snow induced increase in surface air temperature.

Only a few studies have developed model approaches to resolve the impact of LAISI on snowmelt discharge generation at the catchment scale. Painter et al. (2010) showed that dust, transported from remote places to the Colorado River basin, can have severe implications for the hydrological regime due to disturbances to the discharge generation from snowmelt during the spring time, shifting the peak runoff by several weeks and leading to earlier snow-free catchments and a decrease in annual runoff. Kaspari et al. (2015) simulated the impact of BC and dust in snow on glacier melt on Mount Olympus, USA, by using measured concentrations in summer horizons and determining the radiative forcing via a radiative transfer model. Results indicate enhanced melt during a year of heavy nearby forest fires, coinciding with an increase in observed discharge from the catchment.

Despite these efforts, the direct integration of deposition mass fluxes of light absorbing aerosols in a catchment model is still lacking. To date, there is no rainfall–runoff model with a focus on runoff forecast at the catchment scale that is able to consider aerosol deposition mass fluxes alongside snowfall. On the other hand, there is evidence that including the radiative forcing of LAISI has the potential to improve the quality of hydrological predictions: Bryant et al. (2013) showed that during the melt period errors in the operational streamflow prediction of the National Weather Service Colorado Basin River Forecast Center are linearly related to dust radiative forcing in snow. They concluded that implementing the effect of LAISI on the snow reflectivity could improve hydrological predictions in regions prone to deposition of light absorbing aerosols on snow, which emphasizes the need for development of a suitable model approach. Furthermore, we continuously move towards hydrological models with an increasingly complex representation of the physical processes involved in the evolution of the seasonal snowpack. Heretofore there has been little focus on the factors related to LAISI, such as the impact of aerosol deposition on snow albedo, that may alter the timing and character of discharge generation at the catchment scale.

In this study, we address this deficiency by introducing a rainfall–runoff model with a newly developed snow algorithm that allows for a new class of model input variable: the deposition mass flux of different species of light absorbing aerosols. The model integrates snowpack dynamics forced by LAISI and allows for analysis at the catchment scale. The algorithm uses a radiative transfer model for snow to account dynamically for the impact of LAISI on the snow albedo and the subsequent impacts on the snowmelt and discharge generation. Aside from enabling the user to optionally apply deposition mass fluxes as model input, the algorithm depends on standard atmospheric input variables (precipitation, temperature, shortwave radiation, wind speed, and relative humidity). To enable a critical evaluation of the newly developed snowpack algorithm, we conduct two independent analyses: (i) a 1-D sensitivity study of critical model parameters, and (ii) a catchment-scale analysis of the impact of LAISI. In both analyses we use BC in snow from wet and dry deposition as a proxy for the impact of LAISI.

We first present an overview of the hydrological model used in this study and our algorithm to treat LAISI in Sect. 2. A description of the catchment used for our study and the input data sets is given in Sect. 3. Section 4 describes the 1-D model experiments and the model settings in the case study.

Lastly, our results are presented in Sect. 5 and discussed in Sect. 6.

2 Modelling framework and snowpack algorithm

In the following section we provide descriptions of the hydrologic model (Sect. 2.1) and the formulation of a novel snowpack module used for the analyses (Sect. 2.2).

2.1 Hydrologic model framework

For the analysis, we use Statkraft's hydrologic forecasting toolbox (Shyft; https://github.com/statkraft/shyft), a model framework developed for hydropower forecasting (Burkhart et al., 2016; Ghimirey, 2016; Westergren, 2016). Shyft provides the implementation of many well-known hydrological routines (conceptual parameter models, and more physically based approaches), and allows for distributed hydrological modelling. Standard model input variables are temperature, precipitation, wind speed, relative humidity, and shortwave radiation.

The methods used to simulate hydrological processes are (i) a single-equation implementation to determine the potential evapotranspiration, (ii) a newly developed snowpack algorithm using an online radiative transfer solution for snow to account for the effect of LAISI on the snow albedo, and (iii) a first-order nonlinear differential equation to calculate the catchment response to precipitation, snowmelt, and evapotranspiration. (i) and (iii) are described in more detail herein, while (ii) is described in detail in Sect. 2.2.

To determine the potential evapotranspiration, E_{pot}, we use the method according to Priestley and Taylor (1972):

$$E_{\mathrm{pot}} = \frac{a}{\lambda} \cdot \frac{s(T_{\mathrm{a}})}{s(T_{\mathrm{a}}) + \gamma} \cdot K_{\mathrm{n}}, \tag{1}$$

with $a = 1.26$ being a dimensionless empirical multiplier, γ the psychrometric constant, $s(T_{\mathrm{a}})$ the slope of the relationship between the saturation vapour pressure and the temperature T_{a}, λ the latent heat of vaporization, and K_{n} the net radiation.

The catchment response to precipitation and snowmelt is determined using the approach of Kirchner (2009), who describes catchment discharge from a simple first-order nonlinear differential equation. Following Kirchner (2009), we solve the log-transformed formulation

$$\frac{\mathrm{d}(\ln(Q))}{\mathrm{d}t} = g(Q)\left(\frac{P-E}{Q} - 1\right) \tag{2}$$

due to numerical instabilities of the original formulation. In Eq. (2), Q is the catchment discharge, E the evapotranspiration, and P the precipitation.

We assume that the sensitivity function, $g(Q)$, has the same form as described in Kirchner (2009):

$$\ln(g(Q)) \approx c_1 + c_2 \ln(Q) + c_3 (\ln(Q))^2, \tag{3}$$

with c_1, c_2, and c_3 being the only catchment-specific parameters, which we estimate by standard model calibration of simulated discharge against observed discharge. In contrast to Kirchner (2009)'s approach, we use the liquid water response from the snow routine instead of precipitation P in Eq. (2) (Kirchner, 2009, used snow-free catchments). The response from the snow routine can be liquid precipitation, meltwater, or a combination of both.

2.2 A new snowpack module for LAISI

To account for snow in the model, we developed a snow algorithm to solve the energy balance:

$$\frac{\delta F}{\delta t} = K_{\mathrm{in}}(1-\alpha) + L_{\mathrm{in}} + L_{\mathrm{out}} + H_{\mathrm{s}} + H_{\mathrm{l}} + R, \tag{4}$$

with the incoming shortwave radiation flux K_{in}, the incoming and outgoing longwave radiation fluxes L_{in} and L_{out}, the sensible and latent heat fluxes H_{s} and H_{l}, and the heat contribution from rain R. $\frac{\delta F}{\delta t}$ is the net energy flux into or out of the snowpack. Fluxes are considered to be positive when directed into the snowpack and as such an energy source.

L_{in} and L_{out} are calculated using the Stephan–Boltzmann law, with L_{in} depending on the air temperature T_{a} and L_{out} on the snow surface temperature T_{ss}, calculated as $T_{\mathrm{ss}} = 1.16 \cdot T_{\mathrm{a}} - 2.09$ (Hegdahl et al., 2016). The latent and sensible heat fluxes are calculated using a bulk-transfer approach that depends on wind speed, temperature, and relative humidity (Hegdahl et al., 2016).

The main addition provided in the algorithm described herein is the implementation of a radiative transfer solution for the dynamical calculation of snow albedo, α. This implementation allows a new class of model input variable, wet and dry deposition rates of light absorbing aerosols. From this, the model is able to simulate the impact of dust, black carbon, volcanic ash, or other aerosol deposition on snow albedo, snowmelt, and runoff. To account for the mass balance of LAISI, while maintaining a representation of sub-grid snow variability and snow cover fraction (SCF), a tiling approach is applied, where a grid cell's snowfall is apportioned to sub-grid units. Energy balance calculations are then conducted within each tile. Currently, a gamma distribution is used to distribute snowfall to the tiles.

Below, we introduce the radiative transfer calculations required to represent LAISI (Sect. 2.2.1), and provide further details of the sub-grid-scale tiling approach to represent snowpack spatial variability (Sect. 2.2.2).

2.2.1 Aerosols in the snowpack

Wiscombe and Warren (1980) and Warren and Wiscombe (1980) developed a robust and elegant model for snow albedo that remains today as a standard. Critical to their approach was the ability to account for (i) wide variability in ice absorption with wavelength, (ii) the forward scattering of snow

grains, and (iii) both diffuse and direct beam radiation at the surface. Furthermore, and of particular importance to the success of the approach, the model relies on observable parameters.

Both the albedo of clean snow and the effect of LAISI on the snow albedo strongly depend on the snow optical grain radius r (Warren and Wiscombe, 1980), which alters as snow ages. r can be related to the snow-specific surface area A_s via

$$r = \frac{3}{\rho_{ice} \cdot A_s}, \tag{5}$$

with ρ_{ice} the density of ice. A_s represents the ratio of surface area per unit mass of snow grain (Roy et al., 2013).

In our model, we compute the evolution of A_s in dry snow following Taillandier et al. (2007) as

$$\begin{aligned} A_s(t) = {} & [0.629 \cdot A_{s,0} - 15.0 \cdot (T_s - 11.2)] - [0.076 \cdot A_{s,0} \\ & -1.76 \cdot (T_s - 2.96)] \\ & \ln\left\{t + \exp\left(\frac{-0.371 \cdot A_{s,0} - 15.0 \cdot (T_s - 11.2)}{0.076 \cdot A_{s,0} - 1.76 \cdot (T_s - 2.96)}\right)\right\}, \end{aligned} \tag{6}$$

where t is the age of the snow layer (hours), $A_{s,0}$ is A_s at $t = 0$ ($cm^2\,g^{-1}$), and T_s is the snow temperature (°C). The evolution of A_s in wet snow is calculated according to Eq. (5) and Brun (1989) as

$$\frac{dr}{dt} = \frac{C_1 + C_2 \cdot \Theta^3}{r^2 \cdot 4\pi}, \tag{7}$$

where $C_1 = 1.1 \times 10^{-3}\,mm^3\,d^{-1}$ and $C_2 = 3.7 \times 10^{-5}\,mm^3\,d^{-1}$ are empirical coefficients. Θ is the liquid water content of snow in mass percentage. $A_{s,0}$ is set to $73.0\,m^2\,kg^{-1}$ (Domine et al., 2007) and we set the minimum snowfall required to reset A_s to 5 mm snow water equivalent (SWE).

To solve for the effect of light absorption from LAISI on the snow albedo, we have integrated a two-layer adaption of the Snow, Ice, and Aerosol Radiative (SNICAR) model (Flanner et al., 2007, 2009) into the energy and mass budget calculations. By providing the solar zenith angle of the sun, the snow optical grain radius r, mixing ratios of LAISI in the snow layers, and the SWE of each layer, SNICAR calculates the snow albedo for a number of spectral bands. To achieve this, SNICAR utilizes the theory from Wiscombe and Warren (1980) and the two-stream, multilayer radiative approximation of Toon et al. (1989). Following Flanner et al. (2007), our implementation of SNICAR uses five spectral bands (0.3–0.7, 0.7–1.0, 1.0–1.2, 1.2–1.5, and 1.5–5.0 µm) in order to maintain computational efficiency. Flanner et al. (2007) compared results from the 5-band scheme to the default 470-band scheme in SNICAR and concluded that relative errors are less than 0.5 %. The incident fluxes were simulated offline assuming mid-latitude winter clear- and cloudy-sky conditions.

The absorbing effect of LAISI is most efficient when the LAISI reside at or close to the snow surface (Warren and Wiscombe, 1980). As snow melts, LAISI can remain near the surface due to inefficient melt scavenging, which leads to an increase in the near-surface concentration of LAISI and thus a further decrease in the snow albedo – the so-called melt amplification (e.g. Xu et al., 2012; Doherty et al., 2013, 2016; Sterle et al., 2013). Field observations suggest that the magnitude of this effect is determined by the particle size and the hydrophobicity of the respective LAISI (Doherty et al., 2013). Conway et al. (1996) observed vertical redistribution and the effect on the snow albedo by adding volcanic ash and hydrophilic and hydrophobic BC to the snow surface of a natural snowpack. Flanner et al. (2007) used the results from Conway et al. (1996) to determine the scavenging ratios, specifying the ratio of LAISI contained in the melting snow that is flushed out with meltwater, of both hydrophilic and hydrophobic BC. They found the scavenging ratio for hydrophobic BC, k_{phob}, to be 0.03, and, for hydrophilic BC, k_{phil}, 0.2. Doherty et al. (2013) found similar results by observing BC mixing ratios close to the surface of melting snow. However, more recent studies report efficient removal of BC with meltwater (Lazarcik et al., 2017), revealing large gaps in the understanding of the process.

To represent the evolution of LAISI mixing ratios near the snow surface, we treat LAISI in two layers in our model. The surface layer has a time-invariant maximum thickness (further called the maximum surface layer thickness). The mixing ratio of each LAISI species in this layer is calculated from a uniform mixing of the layer's snow with either falling snow with a certain mixing ratio of aerosol (wet deposition) or aerosol from atmospheric dry deposition. The second layer (bottom layer) represents the snow exceeding the maximum thickness of the surface layer. Following Krinner et al. (2006), we apply a maximum surface layer thickness of 8 mm SWE. Krinner et al. (2006) suggest this value is based on observations of 1 cm thick dirty layers in alpine firn cores used to identify summer horizons. Due to potential accumulation of LAISI in surface snow via dry deposition and melt amplification, we expect the simulated surface mixing ratios of LAISI to be sensitive to the maximum surface layer thickness of our model. For this reason, we use a factor of 2 for the maximal surface layer thickness to account for the uncertainty of this model parameter.

To allow for melt amplification in the model, we include LAISI mass fluxes between the two layers during snow accumulation and snowmelt. Generalizing Jacobson (2004)'s representation of LAISI mass loss due to meltwater scavenging for multiple snow layers, we characterize the magnitude of melt scavenging using the scavenging ratio k and calculate the temporal change in LAISI mass m_s in the surface layer as

$$\frac{dm_s}{dt} = -k q_s c_s + D, \tag{8}$$

and the change in LAISI mass m_b in the bottom layer as

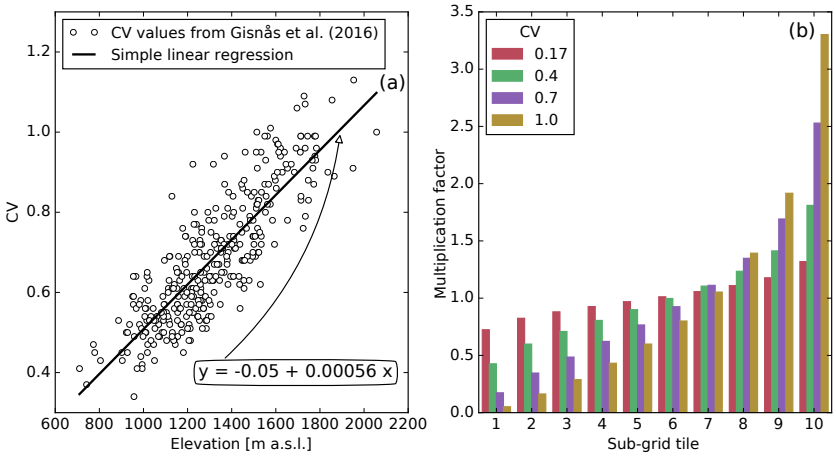

Figure 1. (a) Elevation versus coefficients of variation (CVs) of sub-grid snow distribution from Gisnås et al. (2016) of forest-free areas in the Atnsjoen catchment (dots) and the relationship between the CVs and the elevation resulting from simple linear regression analysis (black line). **(b)** Solid precipitation multiplication factors for the sub-grid snow tiles for different CVs.

$$\frac{\mathrm{d}m_\mathrm{b}}{\mathrm{d}t} = k(q_\mathrm{s}c_\mathrm{s} - q_\mathrm{b}c_\mathrm{b}). \tag{9}$$

Herein, q_s and q_b are the mass fluxes of meltwater from the surface to the bottom layer and out of the bottom layer, respectively, and c_s and c_b are the mass mixing ratios of LAISI in the respective layer. D is the atmospheric deposition mass flux. A value for k of < 1 is equal to a scavenging efficiency of less than 100 % and hence allows for accumulation of LAISI in the surface layer during melt. In our analysis, we account for hydrophobic and hydrophilic BC. By following Flanner et al. (2007), we set k_phob to 0.03 and k_phil to 0.2, and account for the large uncertainty in those estimates by using an order of magnitude variation on k_phob and k_phil. Like Flanner et al. (2007), we treat aged, hydrophilic BC as sulfate coated to account for the net increase in the mass absorption cross section (MAC) by 1.5 at $\lambda = 550$ nm compared to hydrophobic BC caused by the ageing of BC (reducing effect on MAC) and particle coating from condensation of weakly absorbing compounds (enhancing effect on MAC) suggested by Bond et al. (2006). As a consequence, hydrophilic BC absorbs more strongly than hydrophobic BC under the same conditions. On the other hand, hydrophilic BC undergoes a more efficient melt scavenging. The competing mechanisms are subjects of the 1-D sensitivity study in Sect. 5.1.3.

2.2.2 Sub-grid variability in snow depth and snow cover

In order to allow for explicit treatment of snow layers while representing sub-grid snow variability, we follow Aas et al. (2017), and assume that the sub-grid spatial distribution of each single event of solid precipitation follows a certain probability distribution function. From this distribution we calculate multiplication factors, which then are used to assign the snowfall of a model grid cell to a number of sub-grid computational elements, the so-called tiles (Aas et al., 2017). The snow algorithm described herein is executed for each of the tiles separately, providing a mechanism to account for snow spatial distribution while preserving conservation of mass. Therefore, variables related to the snow state, such as SWE, liquid water content, LAISI mixing ratios, and snow albedo differ among the tiles. To calculate the multiplication factors, we assume that the sub-grid redistributed snow follows a gamma distribution (see e.g. Kolberg and Gottschalk, 2010; Gisnås et al., 2016), determined by the coefficient of variation (CV) of SWE at snow maximum. Gisnås et al. (2016) used Winstral and Marks (2002)'s terrain-based parametrization to model snow redistribution in Norway by accounting for wind effects during the snow accumulation period over a digital elevation model with 10 m resolution. In the case study presented in Sect. 5.2, we use the CV values from Gisnås et al. (2016) to derive a linear relationship between the model grid cell's elevation and the corresponding CV value by simple linear regression (see Fig. 1a), which results in a R^2 value of 0.71 and a p value of smaller than 2.0×10^{-5} for the study area. The linear relationship is only applied to grid cells with an areal forest cover fraction of lower than or equal to 0.5. For grid cells with a forest cover fraction of higher than 0.5, a constant snow CV value of 0.17 is used, following the findings of Liston (2004) for high-latitude, mountainous forest. Examples of multiplication factors for forested grid cells and forest-free grid cells for different CV values are shown in Fig. 1b.

3 Site description, meteorologic model input, and atmospheric deposition data

We selected the unregulated upper Atna catchment for our analysis. The catchment is located in a high-elevation region of southern Norway (Fig. 2). The watershed covers an area of 463 km^2 and ranges in elevation from 700 m a.s.l. at the outlet at lake Atnsjoen to over 2000 m a.s.l. in the Rondane mountains in the western part of the watershed, with approximately 90 % of the area above the forest limit. The average annual precipitation in the watershed during the study period is approximately 655 mm. The mean annual discharge is approximately 11 m^3 s^{-1}, with low flows of 1–3 m^3 s^{-1} during the winter months and peak flows of over 130 m^3 s^{-1} during the spring melt season.

For the meteorological model input of precipitation, temperature, relative humidity, and wind speed we use daily observations from the Norwegian Water Resources and Energy Directorate (NVE) and the Norwegian Meteorological Institute (MET). Four meteorological stations are located in the watershed at elevations between 701 and 780 m a.s.l. along the Atna river, two of these measuring precipitation and two measuring temperature. Observations of relative humidity and wind speed originate from two stations at locations close by the catchment (not shown in Fig. 2). Further information about the stations are given in Table 1. Due to poor availability of continuous solar radiation observations in Norway, we use gridded global radiation data from the Water and Global Change (WATCH) Forcing Data methodology applied to ERA-Interim reanalysis data (WFDEI; Weedon et al., 2014) with a resolution of 0.5°. Discharge observations are from a station located at the outlet of the catchment at lake Atnsjoen and are used for model calibration and validation. In the following, we present the development of atmospheric deposition rates of BC, which we use as a proxy for LAISI, due to a lack of available deposition rates for other species. For the 1-D sensitivity study of Sect. 5.1 we developed representative model input based on the meteorological conditions in this catchment.

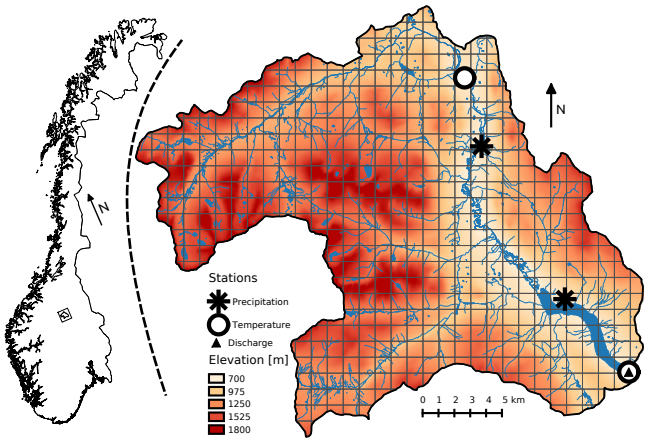

Figure 2. Location of the Atnsjoen catchment in Norway (black box in the left map) and overview map of the Atnsjoen catchment (right).

Atmospheric deposition of black carbon from the REMO-HAM model

The wet and dry deposition rates of BC for the study area are generated using the REMO-HAM regional aerosol-climate model (Pietikäinen et al., 2012). The core of the model is a hydrostatic, 3-D atmosphere model developed at the Max Planck Institute for Meteorology in Hamburg. With the aerosol configuration, the model incorporates the HAM (Hamburg Aerosol Module) by Stier et al. (2005) and Zhang et al. (2012). HAM calculates the aerosol distributions using seven log-normal modes and includes all the main aerosol processes.

For the simulations, we follow the approach of Hienola et al. (2013), but with changes to the emission inventory: Hienola et al. (2013) used emissions based on the AeroCom emission inventory for the year 2000 (see Dentener et al., 2006). In the REMO-HAM simulations conducted herein, emissions are made by the International Institute for Applied Systems Analysis (IIASA) and are based on the Evaluating the Climate and Air Quality Impacts of Short-Lived Pollutants (ECLIPSE) V5a inventory for the years 2005, 2010, and 2015 (years in between were linearly interpolated) (Klimont et al., 2016, 2017). We also updated other emissions modules (wildfire, aviation, and shipping) following the approaches presented in Pietikäinen et al. (2015). The only difference to Pietikäinen et al. (2015) in this work is that we used the Global Fire Emissions Database (GFED) version 4 based on an updated version of van der Werf et al. (2010).

REMO-HAM was used for the same European domain as in Pietikäinen et al. (2012) using a 0.44° spatial resolution (50 km), 27 vertical levels, and a 3 min time step. The ERA-Interim re-analysis data were utilized at the lateral boundaries for meteorological forcing (Dee et al., 2011) and, for the lateral aerosol forcing, data from the ECHAM-HAMMOZ global aerosol-climate model (version echam6.1.0-ham2.2) were used. ECHAM-HAMMOZ was simulated in a nudging mode, i.e. the model's meteorology was forced to follow ERA-Interim data, and the ECLIPSE emissions were used (plus the other updated emission modules shown in Pietikäinen et al., 2015). The boundaries of REMO-HAM were updated every 6 h for both meteorological and aerosol related variables. Simulations with REMO-HAM were conducted for the time period of 1 July 2004–31 August 2012 and the time period used in our analysis is from 1 September 2006 onwards. The initial state for the model was taken from the boundary data, except for the soil parameters, which were taken from a previous long-term simulation for the same domain (a so-called warm start). The output frequency of REMO-HAM was 3 h and the total BC deposition flux was

Table 1. Information about observational stations.

Station name	Station ID	Operator	Observational variable	Elevation (m a.s.l.)
Atnsjoen 1	8720	MET	precipitation	749
Atndalen-Eriksrud	8770	MET	precipitation	731
Atnsjoen 2	2.32.0	NVE	temperature	701
Li Bru	2.479.0	NVE	temperature	780
Fokstuga	16610	MET	wind speed; relative humidity	973
Kvitfjell	13160	MET	wind speed	1030
Venabu	13420	MET	relative humidity	930

calculated from the accumulated dry and wet deposition and sedimentation fluxes, and resampled to daily time resolution. Herein, dry deposition refers to the sum of REMO-HAM dry deposition and sedimentation.

4 Modelling experiments and calibration

Our analysis is conducted in two parts. First, in a 1-D sensitivity study, we investigate the sensitivity of parameters and variables specific to the LAISI algorithm presented in Sect. 2.2. We then demonstrate the impact of BC at the catchment scale in a case study by simulating the impact of wet and dry deposition of BC on snowmelt and discharge generation in a remote southern Norwegian catchment (Sect. 5.2).

We assume uncertainties of the LAISI radiative forcing in snow to originate mainly from the model representation of surface layer thickness, melt scavenging of BC, and uncertainties in the deposition input data. To account for the uncertainties, we declare minimum (min), central (mid), and maximum (max) effect estimates for each of the critical parameters, outlined together with further model parameters in Table 2. The min, mid, and max estimates are both subjects of analysis in the sensitivity study (further described in Sect. 4.1) and used in the case study to give an uncertainty estimate of the LAISI effect on the hydrologic variables (further described in Sect. 4.2). We investigate the impact of BC impurities on the response variables by comparing the results from aerosol radiative forcing model experiments (ARF scenarios) to simulations in which all BC deposition rates are set to zero (no-ARF scenario).

4.1 One-dimensional sensitivity study experiments

The results of the 1-D sensitivity study are presented in Sect. 5.1; herein we describe the configurations to conduct our analysis. The purpose of this study is to isolate the impact of different model parameters: (i) maximum surface layer thickness (parameter *max_surface_layer*; see Table 2), (ii) scavenging ratio, and (iii) the impact of the scavenging ratio with respect to the BC species (parameters k_{phob} and k_{phil}).

Our approach evaluates these parameters and the evolution of the snowpack under constant melting conditions. We run the 1-D simulations with model parameters as outlined in Table 2 and forcing data based on synthetic input data. The synthetic forcing data set is based on the average meteorological conditions during the melt season from mid March until mid July of the Atnsjoen catchment. In our sensitivity experiments, all snowpacks have 250 mm SWE of snow with a mixing ratio of 35 ng g^{-1} in both surface and bottom layer at melt onset. These values are representative of the upper 50 % of tiles at winter snow maximum in the Atnsjoen catchment during the study period of the case study. During the melt period, we exclude fresh snowfall and dry deposition, in order to isolate the effect of the tested model parameters on the snowpack evolution under melt conditions. This may lead to an underestimation of total BC mass in the snow column.

To investigate the impact of the maximum surface layer thickness (parameter *max_surface_layer*) of the model, we run simulations with synthetic forcing and use maximal surface layer thicknesses of 4.0 mm SWE (max estimate; see Table 2), 8.0 mm SWE (mid estimate), and 16.0 mm SWE (min estimate). Additionally, we include a single-layer model with a vertically uniform distribution of BC in the analysis and, for comparison, a simulation with clean snow.

To explore the sensitivity to scavenging ratio, we apply different BC scavenging ratios in the range of the uncertainty of hydrophilic BC, which covers a wide range from very efficient to inefficient scavenging. The scavenging ratios applied are based on the analysis conducted by Flanner et al. (2007) using data from Conway et al. (1996). The mid estimate for the hydrophilic BC scavenging ratio ($k_{\mathrm{phil}} = 0.2$) also compares well to field observations from Doherty et al. (2013). We further include in the analysis Flanner et al. (2007)'s upper bound uncertainty estimate for hydrophilic BC (2.0; efficient scavenging), the lower bound estimate (0.02; inefficient scavenging), and for comparison a scenario in which BC does not undergo any scavenging (0.0).

Hydrophilic BC absorbs more strongly than hydrophobic BC under the same conditions due to an increased MAC for hydrophilic BC resulting from ageing of the aerosol during atmospheric transport (Bond et al., 2006). On the other hand, hydrophilic BC undergoes more efficient melt scavenging (Flanner et al., 2007), which impacts the snowpack evolution significantly. To explore this competing interplay, we apply the mid estimate of the scavenging ratio of hydropho-

Table 2. Model parameters used in the sensitivity and case study. Parameters optimized during calibration are marked with [a]. Further parameters were pre-set and not included in parameter estimation during calibration. Parameters with different values in the minimum (min), central (mid), and maximum (max) BC radiative forcing estimates are marked with [b].

Parameter	Description and unit	min estimate	optimized/set mid estimate	max estimate
c_1[a]	empirical coefficient 1 (see Eq. 3) (–)		−4.298	
c_2[a]	empirical coefficient 2 (see Eq. 3) (–)		0.3295	
c_3[a]	empirical coefficient 3 (see Eq. 3) (–)		−0.07757	
ae_scale_factor[a]	scaling factor for actual evapotranspiration (–)		1.43	
tx[a]	temperature threshold rain/snow (°C)		−0.92	
wind_const[a]	determining wind profile (–)		6.32	
wind_scale[a]	determining wind profile (–)		1.12	
snowfall_reset_depth	minimum snowfall required to reset A_s (mm SWE)		5.0	
snow_cv_forest	snow CV in forested area (–)		0.17	
snow_cv_intercept	intercept of linear elevation–CV relation (–)		−0.05	
snow_cv_slope	slope of linear elevation–CV relation (m^{-1})		0.00056	
max_water	fractional max water content of snow (–)		0.10	
$A_{s,0}$	A_s of fresh snowfall ($m^2\,kg^{-1}$)		73.0	
surface_magnitude	maximum snow depth for snow heat content (mm SWE)		30.0	
max_surface_layer[b]	maximum thickness of surface layer (mm SWE)	16.0	8.0	4.0
depo_factor[b]	multiplication factor for deposition (–)	0.5	1.0	1.5
k_{phob}[b]	scavenging ratio of hydrophobic BC (–)	0.3	0.03	0.003
k_{phil}[b]	scavenging ratio of hydrophilic BC (–)	2.0	0.2	0.02

bic BC ($k_{phob} = 0.03$) to both the hydrophobic BC and the hydrophilic BC species. In this manner we explore the isolated effect of the different absorption properties of the two species. We further apply the mid estimate for hydrophilic BC scavenging ratio ($k_{phil} = 0.2$) to hydrophilic BC to quantify the gross effect. As in other cases, we include the no-ARF scenario to highlight the overall effect on the albedo and melt of the different scenarios.

4.2 Case study model set-up and calibration

We investigate the impact of BC aerosol deposition on the catchment hydrology of a Norwegian catchment over a study period of 6 years, from September 2006 to August 2012. The station-based input data described above (Sect. 3) are interpolated to the simulation grid cells ($1 \times 1\,km^2$ and accordingly smaller cells at the catchment boarders; see Fig. 2) using Shyft's interpolation algorithms. For temperature Bayesian Kriging (Diggle and Ribeiro, 2007) is used. For precipitation, BC deposition rates, wind speed, and relative humidity interpolation to the model grid cells are via inverse distance weighting. A 5 % increase in precipitation for every 100 m increase in altitude is used for the precipitation interpolation (Førland, 1979).

To calibrate the model against observed discharge, we first run a split-sample calibration (Klemes, 1986) using the first 3 years (1 September 2006 to 31 August 2009) of the study period as the calibration period and the following 3 years (1 September 2009 to 31 August 2012) for model validation. For parameter estimation, we use the BOBYQA algorithm for bound-constrained optimization (Powell, 2009). To assess the predictive efficiency of the model, we use the Nash–Sutcliffe model efficiency

$$E_{NS} = 1 - \frac{\sum_{t=0}^{T}(Q_o^t - Q_s^t)^2}{\sum_{t=0}^{T}(Q_o^t - \overline{Q_o})^2}, \quad (10)$$

where Q_o^t and Q_s^t are the observed and simulated discharge at time t, respectively, and $\overline{Q_o}$ is the mean observed discharge over the assessed period.

Model calibration is run with mid estimates for all model parameters impacting the handling and effect of LAISI and aerosol depositions as simulated from REMO-HAM during model calibration. Those parameters and further model parameters, including the parameters estimated during calibration, are listed in the left column of Table 2. We investigate the uncertainty in the effect of BC on snowmelt by using the min and max effect parameter estimates from Table 2, while holding constant all other model parameters as estimated during calibration. To assess the gross effect of LAISI, we compare the simulations to equivalent simulations in which ARF is not included.

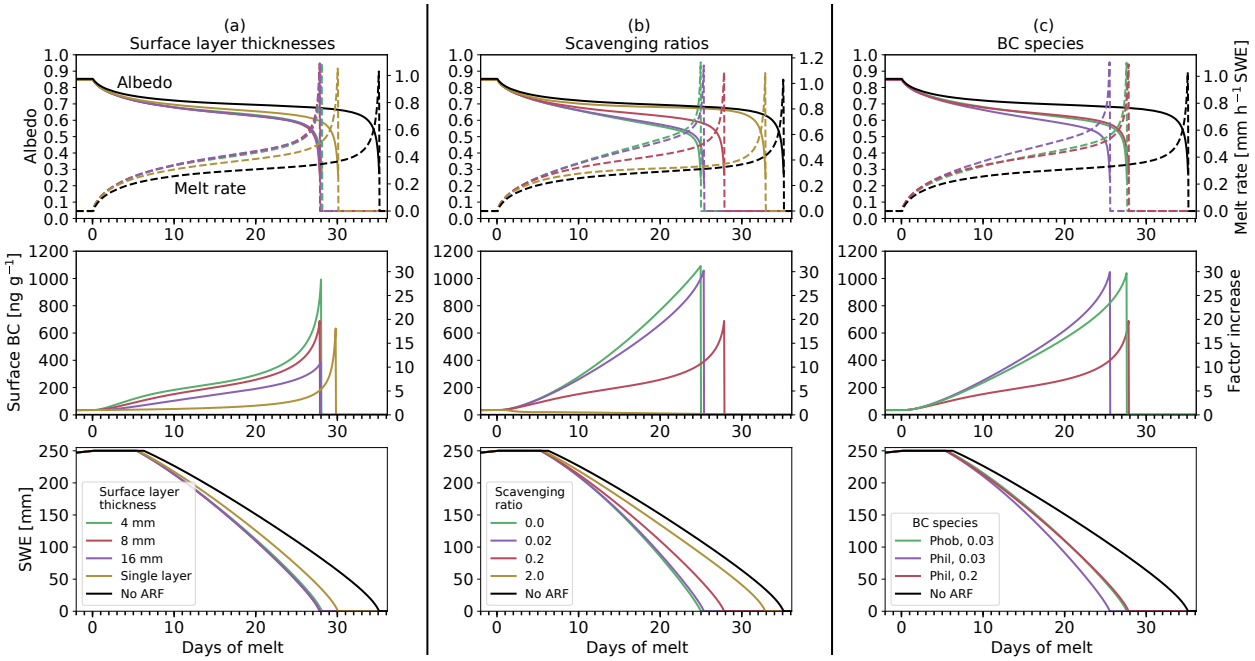

Figure 3. Snow albedo (top row of graphs; solid lines) and melt rate (top row of graphs; dashed lines), BC mixing ratio in the surface layer and factor increase in the mixing ratio during melt compared to the pre-melt BC mixing ratio (central row of graphs), and snowpack SWE (bottom row of graphs) for simulations forced with synthetic data based on average meteorological conditions during the melt season from mid March until mid July of the Atnsjoen catchment and different model configurations: **(a)** different values for maximum surface layer thickness; **(b)** scavenging ratio; and **(c)** BC species with different melt scavenging ratios applied (*phob* and *phil* in the legend stand for hydrophobic and hydrophilic BC, respectively). The black lines in all graphs show simulation results of model runs without ARF applied (no-ARF).

5 Results

5.1 One-dimensional sensitivity studies

5.1.1 Sensitivity to surface layer thickness

Figure 3a shows the effect of the different maximum surface layer thicknesses (parameter *max_surface_layer*) on the melting snowpack with other parameters set according to Table 2. The maximum surface layer thickness strongly determines the surface BC mixing ratio over the melt season. During snowmelt, surface BC increases up to a factor of circa 10, 20, and 30 for maximum surface layer thicknesses of 16.0, 8.0, and 4.0 mm SWE, compared to the pre-melt season BC mixing ratio (35 ng g^{-1}). For those three two-layer scenarios (purple, red, and green curves in Fig. 3a), the resulting differences in albedo and melt rate are small, even though the increase in the surface layer mixing ratio during the melt season differs strongly among the scenarios. Using the single layer model, the surface BC mixing ratio increases more slowly and stays comparably low in contrast to the two-layer models until shortly before meltout. This leads to a less pronounced decrease in albedo compared to the two-layer models and thus to a shorter meltout shift compared to a clean snowpack of about 5 days (yellow curves in Fig. 3a), whereas the two-layer scenarios show earlier meltouts of about 7 days.

5.1.2 Sensitivity to scavenging ratio of BC

In the range of investigated scavenging ratios, we find the sensitivity of the surface BC mixing ratio, the albedo, and the subsequent snowmelt to this parameter (Fig. 3b). When applying a melt scavenging factor typical for the lower bound of hydrophilic BC (0.02, purple lines) there is little effect compared to the scenario without melt scavenging (green lines). Both show circa a factor 30 increase in surface BC mixing ratio to the end of the melt season and only little differences in the development of albedo and snowmelt. Similar results are achieved when using the mid estimate scavenging factor for hydrophobic BC (0.03, not shown). A distinction exists when using the mid estimate scavenging factor for hydrophilic BC (0.2, red line). In contrast to no scavenging and the lower bound hydrophilic scavenging, surface BC does not increase as rapidly during the melt period and is completely flushed when applying a melt scavenging factor typical for the upper bound of hydrophilic BC (yellow line; the surface concentration drops continuously during the melt period).

The changes in the scavenging ratio lead to a considerable effect on albedo and snowmelt. Meltout is delayed by circa

0.5 (purple lines), 3 (red lines), and 8 days (yellow lines) for scavenging ratios of 0.02, 0.2, and 2.0, respectively, compared to no scavenging (green lines). Compared to the no-ARF experiment (black lines), our simulations show that the presence of BC causes an earlier meltout of about 9.5, 7, and 2 days for scavenging ratios of 0.02, 0.2, and 2.0, respectively.

5.1.3 Sensitivity to BC species

The column of graphs in Fig. 3c illustrate the net effect of the competing processes of more efficient absorption resulting from a larger MAC with more efficient wash out. A mid estimate of the scavenging ratio of hydrophobic BC (0.03) is applied and shown for the hydrophobic BC (green curve) and the hydrophilic BC (purple curves) species. These curves show the isolated effect of the different absorption properties of the two species. Further, the mid estimate scavenging ratio for hydrophilic BC (0.2) is also shown using radiative properties of hydrophilic BC to quantify the gross effect (red curves). The no-ARF scenario (black curves) highlights the overall impacts.

The isolated effect of the stronger absorption of hydrophilic BC leads to an earlier meltout by circa 2 days compared to hydrophobic BC (purple and green curves in graphs of Fig. 3c). However, when applying the mid estimate of the scavenging ratio for hydrophilic BC (0.2), the combined effects leads to a masking of the isolated effect of stronger absorption by hydrophilic BC (and vice versa). During the melt period, snow albedo, melt rate and the snowpack SWE barely differ between the scenarios with the mid estimate scavenging for hydrophobic and hydrophilic BC applied (green and red curves). This reveals that both scenarios, hydrophobic BC with low scavenging efficiency and hydrophilic BC with high scavenging efficiency, lead to an earlier meltout by roughly 7 days compared to the no-ARF scenario.

5.2 Case study: Impact of BC deposition on the hydrology of a south Norwegian catchment

5.2.1 Performance of the model

In the split-sample test, the model performance is acceptable during both calibration and validation, with Nash–Sutcliffe model efficiencies of 0.86 during the calibration period (green line in Fig. 4a) and 0.82 during the validation period (red line in Fig. 4a). However, in the winter season (November until March) the model generally underestimates the discharge and peaks in the beginning of the melt season are slightly underestimated. The scatter plot in Fig. 5 confirms the underestimation of low-flow situations. For the different scenarios explored within the case study, all LAISI-relevant parameters are fixed to mid estimates and model parameters optimized for the full period (1 September 2006 to 31 August 2012; Fig. 4b) resulting in a Nash–Sutcliffe model

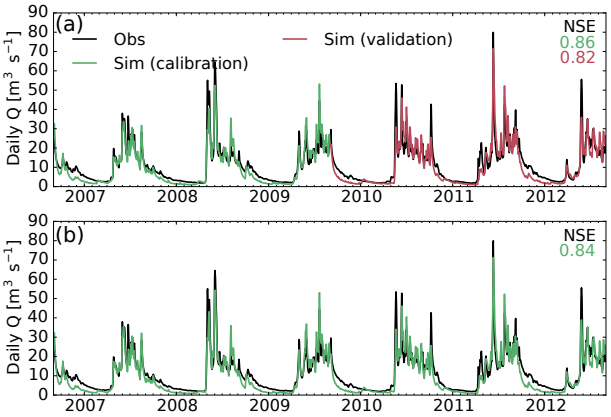

Figure 4. Simulated (green and red curves) and observed (black curve) daily discharge from the Atnsjoen catchment. **(a)** is showing the simulation results for 3 years of calibration (green) and 3 years of validation (red). **(b)** is showing the results for the 6-year calibration period. Parameters estimated in the latter are used in the case study. Parameters not included in the optimization are set to mid estimate values during the calibration process (see Table 2).

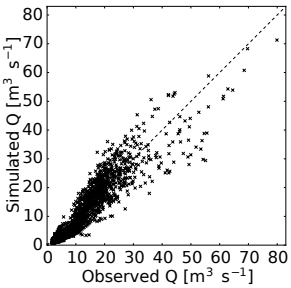

Figure 5. Comparison of observed and simulated daily discharge Q of the Atnsjoen catchment. The dashed black line demonstrates perfect agreement between simulation and observation.

efficiency of 0.84. The optimized parameters are listed in Table 2. Note that switching ARF off entirely (no BC deposition) leads to a slight decrease in the model quality (Nash–Sutcliffe model efficiency of 0.83 over the whole period; not shown).

5.2.2 Surface BC and albedo

For the min and mid estimate, the model simulates an average annual surface BC mixing ratio of about 18 and 71 ng g^{-1}, respectively. Our max estimate yields 198 ng g^{-1}. The evolution of surface albedo driven by BC deposition is distinct in the accumulation period vs. the melt period. During the snow accumulation period (until end of March), only slight differences in albedo are noticeable. The average annual snow albedo from 1 January until 22 March is 0.871 for the no-ARF scenario (Fig. 6a), while during the same time period, min, mid, and max estimates show relative albedo reductions of 0.003, 0.010, and 0.014, respectively from the no-ARF

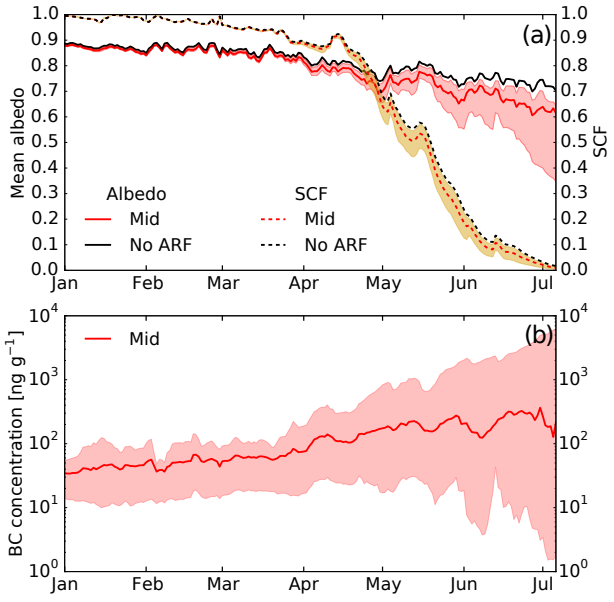

Figure 6. (a) Simulated mean catchment snow albedo (solid lines) and snow-covered fraction (SCF; dashed lines) for the mid (red lines), min, and max (shaded) estimates and for the scenario without ARF (no-ARF; black lines) averaged over the 6-year period. **(b)** Mixing ratio of BC in the model surface layer for the mid (solid line), min (lower bound of the shaded area), and max (upper bound of the shaded area) estimates.

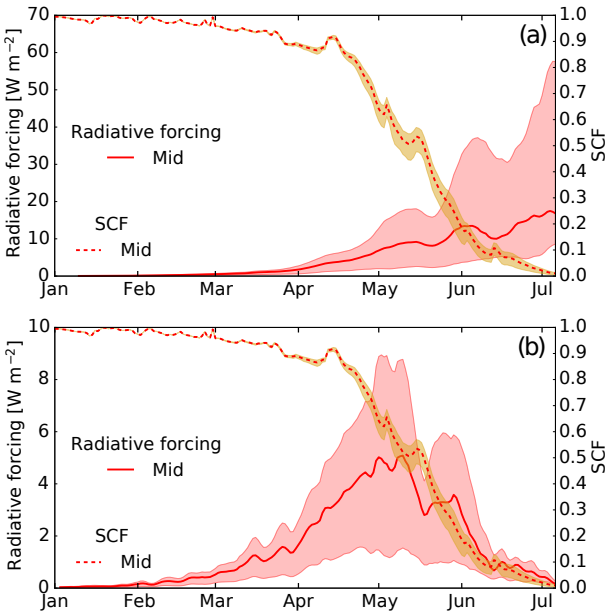

Figure 7. Catchment snow-covered fraction (SCF; dashed lines), **(a)** simulated mean radiative forcing in snow (RFS), and **(b)** total daily energy uptake in the catchment due to BC (surface radiative forcing in Watts per square metre catchment area) for the mid (solid red lines), min (lower bound of the shaded area), and max (upper bound of the shaded area) estimates averaged over the 6-year period).

case. At the beginning of the melt period, surface layer concentrations of min, mid, and max estimate average to 12, 49, and 98 ng g^{-1} (Fig. 6b).

With the start of the melt season, the difference in albedo between model experiments becomes increasingly larger over time. During the melt season, the mid estimate spatially averaged surface BC mixing ratio increases from 49 to about 250 ng g^{-1} (factor 5 increase) at the end of the melt season (beginning of July). For the max estimate, the increase is from roughly 100 to over 2500 ng g^{-1} (factor 25 increase). The min estimate on the other hand leads to a decrease in the BC surface mixing ratio. The distinctly different surface BC mixing ratios at the end of the melt season and among the three scenarios cause large differences in albedo decrease relative to the no-ARF case of about 0.03, 0.1, and over 0.3 for the min, mid, and max estimates, respectively.

5.2.3 BC-induced radiative forcing

The radiative forcing in snow (RFS) induced by the presence of BC is calculated from the average radiative forcing over snow-bearing tiles only. The RFS represents the additional uptake of energy from solar radiation per area snow cover due to the presence of BC in the snow compared to clean snow with the same properties. Figure 7a shows the daily mean RFS and demonstrates the increase in RFS during snowmelt. Low RFS is observed during the snow accumulation period, then steadily increasing through spring snowmelt, reaching values of approximately 8, 18, and 57 W m^{-2} for the min, mid, and max estimates, respectively (see the red solid line and shaded area in Fig. 7a). RFS in mid winter is small due to low surface BC mixing ratios and low solar irradiance.

However, most relevant for discharge generation (see Sect. 5.2.4) is the catchment-wide total daily energy uptake due to BC, or surface radiative forcing, calculated as the mean radiative forcing over all grid cells. As the snow cover fraction (SCF) in the catchment drops during spring (dotted line and yellow shaded area in Figs. 6 and 7), the effect of the RFS on the melt generation is limited by the increasing area of bare ground. The net effect is shown in Fig. 7b. The catchment mean surface radiative forcing due to the presence of BC in snow shows a strong annual cycle and reaches a maximum of 1.3, 4.9, and 8.8 W m^{-2} (min, mid, and max estimates, respectively) around the beginning of May.

5.2.4 BC impact on catchment discharge and snow storage

Figure 8a shows the simulated daily discharge and catchment SWE averaged over the 6-year simulation period for the mid (red lines), min, and max estimates (bounds of the shaded areas), and the no-ARF scenario (black lines). The differences in daily discharge and catchment SWE of the min,

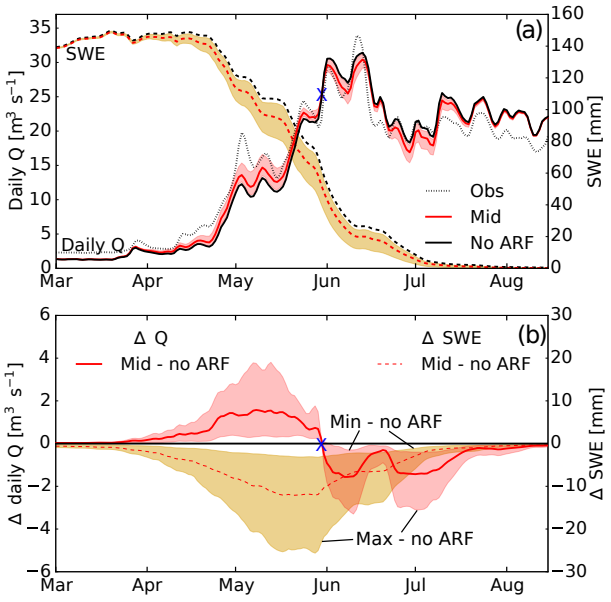

Figure 8. (a) Simulated daily discharge (Q; solid lines) and catchment mean snow water equivalent (SWE; dashed lines) for the mid (red lines), min, and max (shaded) estimates and for the scenario without ARF (no-ARF; black lines) averaged over the 6-year period. **(b)** Differences in daily discharge and SWE between ARF scenarios and the scenario without ARF (no-ARF). The blue marker in **(a)** and **(b)** separates the periods where BC in snow has an enhancing effect (left of the marker) and a decreasing (right of the marker) effect on discharge.

mid, and max estimates to the no-ARF scenario are shown in Fig. 8b. All simulations with ARF applied show higher daily discharge from the end of March until the end of May and lower discharge from the end of May until mid August relative to the no-ARF simulation. For the rest of the year, no effect on discharge is noticeable. The net impact of RFS results in a shift in the timing of discharge. Higher discharge early in the melt season is observed, yet offset by lower discharge following May. The cumulative annual discharge remains nearly identical.

Min, mid, and max estimates all show the change from higher to lower discharge compared to the no-ARF scenario approximately at the same time (at the end of May; see the blue marker in Fig. 8). Therefore, we can quantify the absolute and relative effect of RFS on the discharge during the two periods: the early melt season from circa 22 March until 29 May and the late melt season from circa 30 May until 10 August (Fig. 8b, and see Table 3). This yields an average percentage increase in daily discharge of 2.5, 9.9, and 21.4 % for the min, mid, and max estimates for the early melt season and a decrease in discharge of −0.8, −3.1, and −6.7 % during the late melt season.

The differences in discharge among the scenarios can be explained by understanding the evolution of the snowpack. In all scenarios the catchment SWE (Fig. 8a) reaches a peak reduction relative to the no-ARF scenario of −4.6, −13.4, and −34.4 % in mid May. The average decreases in catchment SWE of the min, mid, and max estimates compared to the no-ARF scenario during the entire melt season are −2.1, −7.4, and −15.1 % (see Table 3). From mid May on, the differences in catchment SWE between scenarios drop continuously, which is equivalent to a higher catchment averaged snowmelt rate in the no-ARF scenario compared to the ARF scenarios.

6 Discussion

The objective of this work is to provide a mechanism to assess the impact of light absorbing aerosols on runoff at the catchment scale in a rainfall–runoff modelling context. Prior investigations into LAISI indicate potentially significant impacts on the cryosphere (Flanner et al., 2007) with potential impacts on water resources (Qian et al., 2009, 2011). Earlier studies on hydrologic impacts at the catchment scale have used altered radiative forcings to evaluate the impact on the timing of snowmelt and hydrology (Painter et al., 2010; Skiles et al., 2012). With the approach presented herein, we seek to fill a gap between land-surface model approaches (e.g. Oaida et al., 2015) and approaches that apply modified radiative forcing to provide a novel tool for hydrologic forecasting.

6.1 Parameter sensitivity

To assess the sensitivity of the newly introduced algorithm and parameters, we conducted a sequence of 1-D sensitivity studies. In this context, we are able to remove complexities that arise when conducting distributed simulations at the catchment scale.

We found the greatest sensitivity to lie in the parametrization of scavenging, as it relates to how likely the aerosol is to remain at the snow surface during melt. Field measurements indicate that only a fraction of BC is flushed out with the meltwater and BC can accumulate near the snow surface (e.g. Xu et al., 2012; Doherty et al., 2013, 2016; Sterle et al., 2013). Our model is able to simulate this process by taking the scavenging ratio of BC during meltwater movement into account (Eqs. 8 and 9). In the literature, the scavenging efficiency of BC is discussed controversially. Flanner et al. (2007)'s estimates for scavenging ratios of hydrophilic and hydrophobic BC, which are used in this study, are based on data from field experiments using artificially added soot (Conway et al., 1996). However, parameters derived from artificially added soot might not be directly transferable to the scavenging properties of naturally occurring BC. Even though field observations from Doherty et al. (2013) agree well with the estimates of Flanner et al. (2007), and further studies highlight the importance of BC retention in the snowpack (e.g. Xu et al., 2012; Sterle et al., 2013), a large uncer-

Table 3. Average change in discharge during the early (22 March to 29 May) and late (30 May to 10 August) melt seasons of min, mid, and max estimates and average change in SWE during the melt season (22 March to 10 August) compared to the no-ARF scenario.

scenario	early melt season discharge		late melt season discharge		melt season SWE	
	($m^3\,s^{-1}$)	(%)	($m^3\,s^{-1}$)	(%)	(mm)	(%)
min estimate	0.2	2.5	−0.18	−0.8	−1.5	−2.1
mid estimate	0.81	9.9	−0.74	−3.1	−5.1	−7.4
max estimate	1.74	21.4	−1.60	−6.7	−10.3	−15.1

tainty remains on the magnitude of this effect (Lazarcik et al., 2017). These uncertainties are identified in our simulations as results show large differences in BC evolution and day of meltout at the boundaries of the applied scavenging ratios (Fig. 3b). Compared to the no-ARF experiment (black lines), the presence of BC causes an earlier meltout for all scavenging ratios applied, spanning from 2 days (upper boundary hydrophilic scavenging, 2.0) to about 9.5 days (lower boundary hydrophilic scavenging, 0.02). Even when applying efficient melt scavenging, resulting in nearly all BC removed from the snow, the meltout still happens circa 2 days earlier compared to the no-ARF experiment.

Further complicating the effect is the fact that hydrophilic BC (which undergoes more efficient melt scavenging) has a larger MAC (enhanced absorption) compared to hydrophobic BC (Flanner et al., 2007). Our results suggest that distinguishing between species may play a secondary role in the determination of the overall impact of BC on snowmelt due to the compensating effect of stronger scavenging accompanied by stronger absorption and vice versa (Fig. 3c).

The 1-D model experiments further show that the definition of at least two layers in the snowpack model is important to allow for accumulation of impurities at the snow surface. This result in itself is not original: numerous prior studies have identified the importance of having multiple layers (Krinner et al., 2006; Flanner et al., 2007; Oaida et al., 2015). However, we further find that the model surface layer thickness (parameter *max_surface_layer*; see Table 2) has a great impact on the evolution of surface mixing ratios of BC, while at the same time the effect on albedo and snowmelt is small. This results from the fact that for all two-layer models the surface layer thickness is much thinner than the penetration depth of shortwave radiation. For example, in clean snow with an optical grain radius of 50 µm, the radiative intensity diminishes to $1/e$ of its surface value (the so-called penetration depth) in 25.5 mm SWE. For snow with an optical grain radius of 1000 µm, the penetration depth increases to 117 mm SWE (both results from Flanner et al., 2007, assuming a wavelength of 550 nm and a solar zenith angle of 60°). Thus, BC in the surface layer absorb efficiently in all two-layer scenarios and the difference in the albedo is relatively large compared to the no-ARF scenario (solid black line in the top graph of Fig. 3a), but relatively small among the two-layer scenarios (solid purple, red, and green curves in the top graph of Fig. 3a). However, there is a critical difference when a single-layer model is used (yellow curves in Fig. 3a) due to the aerosol being distributed uniformly throughout the snowpack instead of allowing accumulation at the surface. Thus, a large fraction of the BC is located at depths where the radiative intensity is much lower than in the top few mm of the snowpack. This leads to a weaker absorption efficiency and a less pronounced decrease in albedo compared to the two-layer models and thus to a shorter meltout shift compared to a clean snowpack than in the two-layer scenarios.

Observations of BC in melting snow support the accumulation of BC near the surface (Xu et al., 2012; Doherty et al., 2013; Sterle et al., 2013; Delaney et al., 2015). In a sequence of snow pits, Sterle et al. (2013) showed that during the ablation season, BC mixing ratios increase significantly near the snow surface (sampled in the top 2 cm) relative to bulk BC concentrations. They suggest that most likely a large fraction of previously deposited BC becomes concentrated near the surface. Delaney et al. (2015) also report surface BC increase during melt, to which BC being trapped at the snow surface is likely to contribute. BC increases in surface snow of up to an order of magnitude (Sterle et al., 2013; Doherty et al., 2016) and more (Xu et al., 2012) have been observed in natural snow during melt. Over most of the melt period, our results show a factor increase between 5 and 15 for the two-layer scenarios, which aligns well with observations. Higher values are mainly predicted shortly before meltout, when the snowpack is typically very thin and effects on discharge generation due to high increase in surface BC should be small.

We argue therefore the importance of providing, at a minimum, a separate surface layer, but recognize that simulated surface mixing ratios of BC are highly sensitive to the thickness of this layer. Since evaluation of model predictions for BC in snow is commonly performed by comparing simulated with observed BC mixing ratios in surface snow (e.g. Flanner et al., 2007; Forsström et al., 2013), this is a critical result. Snow is often sampled in the top few centimetres (typically 2 to 5 cm, e.g. Doherty et al., 2010; Aamaas et al., 2011; Forsström et al., 2013). This raises an interesting challenge given that the surface layer assumed in models is not a measurable property of snow. A comparison of model simulations with observations should therefore include some quan-

tification of the uncertainty resulting from the surface layer thickness parametrization.

6.2 Hydrologic response to BC deposition in a snowfall dominated catchment

We are interested in addressing the impact of BC deposition – and potentially other light absorbing aerosols – on the hydrology of snowfall dominated catchments. Studies have shown the potential impact LAISI may have on the timing of snowmelt (Skiles et al., 2012; Painter et al., 2012), while others have argued that the impact on climate may be significant (Flanner et al., 2007, 2009; Qian et al., 2009, 2011). Given the importance of snow for water resources for a significant portion of the population (Barnett et al., 2005; Sturm et al., 2017) and the rapid growth of BC emissions in certain regions of the world (e.g. Paliwal et al., 2016; Bond et al., 2013), our aim is to provide a mechanism to include this process in hydrologic forecasting to better address future impact studies.

Forsström et al. (2013) found BC seasonal mean snowpack concentrations from about 10 to 80 ng g^{-1} for different locations and time periods in mainland Scandinavia. Generally our results are within those presented in Forsström et al. (2013), though our max estimate lies above. However, Flanner et al. (2007) evaluated the global impact of the radiative forcing of BC in snow using a model that was compared with globally distributed surface BC measurements. For southern Norway, Flanner et al. (2007) predicted annual mean surface BC mixing ratios between 46 and 215 ng g^{-1} for the year 1998, placing our simulations fully within a reasonable range of prior reported values.

The impact resulting from BC deposition in our study is seen in the timing of the annual water balance. Inclusion of ARF generally increases early season melt and causes the snowpack to melt out earlier. Comparing the ARF and no-ARF scenarios, we see a general shift in the discharge, with the ARF scenario producing greater discharge early in the season, and having less discharge after June. Such a shift in seasonal water balance will potentially have impacts on soil moisture and agriculture (Blankinship et al., 2014), as well as on regional climate (Qian et al., 2011). While we recognize significant uncertainties associated with conceptual hydrologic modelling that may impact the applicability of these results (Beven and Binley, 1992; see also the uncertainty discussion in Sect. 6.3), we feel it provides a novel mechanism to address LAISI in a manner that, to date, is not available otherwise. As a reality check of the catchment-scale process representation, we evaluate the impact of the incorporation of BC deposition on albedo, radiative forcing, and snowpack storage.

6.2.1 Surface BC and albedo

Albedo is a critical parameter in any snowmelt model, with significant control over the energy balance. During the accumulation period, the average albedo of each scenario lies within the range of albedo of fresh snow with small optical grain radius combined with a high solar zenith angle (Gardner and Sharp, 2010) and is thus reasonable for a high-latitude snowpack during snow accumulation. The differences in snow albedo during the accumulation season are mostly due to differences in aerosol deposition and in the maximum surface layer thickness of the snowpack. The time series of mid estimate modelled surface BC is within the range of values for locations in mainland Scandinavia presented in Forsström et al. (2013) during the accumulation period. The min estimate predicts values at the lower bound and lies in the range of the background surface BC level found in Svalbard in the European High Arctic (5 ng g^{-1}, Aamaas et al., 2011; 30 ng g^{-1}, Clarke and Noone, 1985). Compared to Forsström et al. (2013), the surface BC level of the max estimate seems to exceed the range of values reasonable for mainland Scandinavia during snow accumulation and reflects a range of values that is rarely found in snowpacks outside Asia (Doherty et al., 2010; Forsström et al., 2013; Wang et al., 2013; AMAP, 2015).

At the end of the melt season, the evolution of surface BC yields reductions in albedo relative to the no-ARF case of about 0.03, 0.1, and over 0.3 for the min, mid, and max estimates, respectively. This has two reasons: first, with increasing grain radius during the melt season, the absorbing effect of BC gets more efficient due to deeper penetration of radiation into the snowpack, leading to a stronger effect of the BC deposition on albedo. Snow of larger grains has a larger extinction coefficient and more effective forward scattering properties (Flanner et al., 2007). Second, with the start of the melt season there is a widespread decrease in snow thickness, allowing BC to accumulate in the surface layer. This latter effect is strongly dependent on the applied scavenging ratios, as we demonstrated in the 1-D sensitivity study (Sect. 5.1). During the melt season, the mid estimate spatially averaged surface BC mixing ratio increases from 49 to about 250 ng g^{-1} (factor 5 increase) at the end of the melt season (beginning of July). Observations from Forsström et al. (2013) indicate that surface BC mixing ratios around 250 ng g^{-1} are well within the range of reasonable values for a melting Scandinavian snowpack. Furthermore, an increase in surface BC by a factor of 5 and higher during snowmelt is in line with observed BC trends in melting snow from different locations (Doherty et al., 2013, 2016; Xu et al., 2012). From this, we argue that our mid estimate simulation predicts a seasonal cycle in surface BC that is within reason.

For the max estimate, the increase is from roughly 100 to over 2500 ng g^{-1} (factor 25 increase). This strong seasonal cycle in surface BC is beyond what is observed for both absolute BC values in Scandinavian snowpacks and increase

relative to surface BC during snow accumulation. The min estimate, on the other hand, leads to a decrease in the BC surface mixing ratio. Even though many studies report an increase in surface BC during snowmelt (e.g. Conway et al., 1996; Doherty et al., 2013, 2016; Xu et al., 2012), there exist observations showing that a large fraction of BC can be flushed efficiently from the snowpack with the beginning of snowmelt (Lazarcik et al., 2017). This indicates that post-depositional enrichment processes and their significance in determining surface BC trends in melting snow require further exploration. We argue that the min estimate thus marks a reasonable lower bound estimate for the seasonal evolution of surface BC.

We recognize our max estimate results in a strong increase in surface BC mixing ratios mostly due to low BC scavenging with melt (note the strong increase from the end of March on in Fig. 6). This divergent evolution of surface BC mixing ratios in the min, mid, and max estimates reveals uncertainty in the representation of the fate of BC in snow during melt, which is also reflected in the literature (Doherty et al., 2013, 2016; Xu et al., 2012; Lazarcik et al., 2017).

6.2.2 BC-induced radiative forcing

The strong increase in RFS (Fig. 7a) and surface radiative forcing (Fig. 7b) during spring melt results from the combination of (i) the aforementioned decrease in snow albedo due to the increase in surface BC mixing ratios (e.g. melt amplification and the increasing optical grain radius in melting snow as discussed in Sect. 5.2.2) and (ii) the increasing daily solar irradiation due to a lower solar zenith angle and longer days.

The annual mean surface radiative forcings in this study are 0.284, 0.844, and 1.391 $\mathrm{W\,m^{-2}}$ for the min, mid, and max estimates. Averaged over Scandinavia (including Finland), Hienola et al. (2016) calculated lower values around 0.145 $\mathrm{W\,m^{-2}}$. However, Hienola et al. (2016)'s study includes large areas with shorter snow cover. Since the surface radiative forcing is strongly dependent on the snow cover evolution, higher values compared to Hienola et al. (2016) are expected due to the long lasting snow cover in our case study region. The mid estimate annual cycle of surface radiative forcing due to the presence of BC in the study region is of a similar magnitude to what is found over the Tibetan Plateau. Qian et al. (2011) report similar snow cover duration and maximum mean forcing during May of over 6 $\mathrm{W\,m^{-2}}$ using a global climate model. Due to the generally much lower snow-covered fraction in Qian et al. (2011)'s study region, however, RFS is presumably significantly higher on the Tibetan Plateau compared to our study region, which is in agreement with very high levels of BC reported for the Tibetan Plateau (Qian et al., 2011). Using a stand-alone version of SNICAR, we estimated RFS based on surface BC mixing ratios from Forsström et al. (2013) measured during melt in the top 5 cm of Scandinavian snowpacks to 4.7 to 18.2 $\mathrm{W\,m^{-2}}$ (95 % confidence interval; details described in Appendix A). These values agree well with our min and mid estimate RFS (Fig. 7), but are significantly lower than our max estimate predictions.

6.2.3 BC impact on catchment discharge and snow storage

We mention a shift in the seasonal water balance, with more melt early in the melt season resulting from enhanced RFS. However, from mid May the melt enhancement reduces and the differences in catchment SWE between the ARF and no-ARF scenarios decrease (Fig. 8b). One would expect with more incoming radiation, later in the season, the RFS effect to become further enhanced. However, this counter-intuitive result becomes clearer when one considers the impact of fractional snow-covered area and catchment-scale processes. The dynamics driven by the faster development of SCF (see Fig. 6a) is a limiting factor in the catchment-averaged snowmelt. By comparing Fig. 7a, which shows the RFS enhancement, with Fig. 7b, which shows total daily energy uptake in the catchment, we see that a threshold period is reached and total daily energy uptake decreases, while RFS is continually increasing. The SCF decrease with increased melt due to ARF counteracts the RFS effect itself, due to the reduction in area from which snow can actually melt. For discharge, this is manifested in the ARF scenarios as an enhancement during the beginning of the melt season attributed to RFS, whereas the decreased discharge later in the season is attributed to melt limitation caused by the faster growth of fractional bare ground areas.

Similar shifts in the annual water balance due to the impact from LAISI are reported for the Upper Colorado River Basin (Painter et al., 2010) and the Tibetan Plateau (Qian et al., 2011). Those regions are well-known hotspots of LAISI disturbance to snow cover (Painter et al., 2007; Qian et al., 2014). Our results suggest that the hydrologic cycle of regions that have not been the focus hitherto (such as Norway) might also be significantly affected by ARF.

Compared to observations, all simulations (ARF and no-ARF) tend to underestimate discharge during early melt season and overestimate discharge during late melt season (Fig. 8a). However, the magnitude of over- and underestimation strongly differs between the scenarios. By including ARF the volume error is reduced in both the early melt season (by increasing melt), and in late melt season (by subsequently decreasing melt generation in the catchment due to reduced SCF). Expressed as seasonal mean volume error for early and late melt season, the difference to observed discharge is largest for the no-ARF scenario and smallest for the max estimate. The max estimate reduces the volume error by −75.1 % during early melt season and −89.9 % during late melt season, relative to the no-ARF scenario (see Table 4). The min and mid estimates also reduce the volume error. Thus, on average, an improvement in simulated discharge is achieved during the melt season by accounting for

Table 4. Season mean volume error in discharge during the early (22 March to 29 May) and late (30 May to 10 August) melt seasons of the no-ARF, min, mid, and max scenarios compared to observed discharge. The percentage change shows an increase (+) or decrease (−) in the volume error compared to the no-ARF volume error.

scenario	early melt season discharge		late melt season discharge	
	($m^3\ s^{-1}$)	(%)	($m^3\ s^{-1}$)	(%)
no-ARF	−2.32	–	1.78	–
min estimate	−2.12	−8.7	1.60	−10.1
mid estimate	−1.52	−34.7	1.04	−41.6
max estimate	−0.57	−75.1	0.18	−89.8

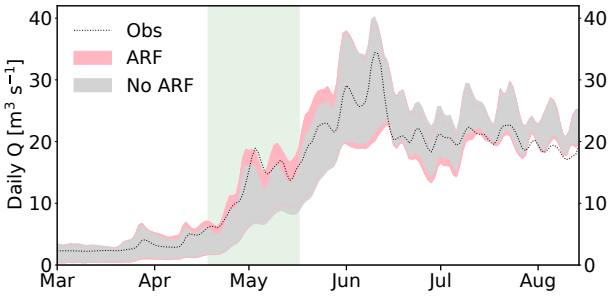

Figure 9. The 95 % confidence interval of simulated discharge due to parameter uncertainty when allowing for ARF (red) and disregarding ARF (grey), calculated using the GLUE method and averaged over the 6-year simulation period. The shaded box marks the period of the melt season, where observations tend to lie outside the uncertainty bounds of the no-ARF simulations.

BC RFS. Similar results are achieved when estimating model parameters using a no-ARF scenario (not shown). However, we acknowledge that further studies are needed in order to be able to confirm a general model improvement when accounting for ARF in snow dominated catchments. Certain mechanisms can lead to model improvements for the wrong reason when applying ARF (Kirchner, 2006). Structural deficits of the model might lead to a negligence of processes that are important for the spring melt generation. The implementation of ARF could then optimize the model towards the observations and counteract errors coming (partly) from a missing process that is not related to ARF. A further potential mechanism is related to the equifinality of conceptual models. These implications coming from model parameter uncertainty are discussed in Sect. 6.3 alongside with further sources of uncertainty.

6.3 Uncertainties

There are numerous challenges associated with the development of an algorithm that mixes conceptual hydrologic parametrizations with physically based approaches. Both the literature and our analysis highlight aspects that warrant a deeper investigation of ARF-induced uncertainty. The intent with this work is to introduce a new algorithm; however, as indicated in Pappenberger and Beven (2006), we feel it is important to provide an initial assessment of the uncertainty introduced with the addition of ARF terms. To achieve this we have conducted a generalized likelihood uncertainty estimation (GLUE; Beven and Binley, 1992) which provides an assessment of the degree of variability in behavioural models resulting from equifinality.

With respect to the implementation of a physical albedo model, the treatment of the darkening effect of LAISI adds additional degrees of freedom to the parameter space of the model due to the introduction of new parameters (scavenging ratios, surface layer thickness, BC input scaling factor; see the bottom four parameters in Table 2). In order to investigate the abilities and limits of the model with and without ARF to reflect the observed discharge, we quantify the parameter uncertainty prior and posterior to the implementation of ARF calculations (Fig. 9; details in Appendix B). Uncertainties are generally largest during snowmelt and summer because various parameters only play an active role in calculating discharge during snowmelt. Including ARF calculation in the model leads to a shift of the uncertainty band to higher values during April and May, and lower values during June and July, due to increased melt under the impact of ARF. From mid May to mid June, the ARF-induced shift in the uncertainty band leads to observations being within or closer to the border of the uncertainty bands (shaded box in Fig. 9), which can be interpreted as an improvement to the model. This would imply that in the model without ARF, albedo decays not sufficiently enough during spring in order to generate enough snowmelt, resulting in an underestimation of discharge in April and May. However, we admit that further testing is needed to draw a more accurate conclusion, as discussed above. Perhaps more importantly, it appears that we have not increased uncertainty much by adding complexity. In general, both simulations with and without ARF lead to acceptable results. However, we enable the inclusion of a potentially important variable, particularly with respect to increasing emissions of light absorbing aerosols due to population growth.

In our case study, further uncertainties result from mixing ratios of BC in the snowpack due to prescribed BC deposition, and LAISI other than BC not accounted for in the simulations:

i. prescribed BC deposition

   In the approach presented here, we use prescribed BC deposition mass fluxes. Even though this is common practice (e.g. Goldenson et al., 2012; Lee et al., 2013; Jiao et al., 2014), it was shown by Doherty et al. (2014) that the decoupling of aerosol deposition from the water mass flux of falling snow can lead to an overesti-

mation of surface mixing ratios by a factor of 1.5–2.5. However, we would like to highlight an important difference between our approach and the one Doherty et al. (2014) claim to be problematic: first, the high bias in surface snow BC mixing ratios described by Doherty et al. (2014) refers to global climate model simulations with prescribed aerosol deposition rates (wet and dry), where the input aerosol fields are interpolated in time from monthly means. Therefore, the episodic nature of aerosol deposition due to wet deposition is generally absent in the prescribed aerosol fields. The coupling of the interpolated fields with highly variable meteorology (in particular precipitation) results in the high bias (Doherty et al., 2014). In our case study, we use deposition fields originating from the REMO-HAM regional aerosol climate model, forced with ERA-Interim reanalysis data at the boundaries. REMO-HAM output is 3-hourly, which we re-sampled to daily means in order to have consistency between the deposition fields and the observed daily precipitation used as input data in the hydrological simulations. The daily time step allows us to preserve the episodic nature of aerosol deposition. Moreover, the daily BC wet deposition rates should not be biased due to major inaccuracies in precipitation, as REMO-HAM has been shown to reproduce the Scandinavian precipitation realistically (Pietikäinen et al., 2012). The high bias occurring when using interpolated monthly averages as input should therefore be minimized. Additionally, and significantly, Doherty et al. (2014) (and the critiques therein) address an objective with consideration to climate impacts. Our analysis is focused on the impact on the hydrological cycle. Our simulations suggest that BC RFS is mostly important during spring time, where surface BC mixing ratios are predominantly controlled by melt processes, and not by deposition processes (as shown in Figs. 3 and 6b).

ii. LAISI other than BC

By including only BC deposition in our simulation, we likely underestimate the additional effect of further LAISI species such as mineral dust (Di Mauro et al., 2015; Painter et al., 2010), mixing of the snow with soil from the underlying ground or local sources (Wang et al., 2013), and biological processes (Lutz et al., 2016). Neglecting additional RFS from LAISI other than BC is likely to result in an underestimation of the overall effect of LAISI on snowmelt and discharge generation. Especially the contribution from dust is critical since it has been shown that in many regions such as the Rocky Mountains (Painter et al., 2012), Utah (Doherty et al., 2016), the southern edge of the Himalayas (Gautam et al., 2013), and Svalbard (Forsström et al., 2013), dust can play a significant role in terms of RFS or even is the dominating LAISI. For Norway, however, analysis conducted by Forsström et al. (2013) indicates that dust might only play a minor role. By comparing samples from Svalbard and near Tromsø, Norway, Forsström et al. (2013) showed that there exits a distinctive difference between the Arctic Archipelago and the mainland. The BC mixing ratio from mineral-dust-rich Svalbard measured by the thermal/optical method used in Forsström et al. (2013) averaged about half the mixing ratio of insoluble light absorbing particulates (including dust) measured by an optical method (ISSW: Integrating Sphere/Integrating Sandwich; e.g. Doherty et al., 2010). Samples collected close to Tromsø, on the other hand, resulted in BC that averaged about 1.3 times the ILAP mixing ratios. Due to the fact that the ISSW method overestimates BC for samples containing dust, Forsström et al. (2013) argue that the comparison of both methods can be used to draw conclusions about the pollution regime. However, due to the small number of samples and the single-location analysis, this needs to be addressed more in future studies in order to identify the relative importance of different LAISI species.

With respect to our study, we acknowledge that including only BC is a shortcoming with respect to the overall effect of LAISI. However, by demonstrating the significant effect of BC on accelerating snowmelt and discharge generation, our study gives a conservative estimate of the effect of LAISI and urges a more detailed investigation.

7 Conclusions

Herein we presented a newly developed snow algorithm for application in hydrologic models that allows a new class of model input variable: the deposition rates of light absorbing aerosols. By coupling a radiative transfer model for snow to an energy-balance-based snowpack model, we are providing a tool that can be used to determine the effect of various species of LAISI at the catchment scale. In this analysis we have focused solely on BC and acknowledge it therefore likely represents a conservative estimate. This work presents a novel analysis of the impact of BC deposition to snow on the hydrologic cycle through 1-D sensitivity studies and catchment-scale hydrologic modelling. From a 1-D model study, presented in Sect. 5.1, we conclude that

i. the implementation of at least two layers (a thin surface layer and a bottom layer) is of outstanding importance to capture the potential effect of melt amplification on the near-surface LAISI evolution. The parametrization of the surface layer has only a small effect on the snow albedo and melt rate as long as the surface layer thickness (in SWE) is sufficiently thin (e.g. thinner than the penetration depth of shortwave radiation). However, the evolution of the LAISI surface mixing ratio is highly sensitive to the surface layer thickness. For this reason, we suggest including a surface layer thickness varia-

tion in model studies when comparing simulated and observed LAISI mixing ratios sampled in the top few centimetres of snow.

ii. The determination of how LAISI are washed out of the snowpack with meltwater has a great effect on the evolution of LAISI concentration near the surface, snow albedo, and melt rate. Due to rare observations of this effect under controlled conditions, the uncertainties are high and our findings show the need for more detailed understanding of the processes involved due to the high importance of the overall effect of LAISI on the snowpack evolution.

To demonstrate the significance of BC radiative forcing for the hydrologic cycle at the catchment scale, we demonstrated the effect of BC deposition and the subsequent implications for snowmelt and discharge generation on a remote Norwegian mountain catchment. The study indicates that inclusion of BC in snow is likely to have a significant impact on melt timing, and that the effect on the discharge generation leads to a shift in the annual water balance. Our simulations further suggest that melt amplification can have severe implications for both the snowpack evolution and the discharge regime of a catchment, which means that the seasonal cycle of the surface BC mixing ratio is of great importance. However, large uncertainties are connected with the representation of surface enrichment of BC. A more robust understanding of the fate of BC in melting snow is essential to fully assess impacts on the hydrologic cycle.

Including radiative forcing from BC in the simulations leads to a reduction in volume error during the early and late melt season in our simulations. We conclude from our study that hydrological modelling can potentially be improved by including the effect of LAISI, especially when the model approach implies a physically based representation of the snowpack in general and the snow albedo in particular. However, more research in the area of catchment-scale impact of LAISI is needed to support this. The approach and algorithm presented in this analysis provide a tool to target this in future applications.

Data availability. Meteorological observations for the Atnsjoen catchment are provided by the Norwegian Meteorological Institute (MET) and the Norwegian Water Resources and Energy Directorate (NVE). Observed streamflow data are provided by NVE. The data are published in Matt (2018), alongside gridded BC wet and dry deposition data and SHyFT model configuration files. The source code of SHyFT is available on GitHub (https://www.github.com/statkraft). More information may be found at http://www.mn.uio.no/geo/english/research/projects/hycamp.

Appendix A: Radiative forcing in snow estimated from Forsström et al. (2013)

In order to calculate radiative forcing in snow (RFS) from surface concentrations during melt reported in Forsström et al. (2013), several assumptions have been made. For each input variable, a certain reasonable range is estimated, suited to snow properties during melt conditions:

- snow optical grain radius: 500–1000 µm;
- snow density: 400–600 kg m^{-3};
- BC mixing ratio: 50–200 ng g^{-1} (from Forsström et al., 2013).

Forsström et al. (2013) report six time series of BC surface concentrations sampled in the top 5 cm of the snowpack, all of which cover the snowmelt period at three locations in Scandinavia; however, only one location can be considered remote without pollution from local sources (Abisko, Sweden). The range of BC mixing ratios during melt is estimated from this location. Global radiation during spring is estimated to 210 W m^{-2}. The value has been calculated from the input time series of our study region, in order to receive comparable results. The daily mean solar zenith angle has been set to 60° and BC mixing ratios below the top 5 cm to 0 ng g^{-1}, since no further information is available. The latter might lead to an underestimation of RFS, and results can be seen as a conservative estimate; 1000 realizations with SNICAR have been conducted using different input variable sets, with random values for each input variable according to a uniform distribution in the stated range. Resulting RFS values are presented as the 95 % confidence interval to 4.7 to 18.2 W m^{-2}. The mean is 11.2 W m^{-2}.

Appendix B: Parameter uncertainty with GLUE

We determine parameter uncertainty using the GLUE method (Beven and Binley, 1992). Lower and upper bounds of parameters used in the calculation are shown in Table B1. We use the Nash–Sutcliffe model efficiency (see Eq. 10) as a likelihood function and choose a threshold value of 0.74 (0.1 below the best calibration result) for accepting parameter sets as behavioural parameter sets. To identify the impact of ARF on model uncertainty, we run GLUE twice, first without ARF applied, and in a second round of simulations accounting for ARF. Random parameter sets are created by choosing parameters according to a uniform distribution in the range of the parameter bounds. For each of the two uncertainty estimations, a total of 10 000 model realizations was drawn, of which 1435 (no-ARF) and 1831 (ARF) parameter sets were rated as behavioural parameter sets. This accounts for about 14 and 18 % of the total samples, respectively.

Table B1. Model parameter bounds used in the uncertainty estimation with the GLUE method. Parameters used to determine ARF are marked with *.

Parameter	Unit	Lower bound	Upper bound
c_1	–	−7.0	−2.0
c_2	–	0.1	1.0
c_3	–	−0.1	0.0
ae_scale_factor	–	0.7	2.0
tx	°C	−2.0	1.0
wind_const	–	3.0	10.0
wind_scale	–	0.5	2.0
snowfall_reset_depth	mm SWE	3.0	7.0
snow_cv_forest	–	0.15	0.2
snow_cv_intercept	–	−0.03	−0.07
snow_cv_slope	m^{-1}	0.0003	0.0007
max_water	–	0.5	0.15
$A_{s,0}$	m^2 kg^{-1}	50.0	100.0
surface_magnitude	mm SWE	20.0	40.0
max_surface_layer*	mm SWE	4.0	16.0
depo_factor*	–	0.5	1.5
k_{phob}*	–	0.003	0.3
k_{phil}*	–	0.02	2.0

Competing interests. The authors declare that they have no conflict of interest.

Acknowledgements. This work was conducted within the Norwegian Research Council's INDNOR programme under the Hydrologic sensitivity to Cryosphere-Aerosol interaction in Mountain Processes (HyCAMP) project (NFR no. 222195). We thank the Mitigation of Arctic warming by controlling European black carbon emissions (MACEB) project for their help concerning the REMO-HAM simulations. Furthermore, we thank the International Institute for Applied System Analysis (IIASA), especially Kaarle Kupiainen and Zbigniew Klimont, for providing the emissions data. Sigbjorn Helset and Statkraft AS, in general, have been vital resources in the development of the algorithm and, in particular, the implementation in Shyft. The ECHAM-HAMMOZ model is developed by a consortium composed of the ETH Zurich, the Max Planck Institut für Meteorologie, the Forschungszentrum Jülich, the University of Oxford, and the Finnish Meteorological Institute, and is managed by the Center for Climate Systems Modeling (C2SM) at the ETH Zurich.

Edited by: Jan Seibert
Reviewed by: three anonymous referees

References

Aamaas, B., Bøggild, C. E., Stordal, F., Berntsen, T., Holmen, K., and Ström, J.: Elemental carbon deposition to Svalbard snow from Norwegian settlements and long-range transport, Tellus B, 63, 340–351, https://doi.org/10.1111/j.1600-0889.2011.00531.x, 2011.

Aas, K. S., Gisnås, K., Westermann, S., and Berntsen, T. K.: A Tiling Approach to Represent Subgrid Snow Variability in Coupled Land Surface–Atmosphere Models, J. Hydrometeorol., 18, 49–63, https://doi.org/10.1175/JHM-D-16-0026.1, 2017.

AMAP: AMAP Assessment 2015: Black carbon and ozone as Arctic climate forcers, Arctic Monitoring and Assessment Programme (AMAP), Oslo, Norway, 2015.

Anderson, E. A.: A Point Energy and Mass Balance Model of a Snow Cover, NOAA Technical Report NWS, National Weather Service, Office of Hydrology, Silver Spring, Md, USA, available at: https://searchworks.stanford.edu/view/2518510 (last access: 5 April 2016), 19, 1976.

Barnett, T. P., Adam, J. C., and Lettenmaier, D. P.: Potential impacts of a warming climate on water availability in snow-dominated regions, Nature, 438, 303–309, https://doi.org/10.1038/nature04141, 2005.

Berghuijs, W. R., Woods, R. A., Hutton, C. J., and Sivapalan, M.: Dominant flood generating mechanisms across the United States, Geophys. Res. Lett., 43, 4382–4390, https://doi.org/10.1002/2016GL068070, 2016.

Beven, K. and Binley, A.: The future of distributed models: Model calibration and uncertainty prediction, Hydrol. Process., 6, 279–298, https://doi.org/10.1002/hyp.3360060305, 1992.

Blankinship, J. C., Meadows, M. W., Lucas, R. G., and Hart, S. C.: Snowmelt timing alters shallow but not deep soil moisture in the Sierra Nevada, Water Resour. Res., 50, 1448–1456, https://doi.org/10.1002/2013WR014541, 2014.

Bond, T. C., Habib, G., and Bergstrom, R. W.: Limitations in the enhancement of visible light absorption due to mixing state, J. Geophys. Res., 111, D20211, https://doi.org/10.1029/2006JD007315, 2006.

Bond, T. C., Doherty, S. J., Fahey, D. W., Forster, P. M., Berntsen, T., DeAngelo, B. J., Flanner, M. G., Ghan, S., Kärcher, B., Koch, D., Kinne, S., Kondo, Y., Quinn, P. K., Sarofim, M. C., Schultz, M. G., Schulz, M., Venkataraman, C., Zhang, H., Zhang, S., Bellouin, N., Guttikunda, S. K., Hopke, P. K., Jacobson, M. Z., Kaiser, J. W., Klimont, Z., Lohmann, U., Schwarz, J. P., Shindell, D., Storelvmo, T., Warren, S. G., and Zender, C. S.: Bounding the role of black carbon in the climate system: A scientific assessment, J. Geophys. Res.-Atmos., 118, 5380–5552, https://doi.org/10.1002/jgrd.50171, 2013.

Brun, E.: Investigation on wet-snow metamorphims in respect of liquid water content, Ann. Glaciol., 13, 22–26, https://doi.org/10.1017/S0260305500007576, 1989.

Bryant, A. C., Painter, T. H., Deems, J. S., and Bender, S. M.: Impact of dust radiative forcing in snow on accuracy of operational runoff prediction in the Upper Colorado River Basin, Geophys. Res. Lett., 40, 3945–3949, https://doi.org/10.1002/grl.50773, 2013.

Burkhart, J. F., Helset, S., Abdella, Y. S., and Lappegard, G.: Operational Research: Evaluating Multimodel Implementations for 24/7 Runtime Environments, in: American Geophysical Union, Fall General Assembly, 12–16 December 2016, San Francisco, USA, 2016.

Clarke, A. D. and Noone, K. J.: Soot in the arctic snowpack a cause for perturbations in radiative transfer, Atmos. Environ., 19, 2045–2053, 1985.

Conway, H., Gades, A., and Raymond, C. F.: Albedo of dirty snow during conditions of melt, Water Resour. Res., 32, 1713–1718, 1996.

Dee, D. P., Uppala, S. M., Simmons, A. J., Berrisford, P., Poli, P., Kobayashi, S., Andrae, U., Balmaseda, M. A., Balsamo, G., Bauer, P., Bechtold, P., Beljaars, A. C. M., van de Berg, L., Bidlot, J., Bormann, N., Delsol, C., Dragani, R., Fuentes, M., Geer, A. J., Haimberger, L., Healy, S. B., Hersbach, H., Hølm, E. V., Isaksen, L., Kållberg, P., Köhler, M., Matricardi, M., McNally, A. P., Monge-Sanz, B. M., Morcrette, J.-J., Park, B.-K., Peubey, C., de Rosnay, P., Tavolato, C., Thépaut, J.-N., and Vitart, F.: The ERA-Interim reanalysis: configuration and performance of the data assimilation system, Q. J. Roy. Meteor. Soc., 137, 553–597, https://doi.org/10.1002/qj.828, 2011.

Delaney, I., Kaspari, S., and Jenkins, M.: Black carbon concentrations in snow at Tronsen Meadow in Central Washington from 2012 to 2013: Temporal and spatial variations and the role of local forest fire activity, J. Geophys. Res.-Atmos., 120, 9160–9172, https://doi.org/10.1002/2015JD023762, 2015.

Dentener, F., Kinne, S., Bond, T., Boucher, O., Cofala, J., Generoso, S., Ginoux, P., Gong, S., Hoelzemann, J. J., Ito, A., Marelli, L., Penner, J. E., Putaud, J.-P., Textor, C., Schulz, M., van der Werf, G. R., and Wilson, J.: Emissions of primary aerosol and precursor gases in the years 2000 and 1750 prescribed data-sets for AeroCom, Atmos. Chem. Phys., 6, 4321–4344, https://doi.org/10.5194/acp-6-4321-2006, 2006.

Di Mauro, B., Fava, F., Ferrero, L., Garzonio, R., Baccolo, G., Delmonte, B., and Colombo, R.: Mineral dust impact on snow radiative properties in the European Alps combining ground, UAV, and satellite observations, J. Geophys. Res.-Atmos., 120, 6080–6097, https://doi.org/10.1002/2015JD023287, 2015.

Diggle, P. J. and Ribeiro, P. J.: Model-based Geostatistics, Springer Series in Statistics, Springer, New York, USA, 2007.

Doherty, S. J., Warren, S. G., Grenfell, T. C., Clarke, A. D., and Brandt, R. E.: Light-absorbing impurities in Arctic snow, Atmos. Chem. Phys., 10, 11647–11680, https://doi.org/10.5194/acp-10-11647-2010, 2010.

Doherty, S. J., Grenfell, T. C., Forsström, S., Hegg, D. L., Brandt, R. E., and Warren, S. G.: Observed vertical redistribution of black carbon and other insoluble light-absorbing particles in melting snow, J. Geophys. Res.-Atmos., 118, 5553–5569, https://doi.org/10.1002/jgrd.50235, 2013.

Doherty, S. J., Bitz, C. M., and Flanner, M. G.: Biases in modeled surface snow BC mixing ratios in prescribed-aerosol climate model runs, Atmos. Chem. Phys., 14, 11697–11709, https://doi.org/10.5194/acp-14-11697-2014, 2014.

Doherty, S. J., Hegg, D. A., Johnson, J. E., Quinn, P. K., Schwarz, J. P., Dang, C., and Warren, S. G.: Causes of variability in light absorption by particles in snow at sites in Idaho and Utah, J. Geophys. Res.-Atmos., 121, 4751–4768, https://doi.org/10.1002/2015JD024375, 2016.

Domine, F., Taillandier, A.-S., and Simpson, W. R.: A parameterization of the specific surface area of seasonal snow for field use and for models of snowpack evolution, J. Geophys. Res.-Earth, 112, F02031, https://doi.org/10.1029/2006JF000512, 2007.

Engelhardt, M., Schuler, T. V., and Andreassen, L. M.: Contribution of snow and glacier melt to discharge for highly glacierised catchments in Norway, Hydrol. Earth Syst. Sci., 18, 511–523, https://doi.org/10.5194/hess-18-511-2014, 2014.

Flanner, M. G. and Zender, C. S.: Linking snowpack microphysics and albedo evolution, J. Geophys. Res.-Atmos., 111, D12208, https://doi.org/10.1029/2005JD006834, 2006.

Flanner, M. G., Zender, C. S., Randerson, J. T., and Rasch, P. J.: Present-day climate forcing and response from black carbon in snow, J. Geophys. Res.-Atmos., 112, D11202, https://doi.org/10.1029/2006JD008003, 2007.

Flanner, M. G., Zender, C. S., Hess, P. G., Mahowald, N. M., Painter, T. H., Ramanathan, V., and Rasch, P. J.: Springtime warming and reduced snow cover from carbonaceous particles, Atmos. Chem. Phys., 9, 2481–2497, https://doi.org/10.5194/acp-9-2481-2009, 2009.

Forsström, S., Isaksson, E., Skeie, R. B., Ström, J., Pedersen, C. A., Hudson, S. R., Berntsen, T. K., Lihavainen, H., Godtliebsen, F., and Gerland, S.: Elemental carbon measurements in European Arctic snow packs, J. Geophys. Res.-Atmos., 118, 13614–13627, https://doi.org/10.1002/2013JD019886, 2013.

Førland, E. J.: Nedbørens høydeavhengighet (Precipitation and topography), Klima, 1, 3–24, 1979 (in Norwegian with English summary).

Gardner, A. S. and Sharp, M. J.: A review of snow and ice albedo and the development of a new physically based broadband albedo parameterization, J. Geophys. Res., 115, F01009, https://doi.org/10.1029/2009JF001444, 2010.

Gautam, R., Hsu, N. C., Lau, W. K.-M., and Yasunari, T. J.: Satellite observations of desert dust-induced Himalayan snow darkening, Geophys. Res. Lett., 40, 988–993, https://doi.org/10.1002/grl.50226, 2013.

Ghimirey, S.: Runoff modelling for Bhutan using satellite data, Master's thesis, Norwegian University of Science and Technology, available at: http://hdl.handle.net/11250/2407599 (last access: 24 August 2017), 2016.

Gisnås, K., Westermann, S., Schuler, T. V., Melvold, K., and Etzelmüller, B.: Small-scale variation of snow in a regional permafrost model, The Cryosphere, 10, 1201–1215, https://doi.org/10.5194/tc-10-1201-2016, 2016.

Goldenson, N., Doherty, S. J., Bitz, C. M., Holland, M. M., Light, B., and Conley, A. J.: Arctic climate response to forcing from light-absorbing particles in snow and sea ice in CESM, Atmos. Chem. Phys., 12, 7903–7920, https://doi.org/10.5194/acp-12-7903-2012, 2012.

Hegdahl, T. J., Tallaksen, L. M., Engeland, K., Burkhart, J. F., and Xu, C.-Y.: Discharge sensitivity to snowmelt parameterization: a case study for Upper Beas basin in Himachal Pradesh, India, Hydrol. Res., 47, 683–700, https://doi.org/10.2166/nh.2016.047, 2016.

Hienola, A. I., Pietikäinen, J.-P., Jacob, D., Pozdun, R., Petäjä, T., Hyvärinen, A.-P., Sogacheva, L., Kerminen, V.-M., Kulmala, M., and Laaksonen, A.: Black carbon concentration and deposition estimations in Finland by the regional aerosol–climate model REMO–HAM, Atmos. Chem. Phys., 13, 4033–4055, https://doi.org/10.5194/acp-13-4033-2013, 2013.

Hienola, A. I., O'Donnell, D., Pietikäinen, J.-P., Svensson, J., Lihavainen, H., Virkula, A., Korhonen, H., and Laaksonen, A.: The radiative impact of Nordic anthropogenic black carbon, Tellus B, 68, 27428, https://doi.org/10.3402/tellusb.v68.27428, 2016.

Jacobson, M. Z.: Climate response of fossil fuel and biofuel soot, accounting for soot's feedback to snow and sea ice albedo and emissivity, J. Geophys. Res.-Atmos., 109, D21201, https://doi.org/10.1029/2004JD004945, 2004.

Jeelani, G., Feddema, J. J., van der Veen, C. J., and Stearns, L.: Role of snow and glacier melt in controlling river hydrology in Liddar watershed (western Himalaya) under current and future climate, Water Resour. Res., 48, W12508, https://doi.org/10.1029/2011WR011590, 2012.

Jiao, C., Flanner, M. G., Balkanski, Y., Bauer, S. E., Bellouin, N., Berntsen, T. K., Bian, H., Carslaw, K. S., Chin, M., De Luca, N., Diehl, T., Ghan, S. J., Iversen, T., Kirkevåg, A., Koch, D., Liu, X., Mann, G. W., Penner, J. E., Pitari, G., Schulz, M., Seland, Ø., Skeie, R. B., Steenrod, S. D., Stier, P., Takemura, T., Tsigaridis, K., van Noije, T., Yun, Y., and Zhang, K.: An AeroCom assessment of black carbon in Arctic snow and sea ice, Atmos. Chem. Phys., 14, 2399–2417, https://doi.org/10.5194/acp-14-2399-2014, 2014.

Jonas, T., Rixen, C., Sturm, M., and Stoeckli, V.: How alpine plant growth is linked to snow cover and climate variability, J. Geophys. Res., 113, G03013, https://doi.org/10.1029/2007JG000680, 2008.

Junghans, N., Cullmann, J., and Huss, M.: Evaluating the effect of snow and ice melt in an Alpine headwater catchment and further downstream in the River Rhine, Hydrolog. Sci. J., 56, 981–993, https://doi.org/10.1080/02626667.2011.595372, 2011.

Kaspari, S., McKenzie Skiles, S., Delaney, I., Dixon, D., and Painter, T. H.: Accelerated glacier melt on Snow Dome, Mount Olympus, Washington, USA, due to deposition of black carbon

and mineral dust from wildfire, J. Geophys. Res.-Atmos., 120, 2793–2807, https://doi.org/10.1002/2014JD022676, 2015.

Kawagoe, S., Kazama, S., and Ranjan Sarukkalige, P.: Assessment of snowmelt triggered landslide hazard and risk in Japan, Cold Reg. Sci. Technol., 58, 120–129, https://doi.org/10.1016/j.coldregions.2009.05.004, 2009.

Kirchner, J. W.: Getting the right answers for the right reasons: Linking measurements, analyses, and models to advance the science of hydrology, Water Resour. Res., 42, W03S04, https://doi.org/10.1029/2005WR004362, 2006.

Kirchner, J. W.: Catchments as simple dynamical systems: Catchment characterization, rainfall-runoff modeling, and doing hydrology backward, Water Resour. Res., 45, W2429, https://doi.org/10.1029/2008WR006912, 2009.

Klemes, V.: Operational testing of hydrological simulation models, Hydrolog. Sci. J., 31, 13–24, https://doi.org/10.1080/02626668609491024, 1986.

Klimont, Z., Höglund-Isaksson, L., Heyes, C., Rafaj, P., Schöpp, W., Cofala, J., Borken-Kleefeld, J., Purohit, P., Kupiainen, K., Winiwarter, W., Amann, M., Zhao, B., Wang, S., Bertok, I., and Sander, R.: Global scenarios of air pollutants and methane: 1990–2050, in preparation, 2016.

Klimont, Z., Kupiainen, K., Heyes, C., Purohit, P., Cofala, J., Rafaj, P., Borken-Kleefeld, J., and Schöpp, W.: Global anthropogenic emissions of particulate matter including black carbon, Atmos. Chem. Phys., 17, 8681–8723, https://doi.org/10.5194/acp-17-8681-2017, 2017.

Kolberg, S. and Gottschalk, L.: Interannual stability of grid cell snow depletion curves as estimated from MODIS images, Water Resour. Res., 46, W11555, https://doi.org/10.1029/2008WR007617, 2010.

Krinner, G., Boucher, O., and Balkanski, Y.: Ice-free glacial northern Asia due to dust deposition on snow, Clim. Dynam., 27, 613–625, https://doi.org/10.1007/s00382-006-0159-z, 2006.

Lazarcik, J., Dibb, J. E., Adolph, A. C., Amante, J. M., Wake, C. P., Scheuer, E., Mineau, M. M., and Albert, M. R.: Major fraction of black carbon is flushed from the melting New Hampshire snowpack nearly as quickly as soluble impurities, J. Geophys. Res.-Atmos., 122, 537–553, https://doi.org/10.1002/2016JD025351, 2017.

Lee, Y. H., Lamarque, J.-F., Flanner, M. G., Jiao, C., Shindell, D. T., Berntsen, T., Bisiaux, M. M., Cao, J., Collins, W. J., Curran, M., Edwards, R., Faluvegi, G., Ghan, S., Horowitz, L. W., McConnell, J. R., Ming, J., Myhre, G., Nagashima, T., Naik, V., Rumbold, S. T., Skeie, R. B., Sudo, K., Takemura, T., Thevenon, F., Xu, B., and Yoon, J.-H.: Evaluation of preindustrial to present-day black carbon and its albedo forcing from Atmospheric Chemistry and Climate Model Intercomparison Project (ACCMIP), Atmos. Chem. Phys., 13, 2607–2634, https://doi.org/10.5194/acp-13-2607-2013, 2013.

Liston, G. E.: Representing Subgrid Snow Cover Heterogeneities in Regional and Global Models, J. Climate, 17, 1381–1397, 2004.

Lutz, S., Anesio, A. M., Raiswell, R., Edwards, A., Newton, R. J., Gill, F., and Benning, L. G.: The biogeography of red snow microbiomes and their role in melting arctic glaciers, Nat. Commun., 7, 11968, https://doi.org/10.1038/ncomms11968, 2016.

Matt, F. N.: Meteorological forcing data and model settings for "Modelling hydrologic impacts of light absorbing aerosol deposition on snow at the catchment scale" [Data set], Norstore, available at: https://doi.org/10.11582/2018.00001 (last access: 23 October 2017), 2018.

Oaida, C. M., Xue, Y., Flanner, M. G., Skiles, S. M., De Sales, F., and Painter, T. H.: Improving snow albedo processes in WRF/SSiB regional climate model to assess impact of dust and black carbon in snow on surface energy balance and hydrology over western U.S., J. Geophys. Res.-Atmos., 120, 3228–3248, https://doi.org/10.1002/2014JD022444, 2015.

Painter, T. H., Barrett, A. P., Landry, C. C., Neff, J. C., Cassidy, M. P., Lawrence, C. R., McBride, K. E., and Farmer, G. L.: Impact of disturbed desert soils on duration of mountain snow cover, Geophys. Res. Lett., 34, L12502, https://doi.org/10.1029/2007GL030284, 2007.

Painter, T. H., Deems, J. S., Belnap, J., Hamlet, A. F., Landry, C. C., and Udall, B.: Response of Colorado River runoff to dust radiative forcing in snow, P. Natl. Acad. Sci. USA, 107, 17125–17130, https://doi.org/10.1073/pnas.0913139107, 2010.

Painter, T. H., Skiles, S. M., Deems, J. S., Bryant, A. C., and Landry, C. C.: Dust radiative forcing in snow of the Upper Colorado River Basin: 1. A 6 year record of energy balance, radiation, and dust concentrations, Water Resour. Res., 48, W07521, https://doi.org/10.1029/2012WR011985, 2012.

Paliwal, U., Sharma, M., and Burkhart, J. F.: Monthly and spatially resolved black carbon emission inventory of India: uncertainty analysis, Atmos. Chem. Phys., 16, 12457–12476, https://doi.org/10.5194/acp-16-12457-2016, 2016.

Pappenberger, F. and Beven, K. J.: Ignorance is bliss: Or seven reasons not to use uncertainty analysis, Water Resour. Res., 42, 1944–7973, https://doi.org/10.1029/2005WR004820, 2006.

Pietikäinen, J.-P., O'Donnell, D., Teichmann, C., Karstens, U., Pfeifer, S., Kazil, J., Podzun, R., Fiedler, S., Kokkola, H., Birmili, W., O'Dowd, C., Baltensperger, U., Weingartner, E., Gehrig, R., Spindler, G., Kulmala, M., Feichter, J., Jacob, D., and Laaksonen, A.: The regional aerosol-climate model REMO-HAM, Geosci. Model Dev., 5, 1323–1339, https://doi.org/10.5194/gmd-5-1323-2012, 2012.

Pietikäinen, J.-P., Kupiainen, K., Klimont, Z., Makkonen, R., Korhonen, H., Karinkanta, R., Hyvärinen, A.-P., Karvosenoja, N., Laaksonen, A., Lihavainen, H., and Kerminen, V.-M.: Impacts of emission reductions on aerosol radiative effects, Atmos. Chem. Phys., 15, 5501–5519, https://doi.org/10.5194/acp-15-5501-2015, 2015.

Powell, M.: The BOBYQA algorithm for bound constrained optimization without derivatives, technical report, Department of Applied Mathematics and Theoretical Physics, Cambridge University, Cambridge, 2009.

Priestley, C. H. B. and Taylor, R. J.: On the assessment of surface heat flux and evaporation using large-scale parameters, Mon. Weather Rev., 100, 81–92, 1972.

Qian, Y., Gustafson, W. I., Leung, L. R., and Ghan, S. J.: Effects of soot-induced snow albedo change on snowpack and hydrological cycle in western United States based on Weather Research and Forecasting chemistry and regional climate simulations, J. Geophys. Res.-Atmos., 114, D03108, https://doi.org/10.1029/2008JD011039, 2009.

Qian, Y., Flanner, M. G., Leung, L. R., and Wang, W.: Sensitivity studies on the impacts of Tibetan Plateau snowpack pollution on the Asian hydrological cycle and monsoon climate, At-

mos. Chem. Phys., 11, 1929–1948, https://doi.org/10.5194/acp-11-1929-2011, 2011.

Qian, Y., Yasunari, T. J., Doherty, S. J., Flanner, M. G., Lau, W. K. M., Ming, J., Wang, H., Wang, M., Warren, S. G., and Zhang, R.: Light-absorbing particles in snow and ice: Measurement and modeling of climatic and hydrological impact, Adv. Atmos. Sci., 32, 64–91, https://doi.org/10.1007/s00376-014-0010-0, 2014.

Rhodes, J. J., Armstrong, R. L., and Warren, S. G.: Mode of formation of "ablation hollows" controlled by dirt content of snow, J. Glaciol., 33, 135–139, 1987.

Roy, A., Royer, A., Montpetit, B., Bartlett, P. A., and Langlois, A.: Snow specific surface area simulation using the one-layer snow model in the Canadian LAnd Surface Scheme (CLASS), The Cryosphere, 7, 961–975, https://doi.org/10.5194/tc-7-961-2013, 2013.

Skiles, S. M., Painter, T. H., Deems, J. S., Bryant, A. C., and Landry, C. C.: Dust radiative forcing in snow of the Upper Colorado River Basin: 2. Interannual variability in radiative forcing and snowmelt rates, Water Resour. Res., 48, W07522, https://doi.org/10.1029/2012WR011986, 2012.

Sterle, K. M., McConnell, J. R., Dozier, J., Edwards, R., and Flanner, M. G.: Retention and radiative forcing of black carbon in eastern Sierra Nevada snow, The Cryosphere, 7, 365–374, https://doi.org/10.5194/tc-7-365-2013, 2013.

Stier, P., Feichter, J., Kinne, S., Kloster, S., Vignati, E., Wilson, J., Ganzeveld, L., Tegen, I., Werner, M., Balkanski, Y., Schulz, M., Boucher, O., Minikin, A., and Petzold, A.: The aerosol-climate model ECHAM5-HAM, Atmos. Chem. Phys., 5, 1125–1156, https://doi.org/10.5194/acp-5-1125-2005, 2005.

Sturm, M., Goldstein, M. A., and Parr, C.: Water and life from snow: A trillion dollar science question, Water Resour. Res., 53, 3534–3544, https://doi.org/10.1002/2017WR020840, 2017.

Taillandier, A.-S., Domine, F., Simpson, W. R., Sturm, M., and Douglas, T. A.: Rate of decrease of the specific surface area of dry snow: Isothermal and temperature gradient conditions, J. Geophys. Res., 112, F03003, https://doi.org/10.1029/2006JF000514, 2007.

Toon, O. B., Mckay, C. P., and Ackerman, T. P.: Rapid Calculation of Radiative Heating Rates and Photodissociation Rates in Inhomogeneous Multiple Scattering Atmospheres, J. Geophys. Res., 94, 16287–16301, 1989.

van der Werf, G. R., Randerson, J. T., Giglio, L., Collatz, G. J., Mu, M., Kasibhatla, P. S., Morton, D. C., DeFries, R. S., Jin, Y., and van Leeuwen, T. T.: Global fire emissions and the contribution of deforestation, savanna, forest, agricultural, and peat fires (1997–2009), Atmos. Chem. Phys., 10, 11707–11735, https://doi.org/10.5194/acp-10-11707-2010, 2010.

Wang, X., Doherty, S. J., and Huang, J.: Black carbon and other light-absorbing impurities in snow across Northern China, J. Geophys. Res.-Atmos., 118, 1471–1492, https://doi.org/10.1029/2012JD018291, 2013.

Warren, S. G. and Wiscombe, W. J.: A Model for the Spectral Albedo of Snow. II: Snow Containing Atmospheric Aerosols, J. Atmos. Sci., 37, 2734–2745, 1980.

Weedon, G. P., Balsamo, G., Bellouin, N., Gomes, S., Best, M. J., and Viterbo, P.: The WFDEI meteorological forcing data set: WATCH Forcing Data methodology applied to ERA-Interim reanalysis data, Water Resour. Res., 50, 7505–7514, https://doi.org/10.1002/2014WR015638, 2014.

Westergren, M.: Performance evaluation of regional calibration methods for a distributed hydrologic modeling framework, Master's thesis, University of Oslo, available at: https://www.duo.uio.no/handle/10852/53238, last access: 19 October 2016.

Winstral, A. and Marks, D.: Simulating wind fields and snow redistribution using terrain-based parameters to model snow accumulation and melt over a semi-arid mountain catchment, Hydrol. Process., 16, 3585–3603, https://doi.org/10.1002/hyp.1238, 2002.

Wiscombe, W. J. and Warren, S. G.: A Model for the Spectral Albedo of Snow. I: Pure Snow, J. Atmos. Sci., 37, 2712–2733, 1980.

Xu, B., Cao, J., Joswiak, D. R., Liu, X., Zhao, H., and He, J.: Post-depositional enrichment of black soot in snow-pack and accelerated melting of Tibetan glaciers, Environ. Res. Lett., 7, 014022, https://doi.org/10.1088/1748-9326/7/1/014022, 2012.

Zhang, K., O'Donnell, D., Kazil, J., Stier, P., Kinne, S., Lohmann, U., Ferrachat, S., Croft, B., Quaas, J., Wan, H., Rast, S., and Feichter, J.: The global aerosol-climate model ECHAM-HAM, version 2: sensitivity to improvements in process representations, Atmos. Chem. Phys., 12, 8911–8949, https://doi.org/10.5194/acp-12-8911-2012, 2012.

Paper III

Matt, F. N., Burkhart, J. F. (2018): Assessing satellite derived radiative forcing from snow impurities through inverse hydrologic modelling, *Geophysical Research Letters, 45, 3531-3541*, doi:10.1002/2018GL077133.

AGU100 ADVANCING EARTH AND SPACE SCIENCE

Geophysical Research Letters

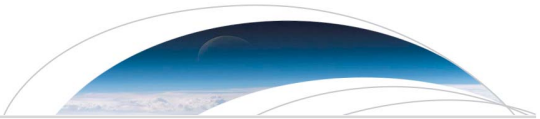

RESEARCH LETTER
10.1002/2018GL077133

Assessing Satellite-Derived Radiative Forcing From Snow Impurities Through Inverse Hydrologic Modeling

F. N. Matt[1] and J. F. Burkhart[1,2]

[1]Department of Geosciences, University of Oslo, Oslo, Norway, [2]Statkraft AS, Oslo, Norway

Key Points:
- A new method for comparing light-absorbing impurities in snow and ice (LAISI) radiative forcing from models and satellites is introduced
- Potential impacts of LAISI on snowmelt for Himalayan water resources are investigated
- LAISI radiative forcing impacts on streamflow generation are estimated at the catchment scale

Supporting Information:
- Supporting Information S1

Correspondence to:
F. N. Matt,
f.n.matt@geo.uio.no

Citation:
Matt, F. N., & Burkhart, J. F. (2018). Assessing satellite-derived radiative forcing from snow impurities through inverse hydrologic modeling. *Geophysical Research Letters*, *45*, 3531–3541. https://doi.org/10.1002/2018GL077133

Received 15 JAN 2018
Accepted 30 MAR 2018
Accepted article online 19 APR 2018
Published online 26 APR 2018

Abstract Light-absorbing impurities in snow and ice (LAISI) lower the snow albedo and cause accelerated snowmelt. The radiative forcing caused by LAISI is in this connection the key variable in understanding LAISI-snowpack dynamics. Here we present an approach combining distributed hydrologic model simulations and remotely sensed radiative forcing from LAISI in order to improve model predictions of radiative forcing impacts. In a case study, we assess the seasonal cycle of instantaneous at-surface clear-sky radiative forcing from LAISI as predicted by model and satellite observations for a river basin located at the southern slope of the Himalayas. By scaling dust depositions, we optimize simulated radiative forcing conditioned on satellite observations. The optimized model predicts that LAISI-induced radiative forcing in snow contributes to 4.1% to 5.8% of the annual discharge. The presented approach has a wide range of applications as it provides a novel method to constrain and evaluate measures of LAISI-induced radiative forcing.

Plain Language Summary Certain particles that have the ability to absorb sunlight deposit onto mountain snow via atmospheric transport mechanisms. The presence of such particles in snow leads to a reduction of the snow's ability to reflect sunlight, which increases snowmelt. The key variable to understand these processes is hereby the additional energy that is taken up by the snow due to the presence of these particles. In this study, we present a method that allows the comparison of this additional energy measured by satellites with those predicted by numerical models. In a case study, we use the satellite data to improve the model representation of this variable by adapting the amount of particles in the snow of an area located at the southern slope of the Himalayas. Using the improved model, we estimate the increase in streamflow resulting from increased snowmelt in the area. We find that in the study region, light-absorbing particles in snow are responsible for 4.1% to 5.8% of the annual streamflow.

1. Introduction

Light-absorbing impurities in snow and ice (LAISI) can increase snowmelt (Skiles et al., 2012), shorten snow cover (Painter et al., 2007), and alter the hydrologic cycle (Qian et al., 2011) resulting from modifications to snow albedo. Inclusion of LAISI in physically based snow albedo models improves the representation of this sensitive and dynamic variable and modifies snow metamorphism (Tuzet et al., 2017). Models of different scales consider the effects of LAISI, ranging from multilayer point models (Tuzet et al., 2017), hydrologic catchment models (Matt et al., 2018), to regional (Oaida et al., 2015) and global (Flanner et al., 2007) climate models.

LAISI in surface snow lead to increased energy uptake by the snowpack, so-called radiative forcing in snow (RFS). RFS is the key variable in determining LAISI impacts. However, it remains a challenge to asses model predictions of RFS. Most studies compare the simulated LAISI content in surface snow layers against observations, which illustrates the models' ability to predict mixing ratios of LAISI from aerosol deposition and post depositional dynamics (e.g., Flanner et al., 2007; Ménégoz et al., 2014; Qian et al., 2011, 2014; Zhao et al., 2014). From this it is then assumed that a good estimate of the LAISI mixing ratios in surface snow reflects the model's ability to simulate RFS. Though reasonable estimates of surface mixing ratios of LAISI may be a necessity to determine RFS, it is not a sufficiency: the model representation of surface snow (Matt et al., 2018), optical grain radius (OGR) of the snow (Warren & Wiscombe, 1980), and irradiance characteristics (Wiscombe & Warren, 1980) play an essential role. However, observations of all variables required to conduct a complete evaluation of model predictions are rare and often discontinuous in time and space.

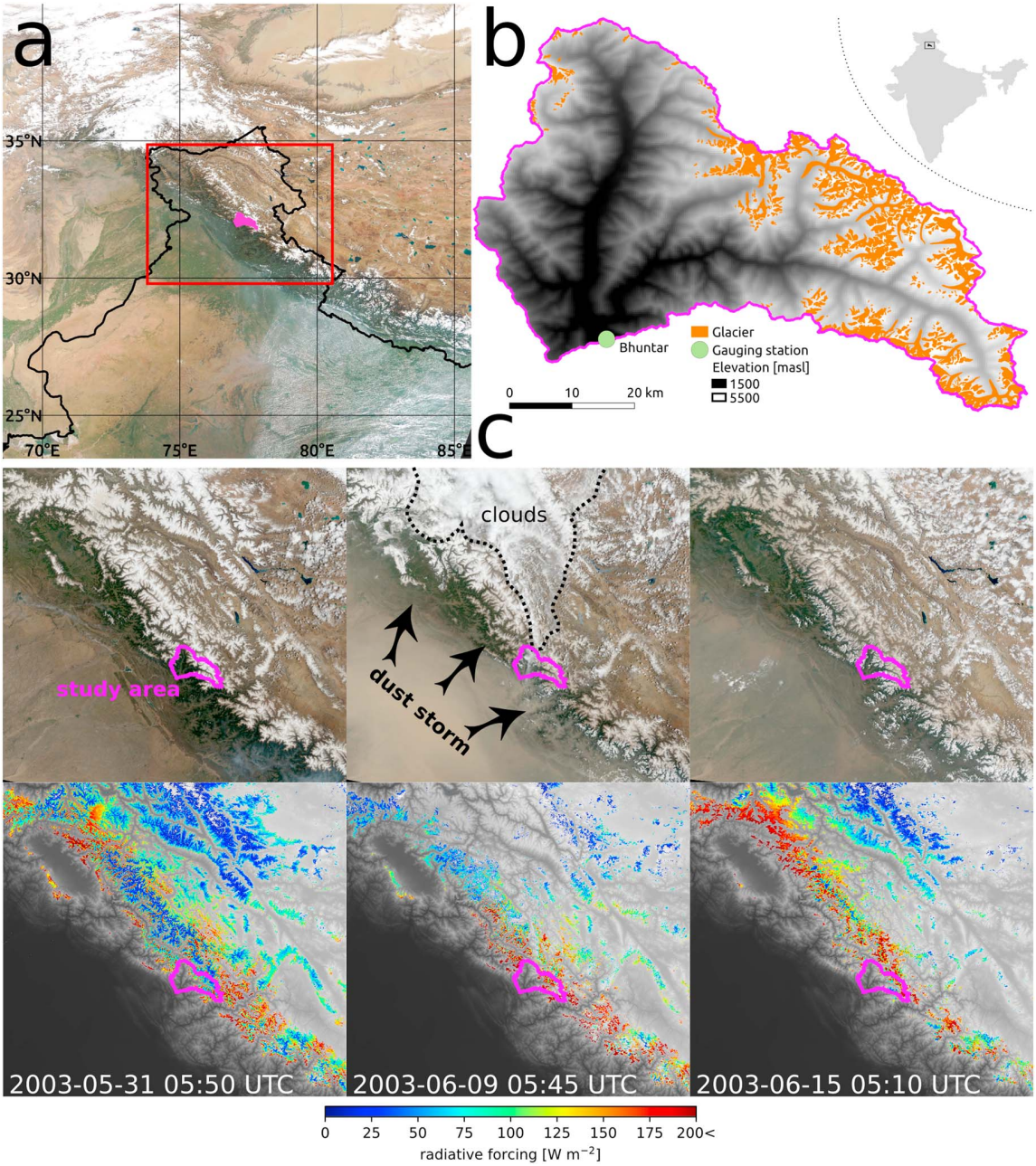

Figure 1. (a) Overview map showing the location of the Upper Beas Basin (magenta) in the western Himalayas. The red box marks the area shown in (c). The black lines mark the country boarders of India. (b) Upper Beas Basin. (c) True color Moderate Resolution Imaging Spectroradiometer (MODIS) images (top row) showing the western Himalayas before, during, and after a dust event in May/June 2003. The corresponding instantaneous radiative forcing in snow predicted by the MODIS Dust Radiative Forcing in Snow algorithm is shown in the bottom row.

On the other hand, continuous observations are required due to strong temporal fluctuations in the surface mixing ratios and subsequent RFS, driven by post depositional redistribution of LAISI in the snowpack (Matt et al., 2018; Qian et al., 2014). These dynamics, and in particular the role of LAISI transport and removal from the snowpack with percolating meltwater (Doherty et al., 2013, 2016; Sterle et al., 2013; Xu et al., 2012), are still poorly understood (Lazarcik et al., 2017). For all these reasons, simulations including LAISI would benefit from a direct evaluation of the model's ability to predict RFS.

RFS can be determined without knowledge of vertical distribution and composition of LAISI by measuring snow albedo and relating it to the albedo of hypothetically clean snow with the same OGR. Painter et al. (2012) introduced a new algorithm that enables the retrieval of RFS from the Moderate Resolution Imaging Spectroradiometer (MODIS) surface reflectance data, which may be used to directly assess model performance in the simulation of RFS. However, challenges arise when comparing instantaneous satellite products with simulations at hourly or daily temporal frequency, and significant variability may exist that MODIS may not adequately capture (Burkhart et al., 2017).

Here we introduce an inverse modeling approach allowing the comparison of simulated instantaneous clear-sky RFS from LAISI to observations from the MODIS Dust Radiative Forcing in Snow algorithm (MODDRFS; Painter et al., 2012). We apply the approach to a western Himalayan catchment that is heavily impacted by dust deposition (Gautam et al., 2013) (see Figure 1 showing satellite scenes prior and posterior to a dust storm over the study area). Utilizing catchment discharge data from a region in the Himalayas for which MODDRFS is available (Figure 1c) and for which we believe significant dust and black carbon (BC) deposition will impact RFS, we conduct hydrologic simulations to derive snowpack properties. Atmospheric transport simulations provide BC aerosol deposition, while dust deposition is scaled in order to optimize model predictions of RFS toward the satellite observations. In this manner we are able to assess the impacts of RFS on discharge generation as well as derive an improved understanding of the magnitude of dust deposition for the region.

2. Study Location and Meteorological Forcing

The study region is the Upper Beas Basin, located at the southern slope of the western Himalayas, Himachal Pradesh, India (Figure 1a). Only the headwater basin above Bhuntar station is used (Figure 1b) due to lower impact of seasonal snow cover and significant hydroelectric activity further downstream (Li et al., 2015). The study basin covers an area of approximately 3,200 km^2, of which about 13% is glacier covered. Elevation varies between 1,055 and over 6,000 masl. The local climate is dominated from a combination of elevation effect, extratropical cyclones in winter, and summer monsoon activity. Meteorological forcing for the hydrological model include daily mean 2-m air temperature, precipitation, relative humidity, wind speed, and global radiation. Limited meteorological observations are available for the study area and time. We chose to dynamically downscale ERA-Interim data (Dee et al., 2011) from the European Centre for Medium Range Weather Forecasts using the Weather Research and Forecasting Model (version 3.8.1; Skamarock et al., 2008). Our decision to use dynamically downscaled reanalysis data as model forcing data rather than meteorological observations is based on a simple model experiment. We found that hydrologic simulations perform equivalent to other studies when using observations as input (Hegdahl et al., 2016; Li et al., 2015) yet significantly better when using dynamically downscaled reanalysis data (see supporting information for details; Diggle & Ribeiro, 2007; Engelhardt et al., 2017).

3. Approach

Figure 2 introduces our methodology which provides a concurrent instantaneous RFS calculation for direct comparison with MODDRFS (Painter et al., 2012). As the satellite product provides an instantaneous response, simulated RFS (hereinafter RFS_{sim}) of LAISI must be calculated with contemporaneous solar radiative conditions to the MODIS overpass. To estimate snowpack variables required to determine RFS_{sim} at MODIS overpass times, we use an inverse hydrologic modeling approach. That is, we estimate model parameters by optimizing regional simulated streamflow constrained by observed streamflow, in order to develop snowpack properties used for the subsequent simulations of RFS_{sim}.

The approach initiates with the development of an aerosol deposition scenario for our study region (Figure 2-A). This scenario provides input for a catchment-scale hydrologic model coupled to the Snow, Ice, and Aerosol Radiation (SNICAR) model (Flanner et al., 2007, 2009). The model includes a dynamic snow albedo calculation considering LAISI (Figure 2-1; details can be found in Matt et al., 2018). Using an optimized set of parameters, we derive snow properties for the region on a daily time scale. The snowpack properties from the regional hydrologic model are then used as input to a stand-alone version of SNICAR. Next, simulated snow albedos are used in combination with solar irradiances at MODIS overpass times in order to estimate the broadband RFS_{sim} (Figure 2-2) suitable for comparison with MODDRFS (Figure 2-3). We then iterate through

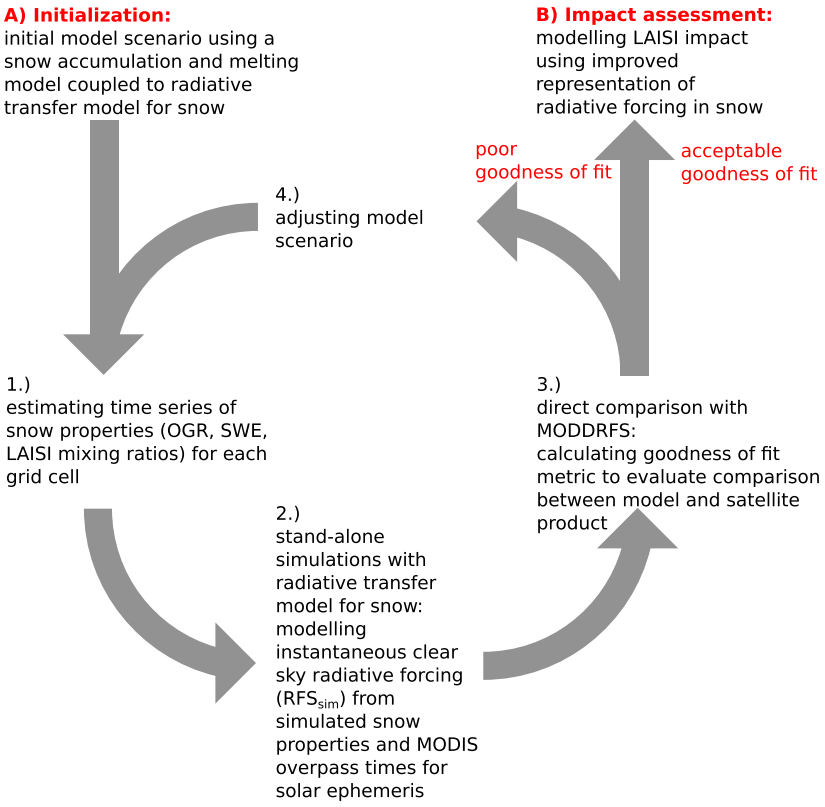

Figure 2. Methodology overview.

our model chain, scaling dust deposition (Figure 2-4) until an optimized fit is achieved between the MODDRFS product and RFS_{sim}. Our approach ultimately allows us to evaluate dust deposition and estimate impacts on streamflow using the optimized LAISI representation (Figure 2-B).

Details of each sequence of the model chain (step 1. to 4. in Figure 2) are provided in the following.

3.1. Coupled Snow/Hydrologic Model

Matt et al. (2018) introduced a snowpack routine within a catchment-scale hydrologic model that allows for the input of wet and dry deposition of light-absorbing aerosols, in addition to standard meteorological forcing variables. The model uses a two-layer energy balance-based snow algorithm coupled to the SNICAR model (Flanner et al., 2007, 2009), which accounts for the reduction in albedo due to LAISI. SNICAR determines snow albedo from the modeled mixing ratios of LAISI in the snow layers, the modeled OGR, and the incoming solar flux characteristics.

Model parameters of the hydrologic model are estimated using automatic model calibration with the Bound Optimization BY Quadratic Approximation algorithm for bound constrained optimization (Powell, 2009). Simulated and observed streamflow are used to quantify model performance (see supporting information for model parameters and model performance measures; Nash & Sutcliffe, 1970). The model is then run at a daily time step over a 6-year period (October 1999 to September 2005) in order to estimate per-grid cell daily time series of the snow properties: OGR, snow water equivalent of surface and bottom layer, and mixing ratios of LAISI in both layers (Figure 2-1).

3.2. Modeled Instantaneous Clear-Sky Radiative Forcing

In the second processing step (Figure 2-2), the snow properties developed in the first step are used as input to a stand-alone version of the SNICAR model. For each grid cell the albedo time series of clean snow (all LAISI mixing ratios set to 0) and LAISI-polluted snow (with LAISI mixing ratios from the first step) at MODIS overpass times are determined. This allows the determination of the *instantaneous* RFS_{sim} *at MODIS overflight times*, which is required for comparison with MODDRFS. The MODIS time of acquisition and the solar

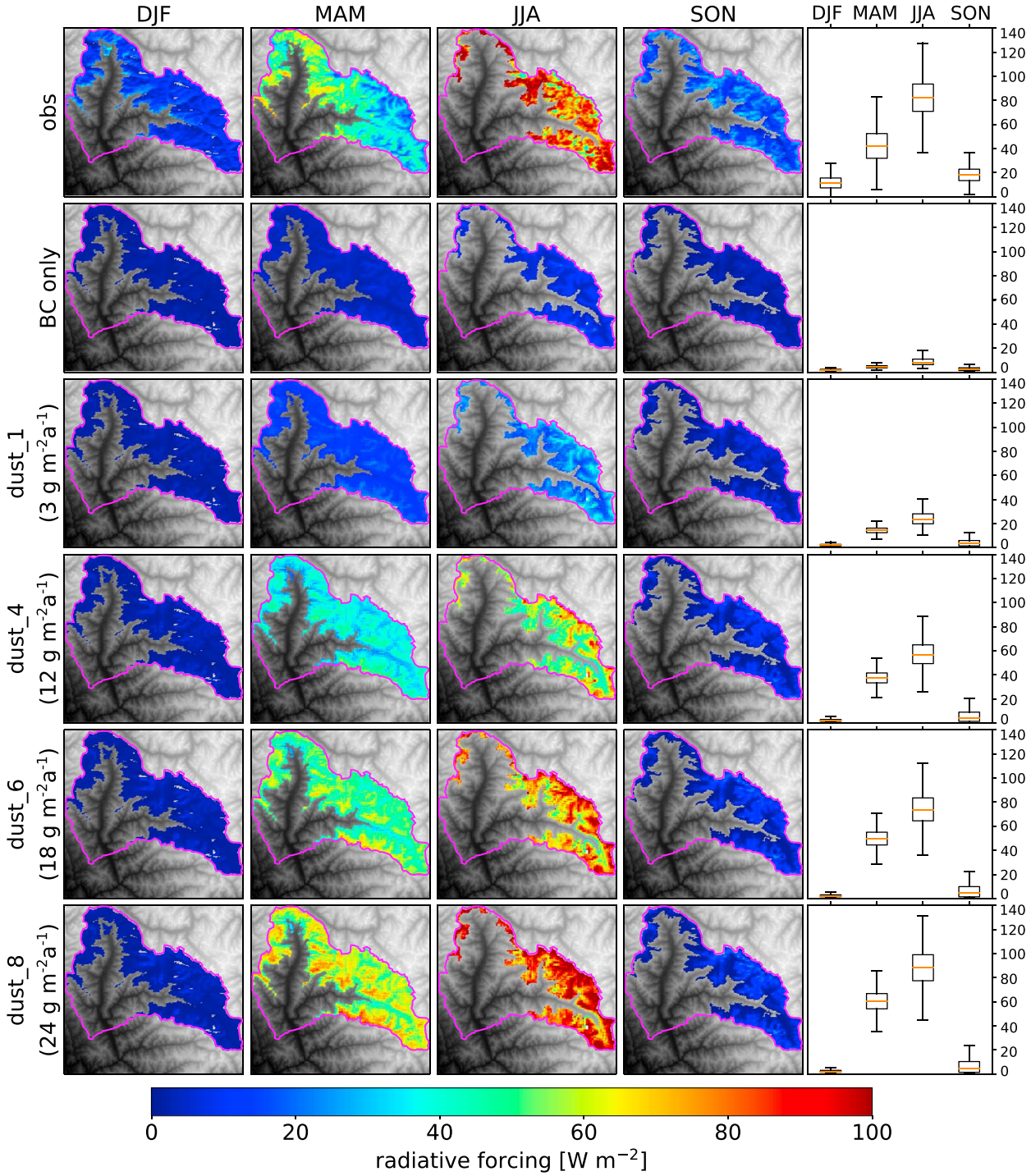

Figure 3. Seasonal mean per-pixel instantaneous radiative forcing from MODIS Dust Radiative Forcing in Snow algorithm observations (row 1) and model simulations using different light-absorbing impurities in snow and ice scenarios (rows 2 to 6). DJF = December, January, February; MAM = March, April, May; JJA = June, July, August; SON = September, October, November.

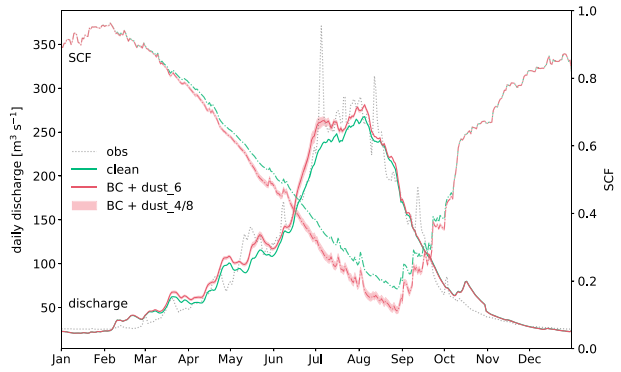

Figure 4. Daily discharge and snow-covered fraction (SCF) averaged over the 6-year study period for the dust_6 scenario (red curve; 18 g·m^{-2}·a^{-1} dust deposition) and the scenario ignoring radiative forcing in snow by light-absorbing impurities in snow and ice ("clean"; green curve). The red shaded area shows the difference between the dust_4 (12 g·m^{-2}·a^{-1}) and dust_8 (24 g·m^{-2}·a^{-1}) scenarios used to estimate light-absorbing impurities in snow and ice radiative forcing impact uncertainty. BC = black carbon; OBS = observations.

ephemeris were determined using the NASA LaRC Satellite Overpass Predictor (https://www-air.larc.nasa.gov/tools.htm). In order to be consistent with the MODDRFS product, we estimate the per-grid cell instantaneous clear-sky RFS using spectral irradiances calculated with the same model configuration as for MODDRFS. Accordingly, local clear-sky radiative conditions for each grid cell at the time of acquisition are modeled using the Santa Barbara DISORT Atmospheric Radiative Transfer model (Ricchiazzi et al., 1998) in conjunction with the 3 arc second Shuttle Radar Topography Mission digital elevation model. In this manner, the approach eliminates differences coming from the radiative transfer model for the atmosphere used in our approach and MODDRFS, and a direct "apples to apples" comparison of RFS_{sim} from the regional hydrologic model with MODDRFS is achieved.

In the same manner as MODDRFS, topographic radiation correction is applied to direct and diffuse incident spectral irradiances. The irradiances are first determined at 1/5th grid cell spatial resolution and then upscaled to mean per-grid cell spectral irradiances. Terrain-corrected irradiances $E_{\text{corrected},\lambda}$ are calculated as

$$E_{\text{corrected},\lambda} = \cos\beta \cdot E_{\text{direct},\lambda} + E_{\text{diffuse},\lambda}, \tag{1}$$

where $E_{\text{direct},\lambda}$ and $E_{\text{diffuse},\lambda}$ are the direct and diffuse irradiances at wavelength λ and β is the grid cell local solar zenith angle, determined as

$$\cos\beta = \cos\theta_s \cos\theta_n + \sin\theta_s \sin\theta_n \cos(\phi_s - \phi_n). \tag{2}$$

The θ_s is the solar zenith angle for a level surface, ϕ_s is the solar azimuth angle, θ_n is the surface slope angle, and ϕ_n is the surface aspect angle (Painter et al., 2012).

The irradiances are first modeled on a continuous spectrum of 0.001 μm. We then integrate the irradiances to the SNICAR bands 1 (0.3 to 0.7 μm) and 2 (0.7 to 1.0 μm), to be comparable with MODDRFS (0.350 to 0.876 μm). Instantaneous clear-sky RFS_{sim} at MODIS overpass times is then retrieved as

$$F = \sum_{i=1}^{2} E_{\text{corrected},i}(\alpha_{\text{clean},i} - \alpha_{\text{polluted},i}), \tag{3}$$

where i is the SNICAR band number. $\alpha_{\text{clean},i}$ and $\alpha_{\text{polluted},i}$ are the band-specific direct beam albedos for clean and polluted snow. Using the 470 bands version of SNICAR (0.01-μm spectral resolution) and various combinations of input data (impurity content, OGR, solar zenith angle, and solar irradiances) representative for the study region, we found that radiative forcing modeled for the 0.3- to 1.0-μm spectrum used in our approach is 10.4 ± 1.9% larger than for the 0.35- to 0.876-μm spectrum used in MODDRFS. We account for this positive bias by introducing a correction factor, c, so that RFS_{sim} corrected for the band mismatch is

$$F_c = c * F, \tag{4}$$

with $c = 0.906$ being specific for the study region. The corrected RFS_{sim} is then used in the comparison with MODDRFS.

A summary of the methods used for MODDRFS retrieval and our model approach is given in supporting information (Brun, 1989; Taillandier et al., 2007).

3.3. Comparison of MODDRFS With Simulated RFS

To compare MODDRFS with our model results, the RFS_{sim} is spatially downscaled from the model grid resolution (1 km) to the MODDRFS pixels (~ 300 m). Only pixels where both MODDRFS and RFS_{sim} have valid RFS values are selected. For MODDRFS a certain pixel must have a value in the range 0 to 400 W/m^2, while the

RFS_{sim} values are considered only if the corresponding snow cover of a pixel is equal or larger than 90%. Valid values are grouped according to a certain time criteria (e.g., month of year or season of year) and per-pixel mean values calculated. Due to the high number of missing values in the MODDRFS product and the very short snow cover in pixels at lower elevations, we introduce a minimum number of values per grouping that are required in order to calculate the mean value for the respective pixel. If this criteria is not fulfilled, the pixel is excluded from the comparison. Mean pixel values constitute the basis for the metric used to compare clear-sky RFS_{sim} with the remotely sensed MODDRFS product. This refers to step 3 in Figure 2.

3.4. Adjusting Model Scenario

We account for BC and dust in our simulations. Wet and dry deposition rates of BC are modeled with the Flexible Particle Dispersion Model (Stohl et al., 1998, 2005; Stohl & Thomson, 1999; details given in supporting information; Amann et al., 2011; Doherty et al., 2014; Klimont et al., 2017; Stohl et al., 2015; van der Werf et al., 2010). Dust deposition rates estimated with atmospheric transport models are highly uncertain due to potentially high contribution from local or regional sources not resolved by the model (Ginot et al., 2014; Ménégoz et al., 2014). For this reason, we apply a simple dust deposition scenario based on quantitative observations and then attempt to improve model projections of RFS by scaling dust depositions (step 4 in Figure 2) and reevaluate steps 1 to 3 of Figure 2. In this way, we optimize RFS_{sim} toward MODDRFS with the aim to improve LAISI impact estimates (Figure 2-B).

In our study area, dust storms are mainly occurring during the premonsoon period (March to June), when westerly winds advect desert dust from Southwest Asia and the Thar desert into the Indo-Ganges planes, with occasional outbreaks over the southern side of the Himalayas (Duchi et al., 2014; Gautam et al., 2011, 2013; Hegde et al., 2007; Prasad & Singh, 2007). Estimates of the annual deposition flux are rare and mainly exist from snowpit and ice core measurements (e.g., Ginot et al., 2014; Xu et al., 2016, 2014). Closest to the study region (Jiemayangzong glacier, Southwest Tibet) dust deposition is about 3.0 $g \cdot m^{-2} \cdot a^{-1}$ (Xu et al., 2016). Further estimates from the southern Himalayas are given from Mera Glacier (Nepal) and are about 10.4 $g \cdot m^{-2} \cdot a^{-1}$ (Ginot et al., 2014). Size distributions peak at around 6 μm (Ginot et al., 2014); wherefore, we use dust optical properties accounting for dust with a diameter of 5 – 10 μm.

Due to the predominant dust deposition during premonsoon, we add dust to the surface layer on a daily basis during March to June, so that the daily added amount is constant and the annual sum has a magnitude consistent with the observed annual depositions. As shown later, aiming for 3 $g \cdot m^{-2} \cdot a^{-1}$ (dust_1 scenario) results in strong underestimation of RFS. We therefore scale dust depositions to multiples of this initial deposition scenario, where the multiplication factor is given in the scenario name (i.e., dust_2 scenario aims for 6 $g \cdot m^{-2} \cdot a^{-1}$ and dust_3 for 9 $g \cdot m^{-2} \cdot a^{-1}$). The highest annual dust deposition included in the analysis is 24 $g \cdot m^{-2} \cdot a^{-1}$ (dust_8). By adding a daily amount of dust to the snow surface, we acknowledge that we are unable to account for the episodic nature of dust events. Implications from this are discussed in section 4.2.

4. Results and Discussion

4.1. From Satellite Observations to Impact Estimates

An optimization of modeled LAISI RFS (RFS_{sim}) toward satellite observations (MODDRFS) is achieved by scaling dust depositions (see Figure 3). The upward scaling of dust leads to a better representation of the seasonal cycle of RFS shown in the observations (row 1 of graphs in Figure 3), which comes from a combination of different processes that cause an increase in RFS from LAISI during spring (March, April, May) and summer (June, July, August): stronger solar irradiation toward summer, increase in OGR due to accelerated snow metamorphism in melting snow and thus more effective absorption of solar radiation by LAISI (Warren & Wiscombe, 1980), and LAISI accumulation in the snow surface during snowmelt (Doherty et al., 2013, 2016; Xu et al., 2012). RFS_{sim} is underestimated during winter months (December, January, February) regardless of the applied dust scenario. The underestimation is likely to come from an underestimation of OGR or an underestimation of LAISI in surface snow or a combination of both. However, we do not expect large implications from the winter underestimation of RFS for the impact estimate on discharge due to generally low streamflow during winter (Figure 4). Using the root-mean-square error E_{RMS} (e.g., Bennett et al., 2013) of basin mean monthly RFS as evaluation metric, an annual dust deposition of 18 $g \cdot m^{-2} \cdot a^{-1}$ (dust_6 scenario) gives the best results (see supporting information for a complete overview of results). We further include the dust_4 (12 $g \cdot m^{-2} \cdot a^{-1}$; general underestimation of LAISI RFS) and dust_8 (24 $g \cdot m^{-2} \cdot a^{-1}$; general overestimation) scenarios to quantify the uncertainty of model projections. Even though the optimized dust depositions are exceeding

the amount of the nearest observed deposition flux (3 $g \cdot m^{-2} \cdot a^{-1}$; Xu et al., 2016) by a factor of 4 to 8 within these uncertainties, we believe that our estimate is realistic due to much shorter distances of our study region to major dust sources such as the Thar Desert and the location at the southern slopes of the Himalayas, which is particularly prone to dust events (e.g., Gautam et al., 2013).

The optimized RFS simulation allows to estimate the LAISI impact on hydrologic variables (Figure 4). On average, LAISI lead to significantly higher discharge from about middle March to end of August. For the rest of the year, no significant difference in discharge is noticeable. Results show on average a maximum absolute increase in discharge of 33.8 m^3/s (26.0 to 40.6 m^3/s), occurring in all scenarios in the beginning of July. Accordingly, LAISI account at maximum for 13.4% (10.6% to 15.6%) of the daily discharge. Considering the whole study period, LAISI account for about 5.0% (4.1% to 5.8%) of the annually generated discharge. The snow-covered fraction (SCF) in the catchment decreases faster during the melt period in scenarios accounting for LAISI, leading to a SCF reduction of 0.065 (0.053 to 0.074) at snow cover minimum in summer. The annual mean SCF is reduced by 0.023 (0.018 to 0.026). The increasing effect on discharge throughout spring and summer is distinct from other studies, where a shift in the annual water balance is observed with increasing discharge during spring melt season and decrease of discharge later in the season (Matt et al., 2018; Painter et al., 2010; Qian et al., 2011). In contrast to the aforementioned studies, our study region shows permanent snow cover due to the high altitude and glaciers. This allows streamflow contribution from snowmelt throughout the year, whereas in seasonally snow covered regions, increased streamflow due to LAISI is limited to the early melt season.

4.2. Uncertainties

Our study exemplifies how remotely sensed instantaneous LAISI RFS can be integrated alongside model simulations with the aim to evaluate and improve model predictions. We hereby lay particular focus on eliminating differences coming from the radiative transfer model for the atmosphere used in our approach and MODDRFS. We then expect discrepancies between simulations and satellite data to mainly originate from the LAISI representation in the model. Uncertainties in the satellite data come from known limitations associated with atmospheric correction, detection of snow properties, and bare ground contamination at the subpixel scale (Painter et al., 2012). To date, ground evaluation of MODDRFS is only available for the Colorado Mountains. We therefore claim that evaluation of MODDRFS in interest regions such as Himalayas, Tibetan plateau, and the Andes is of great importance in order to gain more insight in the accuracy of the satellite product. For the Upper Colorado River Basin, Painter et al. (2012) state a high bias for low values of MODDRFS and a low bias for high values. These findings are consistent with the likelihood that MODIS inherently smooths subpixel variability (Burkhart et al., 2017). Yet as the magnitude of those biases may be regionally specific, we did not apply the bias correction to MODDRFS prior to the case study. However, assuming an analogous tendency in the bias and the predominantly high RFS values during snowmelt (Figure 3), we consider our impact estimate to be conservative. In addition, we expect an uncertainty of about $\pm 1.6\%$ on the corrected RFS_{sim} due to the mismatch in spectral bands used in the radiative transfer model for snow of our model and the MODDRFS algorithm. The uncertainty is estimated using the 470 bands version of SNICAR and various input data combinations representative for conditions in the study region.

By depositing a daily amount of dust to the snow surface during the premonsoon period, we acknowledge that our deposition scenarios potentially differ significantly from real deposition rates both at spatial and temporal scales. Especially the event based, episodic nature of dust depositions (Duchi et al., 2014; Gautam et al., 2011; Hegde et al., 2007) may have implications for the model representation of dust in the surface layer. Improving the spatial and temporal representation of the dust deposition scenario has the potential to improve model predictions of LAISI RFS and impact estimates. Development of such scenarios was not in the scope of this study; however, recent advances in the field of atmospheric dust transport and deposition modeling could provide scenarios enabling this to be addressed in future studies.

5. Potential Applications and Outlook

The impact of LAISI on cryospheric regions has caught the attention of scientists and policymakers due to the significant role in accelerating glacier melt (Gabbi et al., 2015; Xu et al., 2012), altering hydrologic processes (Matt et al., 2018; Qian et al., 2011), and climate forcing (Flanner et al., 2007). However, the techniques to assess model predictions on all scales are limited. The herein provided method is a significant contribution as it provides a further metric of evaluation for LAISI impacts in addition to the established and widely used

comparison between simulated and observed mixing ratios in surface snow. We used the herein presented method in order to optimize model representation of LAISI RFS by scaling dust deposition and to asses the impact on the hydrological cycle using a hydrological model. Likewise, the method can be applied to evaluate model predictions of LAISI RFS of models on different scales. Numerous model studies evaluate surface mixing ratios of LAISI and give an estimate of their radiative impact based on this evaluation (e.g., Flanner et al., 2007; Ménégoz et al., 2014; Qian et al., 2014, 2011; Zhao et al., 2014). Due to the impact of many other variables on RFS, such as OGR and incident radiation properties, we argue that those studies can greatly benefit from including benchmarking tests against the MODDRFS product. In future applications the method described herein can be used as follows:

1. To validate model products aiming for the quantification of LAISI RFS on scales ranging from global, regional, to point models.
2. To improve impact assessments of LAISI on snowmelt, discharge generation, and glacier melt in various regions of the world.

Such comparisons require reliable satellite data of instantaneous RFS. For this reason, we also suggest an in-depth assessment of the regional quality of MODDRFS, which was not in the scope of the study presented herein.

Acknowledgments
This work was conducted within the Norwegian Research Council's INDNOR program under the HyCAMP project (NFR 222195) with support from the strategic research group LATICE (Faculty of Mathematics and Natural Sciences, University of Oslo). We thank Trude Eidhammer from NCAR for providing the WRF configuration files and Sabine Eckhardt from NILU for input on the black carbon emissions used for the FLEXPART modeling. Computational and data storage resources were provided by NOTUR/NORSTORE projects NS9333K and NN9333K. We further thank Anaconda, Inc., for providing the open-source distribution of Python used in this study. Data processing was conducted with open-source Python tools, namely, SciPy/NumPy (van der Walt et al., 2011) and xarray (Hoyer & Hamman, 2017). The data used are listed in the references, tables, and supporting information. Model forcing data, model configuration files, and model output generated and used herein are published in Matt and Burkhart (2018).

References

Amann, M., Bertok, I., Borken-Kleefeld, J., Cofala, J., Heyes, C., Höglund-Isaksson, L., et al. (2011). Cost-effective control of air quality and greenhouse gases in Europe: Modeling and policy applications. *Environmental Modelling & Software*, *26*(12), 1489–1501. https://doi.org/10.1016/j.envsoft.2011.07.012

Bennett, N. D., Croke, B. F., Guariso, G., Guillaume, J. H., Hamilton, S. H., Jakeman, A. J., et al. (2013). Characterising performance of environmental models. *Environmental Modelling & Software*, *40*, 1–20. https://doi.org/10.1016/j.envsoft.2012.09.011

Brun, E. (1989). Investigation on wet-snow metamorphims in respect of liquid water content. *Annals of Glaciology*, *13*, 22–26. https://doi.org/10.3189/S0260305500007576

Burkhart, J., Kylling, A., Schaaf, C. B., Wang, Z., Bogren, W., Storvold, R., et al. (2017). Unmanned aerial system nadir reflectance and MODIS nadir BRDF-adjusted surface reflectances intercompared over Greenland. *The Cryosphere*, *11*, 1575–1589. https://doi.org/10.5194/tc-11-1575-2017

Dee, D. P., Uppala, S. M., Simmons, A. J., Berrisford, P., Poli, P., Kobayashi, S., et al. (2011). The ERA-interim reanalysis: Configuration and performance of the data assimilation system. *Quarterly Journal of the Royal Meteorological Society*, *137*(656), 553–597. https://doi.org/10.1002/qj.828

Diggle, P. J., & Ribeiro, P. J. (2007). *Model-based geostatistics, Springer Series in Statistics*. New York USA: Springer. https://doi.org/10.1007/978-0-387-48536-2

Doherty, S. J., Bitz, C. M., & Flanner, M. G. (2014). Biases in modeled surface snow BC mixing ratios in prescribed-aerosol climate model runs. *Atmospheric Chemistry and Physics*, *14*(21), 11,697–11,709. https://doi.org/10.5194/acp-14-11697-2014

Doherty, S. J., Grenfell, T. C., Forsström, S., Hegg, D. L., Brandt, R. E., & Warren, S. G. (2013). Observed vertical redistribution of black carbon and other insoluble light-absorbing particles in melting snow. *Journal of Geophysical Research: Atmospheres*, *118*, 5553–5569. https://doi.org/10.1002/jgrd.50235

Doherty, S. J., Hegg, D. A., Johnson, J. E., Quinn, P. K., Schwarz, J. P., Dang, C., & Warren, S. G. (2016). Causes of variability in light absorption by particles in snow at sites in Idaho and Utah. *Journal of Geophysical Research: Atmospheres*, *121*, 4751–4768. https://doi.org/10.1002/2015JD024375

Duchi, R., Cristofanelli, P., Marinoni, A., Bourcier, L., Laj, P., Calzolari, F., et al. (2014). Synoptic-scale dust transport events in the southern Himalaya. *Aeolian Research*, *13*, 51–57. https://doi.org/10.1016/j.aeolia.2014.03.008

Engelhardt, M., Leclercq, P., Eidhammer, T., Kumar, P., Landgren, O., & Rasmussen, R. (2017). Meltwater runoff in a changing climate (1951–2099) at Chhota Shigri Glacier, Western Himalaya, Northern India. *Annals of Glaciology*, *58*, 47–58. https://doi.org/10.1017/aog.2017.13

Flanner, M. G., Zender, C. S., Hess, P. G., Mahowald, N. M., Painter, T. H., Ramanathan, V., & Rasch, P. J. (2009). Springtime warming and reduced snow cover from carbonaceous particles. *Atmospheric Chemistry and Physics*, *9*, 2481–2497. https://doi.org/10.1029/2005JD006356

Flanner, M. G., Zender, C. S., Randerson, J. T., & Rasch, P. J. (2007). Present-day climate forcing and response from black carbon in snow. *Journal of Geophysical Research*, *112*, D11202. https://doi.org/10.1029/2006JD008003

Gabbi, J., Huss, M., Bauder, A., Cao, F., & Schwikowski, M. (2015). The impact of Saharan dust and black carbon on albedo and long-term mass balance of an Alpine glacier. *The Cryosphere*, *9*(4), 1385–1400. https://doi.org/10.5194/tc-9-1385-2015

Gautam, R., Hsu, N. C., Lau, W. K.-M., & Yasunari, T. J. (2013). Satellite observations of desert dust-induced Himalayan snow darkening. *Geophysical Research Letters*, *40*, 988–993. https://doi.org/10.1002/grl.50226

Gautam, R., Hsu, N. C., Tsay, S. C., Lau, K. M., Holben, B., Bell, S., et al. (2011). Accumulation of aerosols over the Indo-Gangetic plains and southern slopes of the Himalayas: Distribution, properties and radiative effects during the 2009 pre-monsoon season. *Atmospheric Chemistry and Physics*, *11*, 12,841–12,863. https://doi.org/10.5194/acp-11-12841-2011

Ginot, P., Dumont, M., Lim, S., Patris, N., Taupin, J.-D., Wagnon, P., et al. (2014). A 10 year record of black carbon and dust from a Mera Peak ice core (Nepal): Variability and potential impact on melting of Himalayan glaciers. *The Cryosphere*, *8*, 1479–1496. https://doi.org/10.5194/tc-8-1479-2014

Hegdahl, T. J., Tallaksen, L. M., Engeland, K., Burkhart, J. F., & Xu, C.-Y. (2016). Discharge sensitivity to snowmelt parameterization: A case study for Upper Beas basin in Himachal Pradesh, India. *Hydrology Research*, *47*(4), 683–700. https://doi.org/10.2166/nh.2016.047

Hegde, P., Pant, P., Naja, M., Dumka, U. C., & Sagar, R. (2007). South Asian dust episode in june 2006: Aerosol observations in the central Himalayas. *Geophysical Research Letters*, *34*, L23802. https://doi.org/10.1029/2007GL030692

Hoyer, S., & Hamman, J. J. (2017). xarray: N-D labeled arrays and datasets in Python. *Journal of Open Research Software*, *5*(1), 10. https://doi.org/10.5334/jors.148

Klimont, Z., Kupiainen, K., Heyes, C., Purohit, P., Cofala, J., Rafaj, P., et al. (2017). Global anthropogenic emissions of particulate matter including black carbon. *Atmospheric Chemistry and Physics*, *17*, 8681–8723. https://doi.org/10.5194/acp-17-8681-2017

Lazarcik, J., Dibb, J. E., Adolph, A. C., Amante, J. M., Wake, C. P., Scheuer, E., et al. (2017). Major fraction of black carbon is flushed from the melting New Hampshire snowpack nearly as quickly as soluble impurities. *Journal of Geophysical Research: Atmospheres*, *122*, 537–553. https://doi.org/10.1002/2016JD025351

Li, H., Beldring, S., Xu, C.-Y., Huss, M., Melvold, K., & Jain, S. K. (2015). Integrating a glacier retreat model into a hydrological model—Case studies of three glacierised catchments in Norway and Himalayan region. *Journal of Hydrology*, *527*, 656–667. https://doi.org/10.1016/j.jhydrol.2015.05.017

Matt, F. N., & Burkhart, J. F. (2018). Datasets for "assessing satellite derived radiative forcing from snow impurities through inverse hydrologic modeling", Dataset. https://doi.org/10.5281/zenodo.1147967

Matt, F. N., Burkhart, J. F., & Pietikäinen, J.-P. (2018). Modelling hydrologic impacts of light absorbing aerosol deposition on snow at the catchment scale. *Hydrology and Earth System Sciences*, *22*(1), 179–201. https://doi.org/10.5194/hess-22-179-2018

Ménégoz, M., Krinner, G., Balkanski, Y., Boucher, O., Cozic, A., Lim, S., et al. (2014). Snow cover sensitivity to black carbon deposition in the Himalayas: From atmospheric and ice core measurements to regional climate simulations. *Atmospheric Chemistry and Physics*, *14*, 4237–4249. https://doi.org/10.5194/acp-14-4237-2014

Nash, J. E., & Sutcliffe, J. V. (1970). River flow forecasting through conceptual models. Part I: A discussion of principles. *Journal of Hydrology*, *10*(3), 282–290. https://doi.org/10.1016/0022-1694(70)90255-6

Oaida, C. M., Xue, Y., Flanner, M. G., Skiles, S. M., De Sales, F., & Painter, T. H. (2015). Improving snow albedo processes in WRF/SSiB regional climate model to assess impact of dust and black carbon in snow on surface energy balance and hydrology over western U.S.*Journal of Geophysical Research: Atmospheres*, *120*, 3228–3248. https://doi.org/10.1002/2014JD022444

Painter, T. H., Barrett, A. P., Landry, C. C., Neff, J. C., Cassidy, M. P., Lawrence, C. R., et al. (2007). Impact of disturbed desert soils on duration of mountain snow cover. *Geophysical Research Letters*, *34*, L12502. https://doi.org/10.1029/2007GL030284

Painter, T. H., Bryant, A. C., & Skiles, S. M. (2012). Radiative forcing by light absorbing impurities in snow from MODIS surface reflectance data. *Geophysical Research Letters*, *39*, L17502. https://doi.org/10.1029/2012GL052457

Painter, T. H., Deems, J. S., Belnap, J., Hamlet, A. F., Landry, C. C., & Udall, B. (2010). Response of Colorado River runoff to dust radiative forcing in snow. *Proceedings of the National Academy of Sciences of the United States of America*, *107*(40), 17,125–17,130. https://doi.org/10.1073/pnas.0913139107/-/DCSupplemental

Powell, M. (2009). The BOBYQA algorithm for bound constrained optimization without derivatives (Report NA2009/06, pp. 1–39). Cambridge, UK: Department of Applied Mathematics and Theoretical Physics, Centre for Mathematical Sciences.

Prasad, A. K., & Singh, R. P. (2007). Changes in Himalayan snow and glacier cover between 1972 and 2000. *Eos, Transactions American Geophysical Union*, *88*(33), 326. https://doi.org/doi:10.1029/2007EO330002

Qian, Y., Flanner, M. G., Leung, L. R., & Wang, W. (2011). Sensitivity studies on the impacts of Tibetan Plateau snowpack pollution on the Asian hydrological cycle and monsoon climate. *Atmospheric Chemistry and Physics*, *11*, 1929–1948. https://doi.org/10.5194/acp-11-1929-2011

Qian, Y., Wang, H., Zhang, R., Flanner, M. G., & Rasch, P. J. (2014). A sensitivity study on modeling black carbon in snow and its radiative forcing over the Arctic and Northern China. *Environmental Research Letters*, *9*, 64001. https://doi.org/10.1088/1748-9326/9/6/064001

Ricchiazzi, P., Yang, S., Gautier, C., & Sowle, D. (1998). SBDART: A research and teaching software tool for plane-parallel radiative transfer in the Earth's atmosphere. *Bulletin of the American Meteorological Society*, *79*(10), 2101–2114. https://doi.org/10.1175/1520-0477(1998)079<2101:SARATS>2.0.CO;2

Skamarock, W. C., Klemp, J. B., Dudhia, J., Gill, D. O., Barker, D., Duda, M. G., et al. (2008). A description of the advanced research WRF version 3 (Tech. Rep. NCAR/TN-475+STR). Boulder, CO: National Center for Atmospheric Research. https://doi.org/10.5065/D68S4MVH

Skiles, S. M., Painter, T. H., Deems, J. S., Bryant, A. C., & Landry, C. C. (2012). Dust radiative forcing in snow of the Upper Colorado River Basin: 2. Interannual variability in radiative forcing and snowmelt rates. *Water Resources Research*, *48*, W07522. https://doi.org/10.1029/2012WR011986

Sterle, K. M., McConnell, J. R., Dozier, J., Edwards, R., & Flanner, M. G. (2013). Retention and radiative forcing of black carbon in eastern Sierra Nevada snow. *The Cryosphere*, *7*(1), 365–374. https://doi.org/10.5194/tc-7-365-2013

Stohl, A., Aamaas, B., Amann, M., Baker, L. H., Bellouin, N., & Berntsen, T. K. (2015). Evaluating the climate and air quality impacts of short-lived pollutants. *Atmospheric Chemistry and Physics*, *15*, 10,529–10,566. https://doi.org/10.5194/acp-15-10529-2015

Stohl, A., Forster, C., Frank, A., Seibert, P., & Wotawa, G. (2005). Technical note: The Lagrangian particle dispersion model FLEXPART version 6.2. *Atmospheric Chemistry and Physics*, *5*(9), 2461–2474. https://doi.org/10.5194/acp-5-2461-2005

Stohl, A., Hittenberger, M., & Wotawa, G. (1998). Validation of the Lagrangian particle dispersion model FLEXPART against large-scale tracer experiment data. *Atmospheric Environment*, *32*(24), 4245–4264. https://doi.org/10.1016/S1352-2310(98)00184-8

Stohl, A., & Thomson, D. J. (1999). A density correction for Lagrangian particle dispersion models. *Boundary-Layer Meteorology*, *90*(1), 155–167. https://doi.org/10.1023/A:1001741110696

Taillandier, A.-S., Domine, F., Simpson, W. R., Sturm, M., & Douglas, T. A. (2007). Rate of decrease of the specific surface area of dry snow: Isothermal and temperature gradient conditions. *Journal of Geophysical Research*, *112*, F03003. https://doi.org/10.1029/2006JF000514

Tuzet, F., Dumont, M., Lafaysse, M., Picard, G., Arnaud, L., Voisin, D., et al. (2017). A multilayer physically based snowpack model simulating direct and indirect radiative impacts of light-absorbing impurities in snow. *The Cryosphere*, *11*(6), 2633–2653. https://doi.org/10.5194/tc-11-2633-2017

van der Walt, S., Colbert, S. C., & Varoquaux, G. (2011). The NumPy array: A structure for efficient numerical computation. *Computing in Science Engineering*, *13*(2), 22–30. https://doi.org/10.1109/MCSE.2011.37

van der Werf, G. R., Randerson, J. T., Giglio, L., Collatz, G. J., Mu, M., Kasibhatla, P. S., et al. (2010). Global fire emissions and the contribution of deforestation, savanna, forest, agricultural, and peat fires (1997–2009). *Atmospheric Chemistry and Physics*, *10*(23), 11,707–11,735. https://doi.org/10.5194/acp-10-11707-2010

Warren, S. G., & Wiscombe, W. J. (1980). A model for the spectral albedo of snow. II: Snow containing atmospheric aerosols. *Journal of the Atmospheric Sciences*, *37*(12), 2734–2745. https://doi.org/10.1175/1520-0469(1980)037<2734:AMFTSA>2.0.CO;2

Wiscombe, W. J., & Warren, S. G. (1980). A model for the spectral albedo of snow. I: Pure snow. *Journal of the Atmospheric Sciences*, *37*(12), 2712–2733. https://doi.org/10.1175/1520-0469(1980)037<2712:AMFTSA>2.0.CO;2

Xu, B., Cao, J., Joswiak, D. R., Liu, X., Zhao, H., & He, J. (2012). Post-depositional enrichment of black soot in snow-pack and accelerated melting of Tibetan glaciers. *Environmental Research Letters*, *7*(1), 14022. https://doi.org/10.1088/1748-9326/7/1/014022

Xu, J., Kang, S., Hou, S., Zhang, Q., Huang, J., Xiao, C., et al. (2016). Characterization of contemporary aeolian dust deposition on mountain glaciers of western China. *Sciences in Cold and Arid Regions*, *8*(1), 9–21.

Zhao, C., Hu, Z., Qian, Y., Ruby Leung, L., Huang, J., Huang, M., et al. (2014). Simulating black carbon and dust and their radiative forcing in seasonal snow: A case study over North China with field campaign measurements. *Atmospheric Chemistry and Physics*, *14*(20), 11,475–11,491. https://doi.org/10.5194/acp-14-11475-2014

Supporting Information for

"Assessing satellite derived radiative forcing from snow impurities through inverse hydrologic modelling"

F. N. Matt[1], **J. F. Burkhart**[1,2]

[1]Department of Geosciences, University of Oslo, Oslo, Norway.

[2]Statkraft As, Oslo, Norway.

Appendix A: Dynamical downscaling of ERA-Interim reanalysis data using WRF and evaluation of hydrologic model results

WRF was run with a nested approach with 1 km grid spacing for the inner domain, 5 km grid spacing for the intermediate domain, and 25 km grid spacing for the outer domain from October 1999 through September 2005 (excluding a prior 3 month spin-up time). The latter was forced with ERA-Interim reanalysis data [*Dee et al.*, 2011]. A similar WRF setup was used in *Engelhardt et al.* [2017], however, without the inner nested domain. Horizontal interpolation to the model domain of the hydrological model was performed using inverse distance weighting for all variables except temperature, taking into account a vertical adjustment for precipitation. Temperature interpolation was performed using Bayesian Kriging [*Diggle and Ribeiro*, 2007].

In order to investigate the quality of input datasets, we ran model calibration over the 6-year study period (Oct. 1999 through Sep. 2005) using daily meteorological model input from both station observations in the study region and the WRF output variables, respectively. The quality of hydrologic simulations is assessed by determining the Nash-Sutcliffe model efficiency (see auxiliary material B) using observed and simulated streamflow. Simulations show that using meteorological model input from WRF improves hydrologic simulations from 0.55 (station observations) to 0.79 (WRF) (see Table 1). Due to the significantly improved model performance we decided to use meteorological model input data from WRF in the case study.

Corresponding author: F. N. Matt, f.n.matt@geo.uio.no

Table 1. Calibration results using meteorological input to the hydrological model from station observations only (top row), partly from observations and from dynamically downscaled reanalysis data using WRF, and using WRF data only. T is daily air temperature, P is daily precipitation. Required input data to the hydrological model are global radiation, wind speed, relative humidity, air temperature, and precipitation.

Model Input Variables	Nash-Sutcliffe model efficiency
Observations only	0.55
Observations + T_{wrf}	0.65
Observations + T_{wrf} + P_{wrf}	0.73
WRF only	0.79

Appendix B: Model parameters and model performance measures

Table 2 gives an overview of model parameters. To evaluate the performance of the model during calibration, we determine the Nash-Sutcliffe model efficiency [*Nash and Sutcliffe*, 1970] comparing simulated to observed streamflow. To investigate the goodness-of-fit between simulated and MODDRFS instantaneous at-surface clear sky radiative forcing in snow (RFS_{sim}) we use the root-mean-square error E_{RMS} [e.g., *Bennett et al.*, 2013] of basin mean monthly RFS.

- **Nash-Sutcliffe model efficiency**

  The Nash-Sutcliffe model efficiency [*Nash and Sutcliffe*, 1970] allows to asses the predictive power of a model and is widely used in hydrologic modelling [*Bennett et al.*, 2013]. It is defined as:

$$E_{NS} = 1 - \frac{\sum_{t=0}^{T}(Q_o^t - Q_s^t)^2}{\sum_{t=0}^{T}(Q_o^t - \overline{Q_o})^2}, \tag{1}$$

  where Q_o^t and Q_s^t are the observed and simulated discharge at time t, respectively, and $\overline{Q_0}$ is the mean observed discharge over the assessed period.

- **Root-Mean-Squared Error**

  The Root-Mean-Squared Error is a general purpose error metric for numerical predictions [e.g., *Bennett et al.*, 2013], here stated for two time series, y_1 and y_2:

$$E_{RMS} = \sqrt{\frac{1}{n}\sum_{i=1}^{n}(y_{1,i} - y_{2,i})^2}, \tag{2}$$

  where $y_{1,i}$ and $y_{2,i}$ are members of a time series at time i, respectively, and n is the total number of members per time series.

Table 2. Model parameters used in the simulations. Parameters optimized during calibration are marked with * and resulting estimates are shown for the dust_6 scenario. Further parameters were pre-set and not included in parameter estimation during calibration.

Parameter	Description and unit	Optimized/set
c_1 *	discharge determining empirical coefficient 1 [-]	-5.190
c_2 *	discharge determining empirical coefficient 2 [-]	0.5594
c_3 *	discharge determining empirical coefficient 3 [-]	-0.04189
ae_scale_factor *	scaling factor for actual evapotranspiration [-]	1.41
tx *	temperature threshold rain/snow [°C]	1.52
wind_const *	determining wind profile [-]	4.10
wind_scale *	determining wind profile [-]	4.64
$A_{s,0}$	specific surface area A_s of fresh snow [m^2 kg^{-1}]	73.0
snowfall_reset_depth	minimum snowfall required to reset A_s [mm SWE]	5.0
snow_cv_forest	Coefficient of variation of snow distribution in forested area [-]	0.17
snow_cv	Coefficient of variation of snow distribution in forested free area [-]	0.4
max_water	fractional max water content of snow [-]	0.10
surface_magnitude	maximum snow depth for snow heat content [mm SWE]	30.0
max_surface_layer	maximum thickness of snow surface layer [mm SWE]	8.0
depo_factor	multiplication factor for dust deposition (dust_6 scenario) [-]	6.0
k_{phil}	melt scavenging ratio of hydrophilic BC [-]	0.2
k_{phob}	melt scavenging ratio of hydrophobic BC [-]	0.03
k_{dust}	melt scavenging ratio of dust [-]	0.01

Appendix C: Summary of methods

Table 3. Comparison of radiative forcing retrieval methods used in the MODDRFS algorithm and our approach.

	MODDRFS	MODEL
Optical grain radius (OGR)	Estimated from the normalized difference grain size index (NDGSI), which is sensitive to OGR and solar zenith angle.	Modelled OGR according to *Brun* [1989] for wet snow and *Taillandier et al.* [2007] for dry snow.
Bare ground masking	MODIS Snow Covered Area and Grainsize (MODSCAG) fractional snow and vegetation products to exclude pixels with mixed cover of vegetation	Grid cells with snow cover lower than 0.9 are excluded from the analysis.
Spectral irradiation	Incident spectral irradiances determined at 1/5th MODIS pixel spatial resolution and then up-scaled to pixel resolution.	Incident spectral irradiances determined at 1/5th model grid spatial resolution and then up-scaled to grid cell resolution.
Topographic radiation correction	$E_{corrected,\lambda} =$ $\cos\beta \cdot E_{direct,\lambda} + E_{diffuse,\lambda}$ where β is the per-pixel slope and aspect depended local solar zenith angle	$E_{corrected,\lambda} =$ $\cos\beta \cdot E_{direct,\lambda} + E_{diffuse,\lambda}$ where β is the per-grid cell slope and aspect depended local solar zenith angle
Clean snow albedo α_{clean}	Modelled clean snow at same OGR as determined from NDGSI and SZA from MODIS overflight predictor.	Modelled with SNICAR for the wavelength bands i=1 (0.3-0.7 μm) and i=2 (0.7-1.0 μm) assuming no impurities in the snow, OGR from model output, and SZA from MODIS overflight predictor.
Polluted snow albedo $\alpha_{polluted}$	Measured spectral MODIS albedo, fit to modelled clean spectrum at $MODIS_2$ band center, and interpolated to a continuous spectrum of 0.001 μm.	Modelled with SNICAR for the wavelength bands i=1 (0.3-0.7 μm) and i=2 (0.7-1.0 μm) assuming LAISI mixing ratios and OGR as predicted by the model, and SZA from the MODIS overflight predictor.
Radiative Forcing F	$F = \sum_{\lambda=0.350\mu m}^{0.876\mu m} E_{corrected,\lambda}(\alpha_{clean,\lambda} - \alpha_{MODIS,\lambda})\Delta\lambda$	$E_{corrected,1} = \sum_{\lambda=0.3\mu m}^{0.7\mu m} E_{corrected,\lambda}\Delta\lambda$ $E_{corrected,2} = \sum_{\lambda=0.7\mu m}^{1.0\mu m} E_{corrected,\lambda}\Delta\lambda$ $F_c = c \cdot \sum_{i=1}^{2} E_{corrected,i}(\alpha_{clean,i} - \alpha_{polluted,i})$ where c is a correction factor accounting the spectral band mismatch between model and MODDRFS.

Appendix D: Black carbon (BC) deposition input data

Wet and dry deposition rates over the study region are modelled with the Flexible Particle Dispersion Model (FLEXPART) [*Stohl et al.*, 1998; *Stohl and Thomson*, 1999; *Stohl et al.*, 2005]. To develop the scenarios for this study, FLEXPART used particles parameterized only for BC emissions as developed from the ECLIPSE (Evaluating the Climate and Air Quality Impacts of Short-Lived Pollutants) emission inventory version V4a [*Klimont et al.*, 2017]. The ECLIPSE inventory was created using the GAINS (Greenhouse gas - Air pollution Interactions and Synergies) model [*Amann et al.*, 2011], which provides emissions of long-lived greenhouse gases and shorter-lived species in a consistent framework. Details of the inventory are described in *Stohl et al.* [2015]. Open biomass burning emissions are not calculated in the GAINS model, therefore we used the Global Fire Emission Database (GFED), version 3.1 [*van der Werf et al.*, 2010] for BC emissions from non-agricultural sources.

FLEXPART simulations were conducted for the period 2003 through 2013 in the forward mode using 3-hourly, operational analyses from the European Centre for Medium Range Weather Forecasts (ECMWF) on a 1°x1° resolution with 92 vertical layers. We developed a climatology of the BC deposition to create a seasonal BC deposition profile for two reasons. First, the GFED emissions data is not available prior to 2003. Second, since the wet deposition rates from FLEXPART are decoupled from the dynamically downscaled and interpolated precipitation input to the hydrological model, we follow the suggestion from *Doherty et al.* [2014] and calculate a monthly mean climatology of BC aerosol depositions. Wet deposition rates were used to create monthly mean climatological BC mixing ratios in falling snow. We then account for wet and dry deposition of BC in the hydrological model by using the monthly climatologies of dry deposition mass fluxes and mixing ratios in falling snow from wet deposition. This approach avoids a positive bias in surface snow mixing ratios due to decoupling of wet deposition rates from precipitation [*Doherty et al.*, 2014].

Appendix E: Basin mean monthly RFS and LAISI impact on discharge

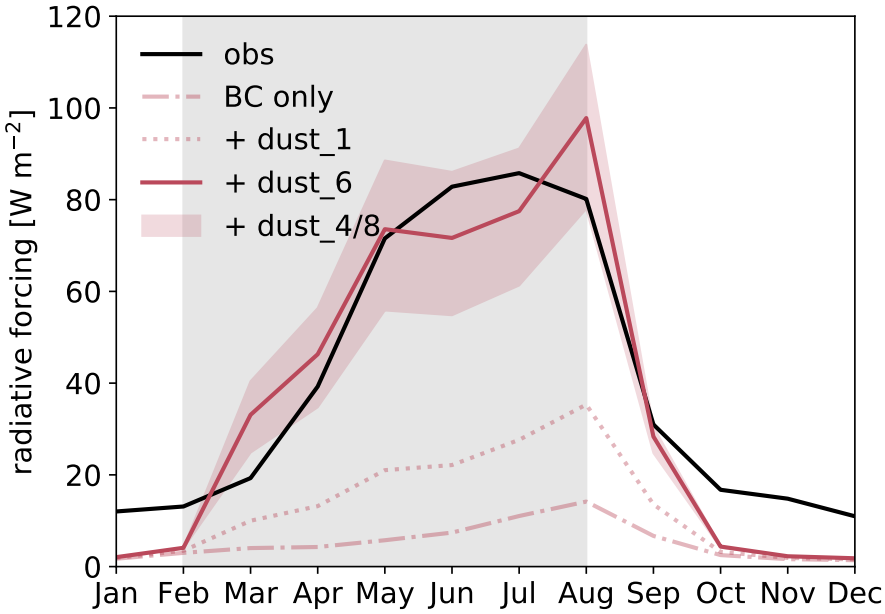

Figure 1. Monthly mean instantaneous radiative forcing from observations and model simulations using different LAISI scenarios. The red shaded area shows the difference between the dust_4 and dust_8 scenarios used as LAISI forcing uncertainty in the impact estimation on discharge. The gray box marks the melt period. Best results in terms of E_{RMS} gives the dust_6 scenario (see Table 4).

Table 4. Summary of simulation results.

scenario	dust deposition* [g $m^{-2}a^{-1}$]	E_{NS}* [-]	mean** [W m^{-2}]	E_{RMS}** [W m^{-2}]	discharge due LAISI* [%]
obs	**-**	**-**	**53.14**	**0**	**-**
dust_0	0	0.761	7.04	52.57	0.71
dust_1	3	0.770	18.29	39.98	1.91
dust_2	6	0.776	27.50	29.91	2.81
dust_3	9	0.780	35.36	21.62	3.52
dust_4	12	0.783	42.28	15.04	4.11
dust_5	15	0.785	48.48	10.82	4.61
dust_6	**18**	**0.787**	**54.04**	**10.23**	**5.04**
dust_7	21	0.788	59.21	12.95	5.41
dust_8	24	0.789	63.86	16.87	5.75

* Annual. ** Melt period only (February through August).

References

Amann, M., I. Bertok, J. Borken-Kleefeld, J. Cofala, C. Heyes, L. Höglund-Isaksson, Z. Klimont, B. Nguyen, M. Posch, P. Rafaj, R. Sandler, W. Schöpp, F. Wagner, and W. Winiwarter (2011), Cost-effective control of air quality and greenhouse gases in europe: Modeling and policy applications, *Environmental Modelling & Software*, *26*(12), 1489–1501, doi:10.1016/j.envsoft.2011.07.012.

Bennett, N. D., B. F. Croke, G. Guariso, J. H. Guillaume, S. H. Hamilton, A. J. Jakeman, S. Marsili-Libelli, L. T. Newham, J. P. Norton, C. Perrin, S. A. Pierce, B. Robson, R. Seppelt, A. A. Voinov, B. D. Fath, and V. Andreassian (2013), Characterising performance of environmental models, *Environmental Modelling & Software*, *40*, 1–20, doi:10.1016/j.envsoft.2012.09.011.

Brun, E. (1989), Investigation on wet-snow metamorphims in respect of liquid water content, *Annals of Glaciology*, *13*, 22–26, doi:10.3189/S0260305500007576.

Dee, D. P., S. M. Uppala, A. J. Simmons, P. Berrisford, P. Poli, S. Kobayashi, U. Andrae, M. A. Balmaseda, G. Balsamo, P. Bauer, P. Bechtold, A. C. M. Beljaars, L. van de Berg, J. Bidlot, N. Bormann, C. Delsol, R. Dragani, M. Fuentes, A. J. Geer, L. Haimberger, S. B. Healy, H. Hersbach, E. V. Hólm, L. Isaksen, P. Kållberg, M. Köhler, M. Matricardi, A. P. McNally, B. M. Monge-Sanz, J.-J. Morcrette, B.-K. Park, C. Peubey, P. de Rosnay, C. Tavolato, J.-N. Thépaut, and F. Vitart (2011), The ERA-interim reanalysis: configuration and performance of the data assimilation system, *Quarterly Journal of the Royal Meteorological Society*, *137*(656), 553–597, doi:10.1002/qj.828.

Diggle, P. J., and P. J. Ribeiro (2007), *Model-based Geostatistics*, Springer Series in Statistics, 232 pp., Springer, New York, USA, doi:10.1007/978-0-387-48536-2.

Doherty, S. J., C. M. Bitz, and M. G. Flanner (2014), Biases in modeled surface snow BC mixing ratios in prescribed-aerosol climate model runs, *Atmospheric Chemistry and Physics*, *14*(21), 11,697–11,709, doi:10.5194/acp-14-11697-2014.

Engelhardt, M., P. Leclercq, T. Eidhammer, P. Kumar, O. Landgren, and R. Rasmussen (2017), Meltwater runoff in a changing climate (1951-2099) at chhota shigri glacier, western himalaya, northern india, *Annals of Glaciology*, pp. 1–12, doi:10.1017/aog.2017.13.

Klimont, Z., K. Kupiainen, C. Heyes, P. Purohit, J. Cofala, P. Rafaj, J. Borken-Kleefeld, and W. Schöpp (2017), Global anthropogenic emissions of particulate matter including

black carbon, *Atmospheric Chemistry and Physics*, *17*, 8681–8723, doi:10.5194/acp-17-8681-2017.

Nash, J. E., and J. V. Sutcliffe (1970), River flow forecasting through conceptual models part i - a discussion of principles, *Journal of Hydrology*, *10*(3), 282–290, doi: https://doi.org/10.1016/0022-1694(70)90255-6.

Stohl, A., and D. J. Thomson (1999), A density correction for lagrangian particle dispersion models, *Boundary-Layer Meteorology*, *90*(1), 155–167, doi: 10.1023/A:1001741110696.

Stohl, A., M. Hittenberger, and G. Wotawa (1998), Validation of the lagrangian particle dispersion model FLEXPART against large-scale tracer experiment data, *Atmospheric Environment*, *32*(24), 4245–4264, doi:10.1016/S1352-2310(98)00184-8.

Stohl, A., C. Forster, A. Frank, P. Seibert, and G. Wotawa (2005), Technical note: The lagrangian particle dispersion model FLEXPART version 6.2, *Atmospheric Chemistry and Physics*, *5*(9), 2461–2474, doi:10.5194/acp-5-2461-2005.

Stohl, A., B. Aamaas, M. Amann, L. H. Baker, N. Bellouin, T. K. Berntsen, O. Boucher, R. Cherian, W. Collins, N. Daskalakis, M. Dusinska, S. Eckhardt, J. S. Fuglestvedt, M. Harju, C. Heyes, Ø. Hodnebrog, J. Hao, U. Im, M. Kanakidou, Z. Klimont, K. Kupiainen, K. S. Law, M. T. Lund, R. Maas, C. R. MacIntosh, G. Myhre, S. Myriokefalitakis, D. Olivié, J. Quaas, B. Quennehen, J.-C. Raut, S. T. Rumbold, B. H. Samset, M. Schulz, Ø. Seland, K. P. Shine, R. B. Skeie, S. Wang, K. E. Yttri, and T. Zhu (2015), Evaluating the climate and air quality impacts of short-lived pollutants, *Atmospheric Chemistry and Physics*, *15*, 10,529–10,566, doi:10.5194/acp-15-10529-2015.

Taillandier, A.-S., F. Domine, W. R. Simpson, M. Sturm, and T. A. Douglas (2007), Rate of decrease of the specific surface area of dry snow: Isothermal and temperature gradient conditions, *Journal of Geophysical Research*, *112*(F3), F03,003, doi: 10.1029/2006JF000514.

van der Werf, G. R., J. T. Randerson, L. Giglio, G. J. Collatz, M. Mu, P. S. Kasibhatla, D. C. Morton, R. S. DeFries, Y. Jin, and T. T. van Leeuwen (2010), Global fire emissions and the contribution of deforestation, savanna, forest, agricultural, and peat fires (1997-2009), *Atmospheric Chemistry and Physics*, *10*(23), 11,707–11,735, doi: 10.5194/acp-10-11707-2010.

Part III

Appendices

A WRF configuration files

A.1 namelist.wps file content

```
&share
 wrf_core         = 'ARW',
 max_dom          = 3,
 start_date       = '1999-07-01_00:00:00','1999-07-01_00:00:00','1999-07-01_00:00:00',
 end_date         = '2005-12-31_18:00:00','2005-12-31_18:00:00', '2005-12-31_18:00:00',
 interval_seconds = 21600
 io_form_geogrid  = 2,
 /

&geogrid
 parent_id         =   1,   1, 2,
 parent_grid_ratio =   1,   5, 5,
 i_parent_start    =   1,  80,  75,
 j_parent_start    =   1,  101, 95,
 e_we              =  217, 251, 301,
 e_sn              =  185, 221, 251
 geog_data_res     = 'modis_lakes+30s','modis_lakes+30s','modis_lakes+30s'
 dx                = 25000,
 dy                = 25000,
 map_proj          = 'lambert',
 ref_lat           =  25.0,
 ref_lon           = 80.0,
 truelat1          =  30.0,
 truelat2          =  60.0,
 stand_lon         = 80.0,
 geog_data_path    = '/path/to/geog'
 /

&ungrib
 out_format = 'WPS',
 prefix     = 'FILE',
 /

&metgrid
 fg_name         = 'FILE'
 constants_name  = 'TAVGSFC'
 io_form_metgrid = 2,
 /
```

A.2 namelist.input file content

```
&time_control
 start_year                          = 1999, 1999, 1999,
 start_month                         = 07,   07,   07,
 start_day                           = 01,   01,   01,
 start_hour                          = 00,   00,   00,
 start_minute                        = 00,   00,   00,
 start_second                        = 00,   00,   00,
 end_year                            = 2005, 2005, 2005,
 end_month                           = 12,   12,   12,
 end_day                             = 31,   31,   31,
 end_hour                            = 18,   18,   18,
 end_minute                          = 00,   00,   00,
 end_second                          = 00,   00,   00,
 interval_seconds                    = 21600
 input_from_file                     = .true.,.true.,.true.,
 history_interval                    = 180,  60,   60,
 frames_per_outfile                  = 1, 1, 1,
 restart                             = .true.,
 restart_interval                    = 1440,
 io_form_history                     = 2
 io_form_restart                     = 2
 io_form_input                       = 2
 io_form_boundary                    = 2
 debug_level                         = 0
 auxinput4_inname                    = "wrflowinp_d<domain>",
 auxinput4_interval                  = 360,
 io_form_auxinput4                   = 2,
 override_restart_timers             = .true.,
 write_hist_at_0h_rst                = .true.,
 /

&domains
 time_step                           = 100,
 time_step_fract_num                 = 0,
 time_step_fract_den                 = 1,
 max_dom                             = 3,
 e_we                                = 217,    251,   301,
 e_sn                                = 185,    221,   251,
 e_vert                              = 40,    40,    40,
 p_top_requested                     = 2500,
 num_metgrid_levels                  = 38,
 num_metgrid_soil_levels             = 4,
 dx                                  = 25000, 5000,  1000,
 dy                                  = 25000, 5000,  1000,
 grid_id                             = 1,     2,     3,
 parent_id                           = 0,     1,     2,
 i_parent_start                      = 1,     80,    75,
 j_parent_start                      = 1,     101,   95,
 parent_grid_ratio                   = 1,     5,     5,
 parent_time_step_ratio              = 1,     5,     5,
 feedback                            = 0,
```

```
 interp_type                         = 1,
 lagrange_order                      = 1,
 smooth_option                       = 0
 eta_levels                          = 1.,
                                       0.9974,
                                       0.9940, 0.9905, 0.9850, 0.9800,
                                       0.9700, 0.9600, 0.9450, 0.9300, 0.9100,
                                       0.8900, 0.8650, 0.8400, 0.8100, 0.7800,
                                       0.7500, 0.7100, 0.6800, 0.6450, 0.6100,
                                       0.5700, 0.5300, 0.4900, 0.4500, 0.4100,
                                       0.3700, 0.3300, 0.2900, 0.2500, 0.2100,
                                       0.1750, 0.1450, 0.1150, 0.0900, 0.0650,
                                       0.0450, 0.0250, 0.0100, 0.0000,
 /

&physics
 mp_physics                          = 8,     8,     8,
 ra_lw_physics                       = 4,     4,     4,
 ra_sw_physics                       = 4,     4,     4,
 radt                                = 30,    10,    5,
 sf_sfclay_physics                   = 1,     1,     1,
 sf_surface_physics                  = 4,     4,     4,
 bl_pbl_physics                      = 1,     1,     1,
 bldt                                = 0,     0,     0,
 cu_physics                          = 6,     0,     0,
 cudt                                = 0,     0,     0,
 isfflx                              = 1,
 ifsnow                              = 1,
 icloud                              = 1,
 surface_input_source                = 1,
 num_soil_layers                     = 4,
 num_land_cat                        = 21,
 sf_urban_physics                    = 0,     0,     0,
 sst_update                          = 1,
 fractional_seaice                   = 0,
 bucket_mm                           = 100.0,
 bucket_J                            = 1.e9,
 sst_skin                            = 1,
 lagday                              = 150,
 tmn_update                          = 1,
 prec_acc_dt                         = 180, 60, 60,
 aer_opt                             = 2,
 mp_zero_out                         = 0,
 rdmaxalb                            = .false.,
 slope_rad                           = 1,
 topo_shading                        = 0,
 topo_wind                           = 0,
 do_radar_ref                        = 1,
 /

&noah_mp
 dveg                                = 4,
 opOBt_crs                           = 1,
```

```
 opt_btr                             = 2,
 opt_sfc                             = 1,
 opt_run                             = 1,
 opt_frz                             = 1,
 opt_inf                             = 1,
 opt_rad                             = 3,
 opt_alb                             = 2,
 opt_snf                             = 4,
 opt_tbot                            = 1,
 opt_stc                             = 1,
 /

&fdda
 /

&dynamics
 w_damping                           = 1,
 diff_opt                            = 1,      1,      1,
 km_opt                              = 4,      4,      4,
 diff_6th_opt                        = 0,      0,      0,
 diff_6th_factor                     = 0.12,   0.12,   0.12,
 base_temp                           = 290.
 damp_opt                            = 3,
 zdamp                               = 5000.,  5000.,  5000.,
 dampcoef                            = 0.2,    0.2,    0.2
 khdif                               = 0,      0,      0,
 kvdif                               = 0,      0,      0,
 non_hydrostatic                     = .true., .true., .true.,
 moist_adv_opt                       = 1,      1,      1,
 scalar_adv_opt                      = 1,      1,      1,
 epssm                               = 0.7,    0.7,    0.7,
 do_avgflx_em                        = 1,      1,      1,
 /

&bdy_control
 spec_bdy_width                      = 5,
 spec_zone                           = 1,
 relax_zone                          = 4,
 specified                           = .true., .false.,.false.,
 nested                              = .false., .true., .true.,
 /

&grib2
 /

&namelist_quilt
 nio_tasks_per_group = 0,
 nio_groups          = 1,
 /
```